PROCESS MODELING OF MICRO-CUTTING INCLUDING STRAIN GRADIENT EFFECTS

A Thesis
Presented to
The Academic Faculty

by

Kai Liu

In Partial Fulfillment
of the Requirements for the Degree
Doctor of Philosophy in the
George W. Woodruff School of Mechanical Engineering

Georgia Institute of Technology
December, 2005

PROCESS MODELING OF MICRO-CUTTING INCLUDING STRAIN GRADIENT EFFECTS

Approved by:

Dr. Shreyes N. Melkote, Advisor
School of Mechanical Engineering
Georgia Institute of Technology

Dr. Naresh N. Thadhani
School of Materials Science & Engineering
Georgia Institute of Technology

Dr. Steven Y. Liang
School of Mechanical Engineering
Georgia Institute of Technology

Dr. Rami M. Haj-Ali
School of Civil & Environmental Engineering
Georgia Institute of Technology

Dr. Min Zhou
School of Mechanical Engineering
Georgia Institute of Technology

Date Approved: October, 7, 2005

To My Parents

ACKNOWLEDGEMENTS

The progression of research towards gaining a new understanding and attaining a completed work worthy of a Ph.D. has been a precious experience from which I shall benefit for my whole career. This progression could not have been completed without the help and support from many people. I would like to extend special thanks to my advisor, Dr. Shreyes Melkote. Thanks for all the inspiring and wonderful discussions, encouragement and patience he provided throughout my stay at Georgia Tech.

I would like to thank Drs. Steven Liang, Naresh Thadhani, Min Zhou and Rami Haj-Ali for providing guidance and serving on my committee. Thanks to other faculty members of the PMRC, Dr. Tom Kurfess, Dr. Steven Danyluk for providing complete access to all labs and equipments. Thanks as well to the lab personnel, Steven Sheffield, John Graham and John Morehouse for all the assistance on the machine shop training and safety classes.

I would like to extend my sincere thanks to my fellow researchers and labmates, Anand Ramesh, Sangil Han, Sathyan Subbiah, Ramesh Singh and Chee Keong Ng for their help with many technical issues and useful discussions.

I would like to thank Dr. Suhas Joshi of IIT, Bombay for guidance in early stages of my research. Thanks to Dr. Martin Baeker at the Institut fuer Werkstoffe, University of Braunschweig for all the advice on ABAQUS related issues. I would also like to thank Dr. Rob Ivester at NIST for assisting with the micro-cutting experiments. Thanks to Mr. Kenneth Niebauer at Kennemetal Inc. for assisting with the trace analysis of the tool inserts.

Thanks are also due to Dr. Douglas Bammann at Sandia National Laboratories for his guidance on material constitutive modeling and a wonderful lecture.

I would like to thank my parents for their support and encouragement which has been ever present and ever felt. Special thanks to my sister for putting up with my long absences from home and taking care of the parents.

TABLE OF CONTENTS

LIST OF TABLES

LIST OF FIGURES

LIST OF SYMBOLS

A	Material constant in Johnson-Cook equation
B	Material constant in Johnson-Cook equation
c	Material constant in Johnson-Cook equation
n	Material constant in Johnson-Cook equation
m	Material constant in Johnson-Cook equation
F_c	Cutting Force
F_t	Thrust Force
p	Contact pressure
τ^*	Limiting shear stress in Coulomb friction model
s	Frictional shear stress
μ	Friction of coefficient
r	Cutting ratio
r_n	Nose radius
r_e	Cutting edge radius
N_i	Interpolation function of an 8-node quadratic element
t	Uncut chip thickness
t_c	Deformed chip thickness
T	Instantaneous temperature in Johnson-Cook equation
T_m	Melting point temperature in Johnson-Cook equation
T_o	Ambient temperature in Johnson-Cook equation

T^*	Dimensionless temperature in Johnson-Cook equation ($\frac{T - T_o}{T_m - T_o}$)
$\dot{Q}$	Volume heat flux
$\dot{U}$	Material time rate of internal thermal energy
C_p	Specific heat capacity
K	Thermal conductivity
C_d	Damping factor
F_v	Viscous force
M^*	Artificial mass
P_e	External forces
I_i	Internal nodal forces
Δt	Time increment
w	Width of cut
V_c	Cutting velocity
α	Rake angle
β	Friction angle
γ	Shear strain
H	Hardness
G	Shear modulus
ρ	Dislocation density
ρ_s	Statistically stored dislocation density
ρ_g	Geometrically necessary dislocation density
ρ_m	Material density

b	Burgers vector
R_{th}	Kinematic/theoretical peak-to-valley surface roughness
R_p	Peak-to-valley surface roughness due to plastic side flow
R_{edge}	Peak-to-valley surface roughness due to non-smooth cutting edge
R_{total}	Total peak-to-valley surface roughness
R_{exp}	Measured peak-to-valley surface roughness
x	rheological factor
$\overline{\sigma}_y$	Average flow stress
$\overline{\tau}$	Average shear flow stress
θ	Semi-apical angle of the indenter/tool
h_a	Actual contact depth in scratch test
h	Contact depth in scratch test
f	Feed
e	Material strength difference ratio
ε	Effective (True) Strain
ε_{ij}	Strain tensor
ε'_{ij}	Deviatoric strain tensor
$\dot{\varepsilon}$	Strain rate
$\dot{\varepsilon}_o$	Reference strain rate
$\dot{\varepsilon}^p$	Effective plastic strain rate
ε^p	Effective plastic strain
E	Young's modulus
κ	Bulk modulus

φ	Shear angle
σ	Flow stress
σ_{ref}	Reference flow stress in uniaxial tension
σ_{ij}	Stress tensor
σ'_{ij}	Deviatoric stress tensor
τ	Shear stress
η_{ijk}	Strain gradient tensor
η'_{ijk}	Deviatoric strain gradient
δ_{ij}	Kronecker delta
η	Effective strain gradient
l	Material length scale in strain gradient plasticity
ξ_i	Coordinates in isoparametric space
A_{cell}	Mesoscale cell used to evaluate strain gradient
l_ε	Edge length of the square mesoscale cell
I_ε	Moment of inertia of the mesoscale cell
$w(x,y)$	Weighting function in diffuse approximation method
$p(x,y)$	Polynomial basis in diffuse approximation method
λ	Coefficient controlling the shape of weighting function
$\vec{X}$	Position vector at point x
$\vec{X}_i$	Position vector at point x_i

SUMMARY

At micrometer length scales of material removal, size effect is observed in mechanical micro-cutting where the energy per unit volume i.e. specific cutting energy increases nonlinearly as the uncut chip thickness is reduced from several hundred microns to a few microns (or less). There is no consensus in the literature on the cutting mechanism that causes this size effect. Noticeable discrepancy is also observed in the surface roughness produced at small feeds in micro-cutting operations such as micro-turning between the theoretical roughness estimated using only tool geometry and process kinematics and the measured roughness. To date, there has been little effort made to develop a detailed process model for micro-cutting to accurately predict the size effect in specific cutting energy, and to develop a fundamental understanding of surface generation at the low feeds typical of micro-cutting processes.

The main objective of this thesis is therefore to develop a predictive process model of micro-cutting of ductile metals that is capable of accurately predicting the size effect in specific cutting energy based on strain gradient based material strengthening considerations. In addition, this thesis attempts to explain the discrepancy between the theoretical and measured surface roughness at small feeds in micro-turning via a model that accounts for the size effect due to material strengthening.

A coupled thermo-mechanical finite element model formulation incorporating strain gradient plasticity is developed to simulate orthogonal micro-cutting process. The thermo-mechanical model is experimentally validated in orthogonal micro-cutting of a strain rate insensitive aluminum alloy Al5083-H116. The model is then used to analyze

the contributions of two major material strengthening factors to the size effect in specific cutting energy: strain gradient and temperature. The effects of cutting edge radius on the specific cutting energy and its role relative to the material length scale arising from strain gradient plasticity are also examined. The strain gradient plasticity based model of micro-cutting is shown to contribute significantly to the size-effect at low cutting speeds and small uncut chip thickness levels (< 10μm). Temperature dependence of material flow stress is seen to cause size effect at relatively high cutting speeds and large uncut chip thickness. However, strain gradient strengthening is more dominant than the temperature effect at high cutting speeds and small uncut chip thickness values.

A surface roughness model for micro-turning that incorporates the effects of kinematic roughness, cutting edge roughness and surface roughening due to plastic side flow is developed and shown to explain the observed discrepancy between the theoretical and measured surface roughness in micro-cutting. In addition, the model is found to accurately capture the increase in surface roughness at very low feeds.

CHAPTER 1

INTRODUCTION

1.1 Background

The need for engineered component possessing three-dimensional micro/meso scale features and sub-micron surface finish keeps increasing rapidly in the fields of optics, die and molds, semiconductor and biomedical devices, to name a few. Specific applications include microscale pumps, valves and mixing devices, micro-fluidic systems, micro-molds, micro-holes for fiber optics and micro-nozzles for high-temperature jets [1-11]. These applications require very tight tolerances, high quality surface finish, and both functional and structural requirements that demand the use of various engineering materials, including aluminum alloys, stainless steel, titanium, brass, plastics, ceramics, and composites. Mechanical micro-cutting, as an ultra-precision machining process, is becoming increasingly important for its capability of producing parts with three dimensional features ranging from a few microns to a few hundred microns in a wide range of materials. For the purpose of this thesis, micro-cutting is defined as a mechanical cutting process with uncut chip thickness varying from submicron to a few hundred microns.

There are a number of issues in micro-scale cutting that are fundamentally different from macro-scale cutting. They include differences in the underlying mechanisms of the process, resulting in changes in the chip formation process, machining forces, specific energy and surface finish. For example, the tool cutting edge geometry

becomes comparable in size to the uncut chip thickness, which causes the effective rake angle to be negative. This in turn causes the ploughing and associated elastic-plastic deformation of the workpiece material to become much more dominant factors in the process. Furthermore, at micrometer length scales of material removal, the well known size effect is observed in micro-cutting where the specific cutting energy/force increases non-linearly with decrease in uncut chip thickness [12-18]. However, there exists no consensus on a phenomenological explanation of size-effect in micro-cutting. In recent experiments of micro- and nano-indentation, remarkable material strengthening behavior has been found at and below length scales of the order of a micrometer due to highly localized inhomogeneous deformation [19-23]. Intense strain gradient is also observed within the primary and secondary deformation zones in both macro- and micro-cutting, which suggests that the strain gradient in micro-cutting is an important factor that affects the material strength. To date, there has been little effort to systematically assimilate the effects of workpiece and tool material properties and cutting variables in micro-cutting to predict the size effect. In particular, no numerical modeling work on micro-cutting has considered the effects of strain gradient induced strengthening of the workpiece material. Moreover, most of the prior work attributes the size effect in cutting to a single factor such as inhomogeneous deformation, tool edge radius or ductile fracture energy and does not consider the possibility and roles of multiple factors and relative contribution to the size effect.

It is also known that the machined surface roughness at low feeds (or uncut chip thickness) is often larger than the theoretical roughness estimated using only tool geometry and process kinematics [24]. The contribution of plastic deformation to surface

roughness needs to be considered since plastic deformation in the primary deformation zone often extends into the material adjacent to the machined surface and in the out-of-plane direction to cause side flow. In micro-cutting, the uncut chip thickness is small that the effect of process kinematics on surface roughness becomes comparable to or less than the effect of plastic deformation. So far there has been little work done to account for the plastic deformation induced surface roughness in micro-cutting processes.

Therefore, the focus of this thesis is to model and investigate the influence of strain gradient strengthening at the microscale on the size effect in specific cutting energy, as well as surface roughness in micro-cutting. To this end, strain gradient plasticity will be incorporated into a thermo-mechanical model of the orthogonal micro-cutting process. The fundamental mechanism of size effect and surface roughening will be explained through a quantitative framework. The model developed for orthogonal micro-cutting constitutes the first step in developing a micro-cutting process simulation model for analysis of three dimensional operations such as micro-turning and micro-milling in the future. It would also serve to provide a better physical understanding of material and cutting parameter interactions in micro-cutting and aid in optimizing the machining conditions.

The research plan is divided into the following four areas: (1) Thermo-mechanical finite element modeling of the orthogonal micro-cutting process based on strain gradient plasticity, (2) Analysis of the size effect in specific cutting energy caused by strain gradient and the roles of other factors such as temperature and edge radius, (3) Developing a model-based approach to explain surface roughening due to plastic deformation in micro-cutting, and (4) Experimental validation of the models.

1.2 Problem Statement

Thermo-mechanical modeling of macro- and micro-cutting processes has been carried out by a number of investigators. However, process modeling of micro-cutting including the effects of intense strain gradient within the primary and secondary deformation zones has not been considered. Also, little work has been done to analyze surface roughness generation in micro-cutting and in particular the influence of plastic deformation on the surface roughness. This is of vital importance in micro-cutting processes.

Therefore, the specific objectives of this thesis are:

- Thermo-mechanical modeling of chip formation, cutting forces and size effect in orthogonal micro-cutting, including the strain gradient effect.
- Experimental verification of the developed finite element model.
- Develop an understanding of the relative roles of strain gradient, temperature drop induced strengthening, and tool edge radius effects on the size effect in specific cutting energy in micro-cutting.
- Analysis of the influence of plastic side flow of workpiece on the surface roughness of the machined surface

1.3 Research Approach

As has been stated previously, development of a simulation tool for the prediction of size effect and surface finish is of interest in micro-cutting. Prior to doing this, it is necessary to understand the fundamental mechanics in micro-cutting. Keeping this in mind, the research approach adopted in this thesis is as follows:

- Develop and validate a finite element model of orthogonal micro-cutting using a commercially available package to describe the thermo-mechanical aspects of the material removal process, taking into account chip formation, frictional effects and workpiece constitutive behavior.
- Using the developed finite element model, analyze quantitatively the main factors that contribute to size effect in micro-cutting, understand the contributions of each factor to the nonlinear increase in specific cutting energy with decrease in uncut chip thickness and the conditions under which they are dominant.
- Develop a model that accounts for the effects of plastic deformation in micro-turning on surface roughness of the machined surface.
- Experimentally validate the above models through measurement of cutting forces and surface roughness in orthogonal micro-cutting and micro-turning tests, respectively.

1.4 Dissertation Outline

Chapter II reviews the prior work in the field of modeling of machining processes. Previous attempts to explain the size effect and predict the surface roughness in micro-cutting processes are discussed. A detailed description of the finite element modeling of orthogonal micro-cutting process is discussed in Chapter 3. The details of the orthogonal cutting experiments and validation of the finite element model are discussed in Chapter 4. Chapter 5 contains detailed analysis of the main factors that cause size effect in micro-cutting. Modeling of the surface roughness in micro-cutting and validation of this aspect

are presented in Chapter 6. Finally, the main conclusions and contributions of this dissertation and a discussion of possible avenues of future research are presented in Chapter 7.

CHAPTER 2

SURVEY OF PRIOR WORK

This chapter summarizes the experimental observation of size effect in micro-cutting and mechanisms that have been proposed to explain the size effect. Current state of the art in modeling of machining processes is reviewed and particular emphasis is given to the application of finite element methods to machining. This is followed by an overview of the theory of strain gradient plasticity, which is proposed to correctly represent the material behavior in cutting process at the micron/submicron level. Prior work on the prediction of surface roughness in micro-cutting is also discussed.

2.1 Size Effect in Micro-cutting

Micro-cutting is characterized by very small amounts of material removal with uncut chip thickness values that vary from a few microns (or less) to several hundred microns. At these length scales of material removal, the well-known size effect phenomenon is expected to be prominent. In machining, the size effect is typically characterized by a non-linear increase in the specific cutting energy (or specific cutting force) as the uncut chip thickness is decreased.

Experimental observations of size effect in machining of different materials under different cutting conditions have been reported in the literature. Backer and Shaw [12] reported size effect in turning tests performed on SAE 1112 steel (see Figure 2.1). Tests were performed on a 57.2 mm diameter bar premachined in the form of a thin-walled

tube having a wall thickness of 5 mm. A carbide tool with 0 degree rake angle and 5 degree clearance angle was used for orthogonal cutting the end of the tube. Cutting tests were conducted at a cutting speed of 137.16 m/min with uncut chip thickness ranging from 58.4 μm to 294.6 μm.

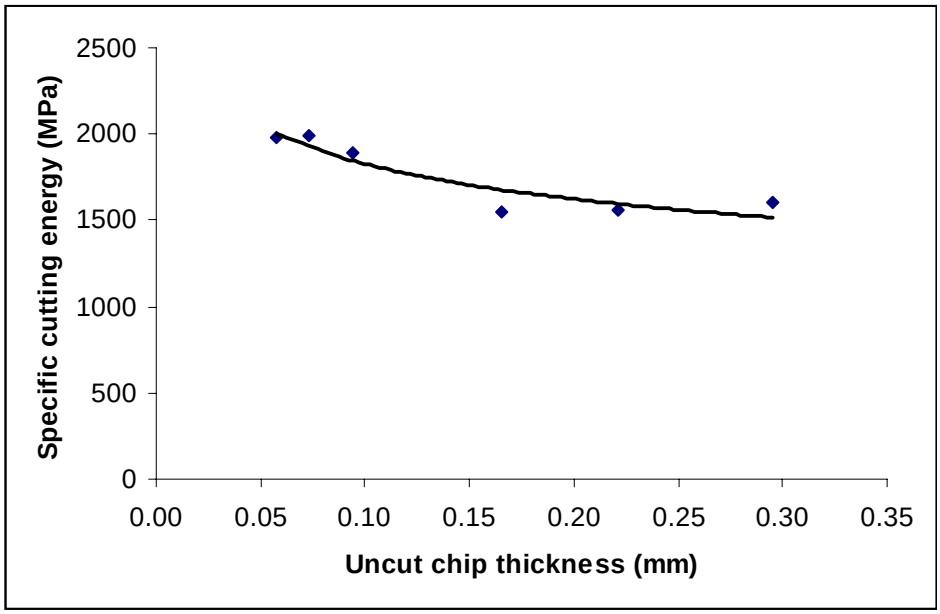

Figure 2.1. Experimental specific cutting energy versus uncut chip thickness (SAE 1112 steel) [12].

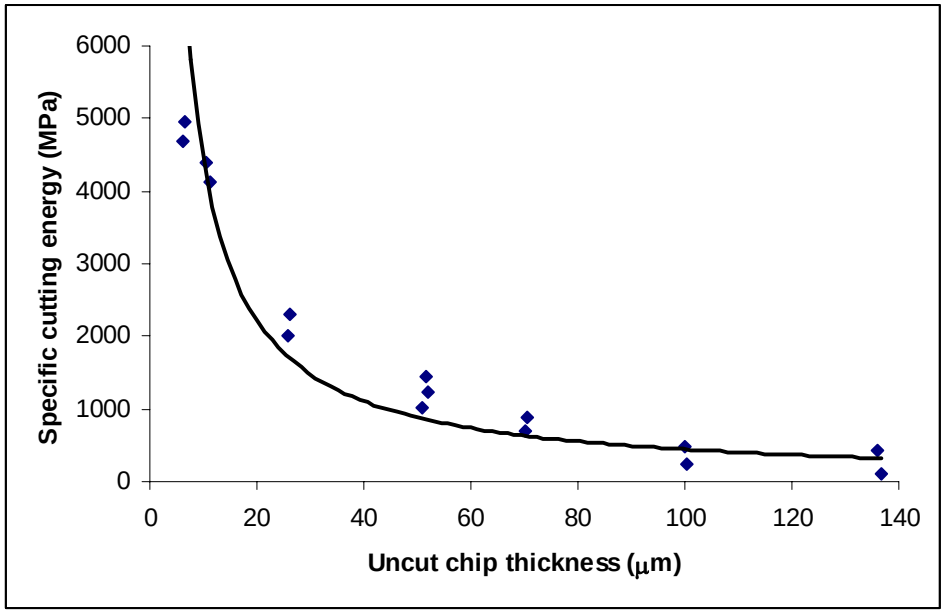

Figure 2.2. Experimental specific cutting energy versus uncut chip thickness (plain carbon steel) [13].

Kopalinsky and Oxley [13] conducted turning tests on plain carbon steel of chemical composition 0.48%C, 0.3%Si, 0.13%S, 0.8%Mn and 0.019%P. The cutting tool used was black ceramic indexable tip with -5 degree rake angle and 2 degree clearance angle. The cutting edge radius of the tool was ground by a fine grit diamond wheel to a radius much smaller than 6 μm, which was the smallest value of uncut chip thickness used in their tests. A cutting speed of 420 m/min was used. Their results, reproduced in Figure 2.2, also show a clear nonlinear scaling effect in the specific cutting energy with decrease in uncut chip thickness.

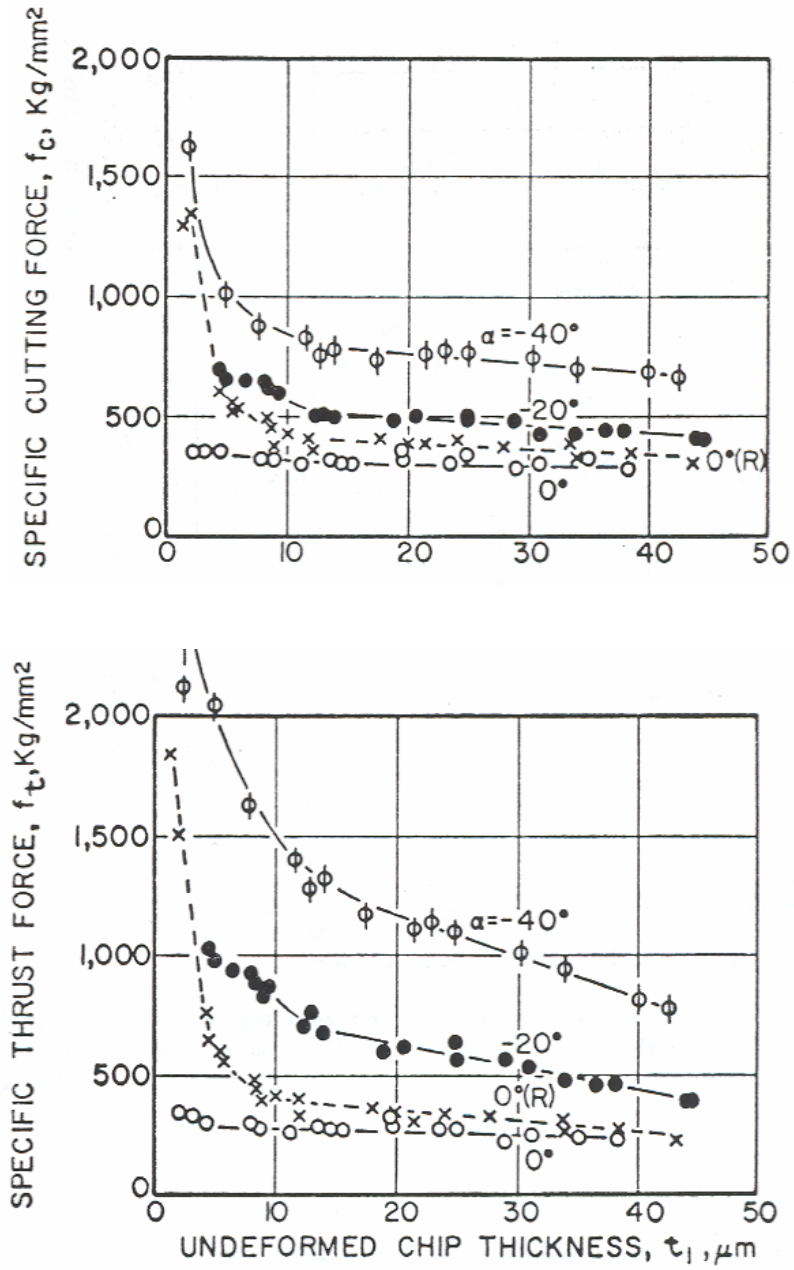

Figure 2.3. Experimental specific cutting energy versus uncut chip thickness (workpiece material brass, cutting speed V_c = 0.1 m/min) [14].

Nakayama and Tamura [14] performed an experimental investigation on orthogonal cutting of brass. The cutting speed was kept at 0.1 m/min in all their tests.

This speed was slow enough to avoid thermal and strain rate effects. High speed steel tools with an edge radius of 3~4 μm at different rake angles (0º, -20º, -40º) were used. Figure 2.3 shows their results. The size effect in the specific cutting and thrust forces is clearly evident at low cutting speed of 0.1 m/min.

Lucca et al. [15] conducted an experimental study of the effect of single crystal diamond tool edge geometry on the resulting cutting and thrust forces and specific energy in ultraprecision flycutting. Edge radii of newly sharpened single crystal diamond tools were measured in an atomic force microscope by scanning the AFM cantilever tip across the diamond tool edge normal to the rake and flank faces. Single crystal diamond tools with edge radius of 0.25 μm (±0.02μm) at different rake angles (0º, -10º, -20º and -30º) were used for cutting Te-Cu, which has a nominal chemical composition of 99.4-99.5% Cu and 0.5-0.6% Te. The experiments were conducted at a cutting speed of 7.6 m/min with the uncut chip thickness ranging from 20μm down to 10 nm. Their results, shown in Figure 2.4, clearly demonstrate the size effect in the specific cutting energy.

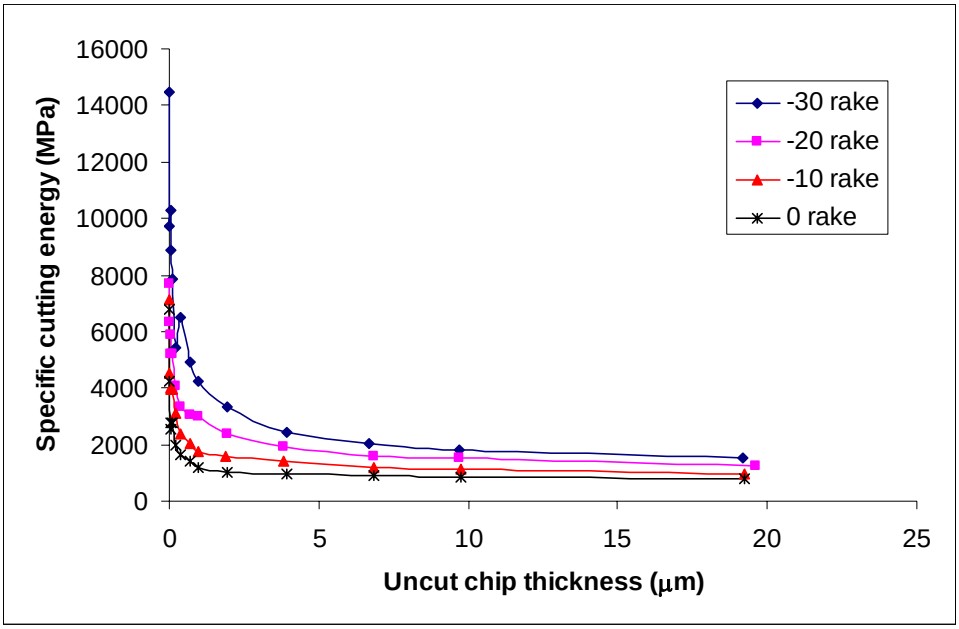

Figure 2.4. Experimental specific cutting energy versus uncut chip thickness (workpiece material Te-Cu) [15].

Furukawa et al. [16] also reported the presence of size effect in the specific cutting energy (see Figure 2.5) over an uncut chip thickness ranging from 0.5 to 10 μm in their investigation of micro-cutting of several different materials including Aluminum alloy, Oxygen Free Copper, Germanium, Fluorite (CaF_2) and Acryl resin (PMMA). The aluminum alloy is considered to be isotropic in a macro sense. Germanium is difficult to finish precisely because of its high hardness and brittleness. Fluorite is a single crystal used for ultraviolet ray components, and is not very hard but is very brittle. Acryl resin is a soft amorphous material used for optical components. A single crystal diamond tool with 0 degree rake angle and 2~3 degree relief angle was used at a cutting speed of 6 m/min.

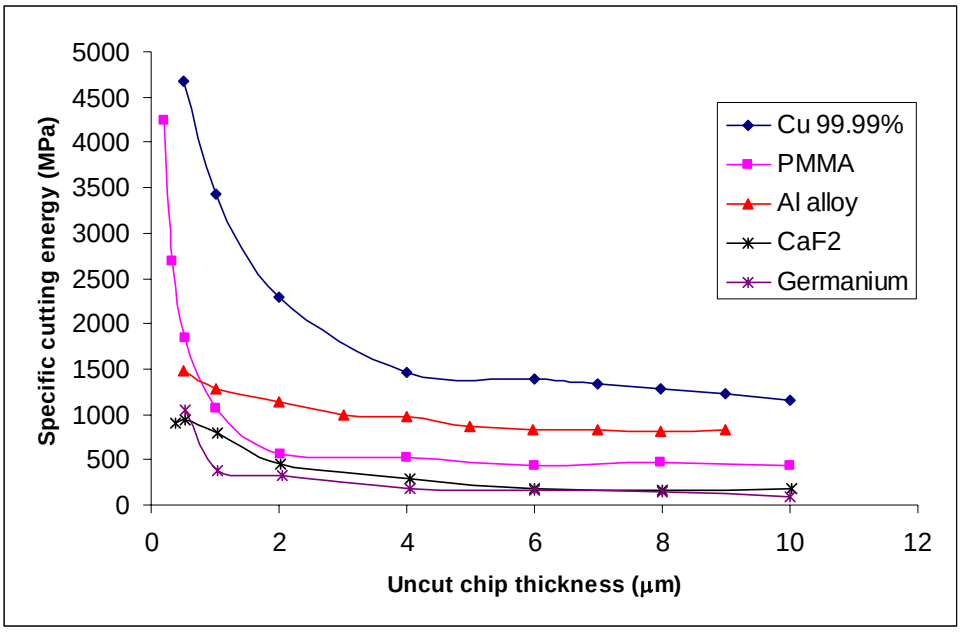

Figure 2.5. Experimental specific cutting energy versus uncut chip thickness [16].

Schimmel and Endres [17] and Kountanya [18] investigated the effect of tool edge geometry on cutting forces in orthogonal cutting with different edge radius cutting tools. Orthogonal cutting experiments were performed on materials such as pure zinc, cast iron and Al-2024 at a cutting speed of 56.4 m/min, with carbide tools having edge radii ranging from a few microns to a few hundred microns. Figure 2.6 reproduces their results and the nonlinear scaling effect is clearly visible.

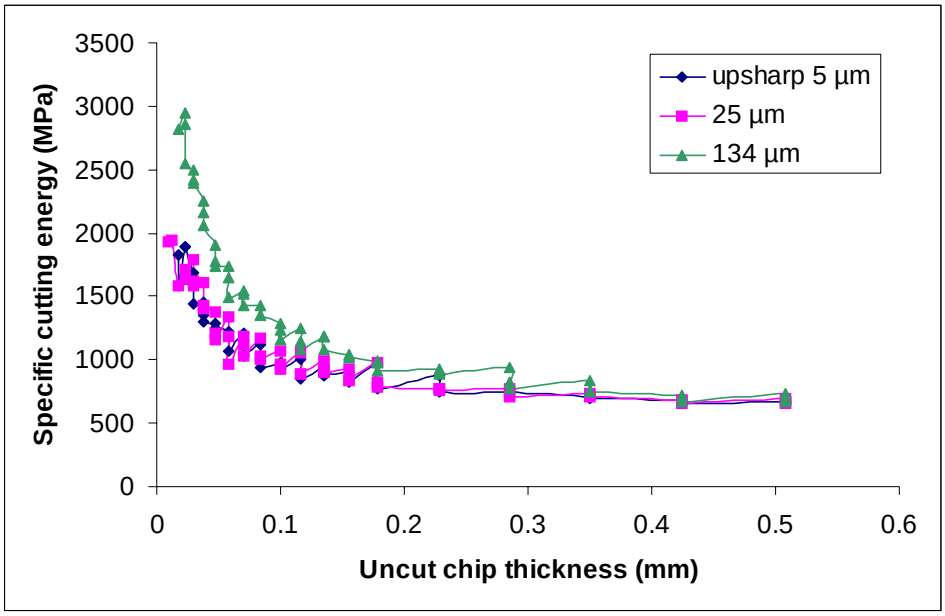

Figure 2.6. Experimental specific cutting energy versus uncut chip thickness (workpiece material pure zinc) [18].

Several efforts have been made to explain and predict the size effect in micro-cutting. Most of the explanations offered to date can be classified as follows: 1) Material strengthening due to factors that vary with the uncut chip thickness, 2) Sub-surface deformation of the workpiece material, 3) Tool edge radius effects, and 4) Energy required to create new surfaces via ductile fracture.

Shaw and Backer et al. [12] attributed the size effect to crystallographic defects such as grain boundaries, missing and impurity atoms, etc. They argued that since a significantly reduced number of imperfections are encountered when deformation takes place in a small volume, the material strength would be expected to increase and approach the theoretical strength.

Larsen-basse and Oxley [25] explained the scaling phenomenon in machining in terms of the strain-rate sensitivity of the workpiece material. Their reasoning is based on

empirical data drawn from experiments on plain carbon steel, which suggest that the maximum shear strain rate within the primary shear zone is inversely proportional to the uncut chip thickness. Therefore, a decrease in the uncut chip thickness will leave the strain occurring in the shear zone unchanged but the strain rate will increase inversely with the uncut chip thickness *t*. For most metals, an increase in the strain rate causes an increase in the flow stress with the strain-rate sensitivity of flow stress increasing rapidly in the range applicable to machining processes. This could therefore explain the increase in specific cutting energy with reduction in uncut chip thickness.

Kopalinsky and Oxley [13] took into account the effect of temperature in later work and attributed the size effect in the specific cutting force to a decrease in the shear plane angle due to decrease in the tool-chip interface temperature. This, they contended, leads to an increase in the shear strength of the workpiece material. Furthermore, they acknowledge that the temperature effect does not explain the size effect observed at uncut chip thickness less than 50 μm, which is possibly because of the increasing sensitivity of flow stress to strain rate within this range. Marusich [26] also offers a similar explanation based on finite element simulations of orthogonal cutting at very high cutting speeds. Fang [27] recently presented a complex slip line model for orthogonal machining and attributed the size effect to the material constitutive behavior of varying shear flow stress with uncut chip thickness.

Nakayama and Tamura [14] analyzed size effect in machining through micro-cutting experiments performed at a very low cutting speed (0.1m/min) to minimize temperature and strain rate effects. They observed plastic flow in the subsurface layer of the workpiece and suggested that its contribution to size effect becomes important with

reduction in the uncut chip thickness. The main cause of this subsurface plastic flow is believed to be the extension of the shear zone below the machined surface. Therefore, they attribute the size effect to the fact that the energy consumed in plastic flow in the subsurface layer is not proportional to the uncut chip thickness and to the decrease in shear angle with a decrease in the uncut chip thickness.

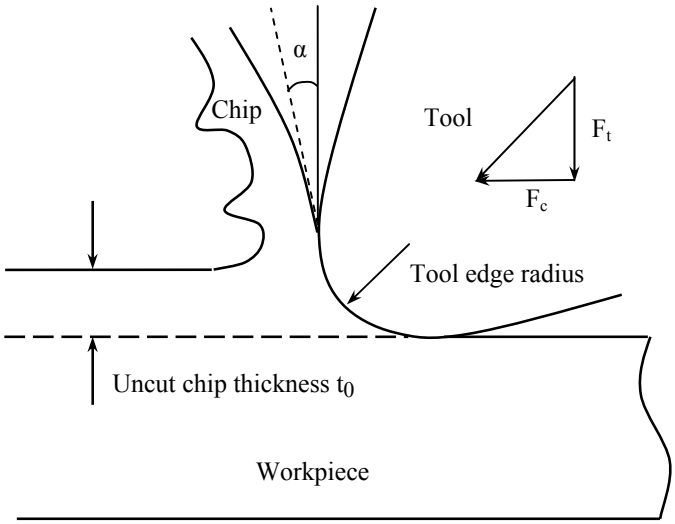

Figure 2.7. Illustration of effective negative rake angle and resultant force vector at small uncut chip thickness.

Kim et al. [28] analyzed the effect of the tool edge radius on the cutting process using the finite element method. The model is based on an Eulerian formulation with tools of finite edge radius and a rigid-viscoplastic workpiece material. The cutting forces obtained from their finite element simulation are found to be in good agreement with their experimental data. They therefore concluded that the major cause of size effect is the tool edge radius. Lucca et al [15] studied the role of the effective negative rake angle induced by the tool edge radius (see Figure 2.7), when it becomes comparable to the uncut chip thickness. As the uncut chip thickness is decreased, a rotation of the resultant

force vector downward toward the workpiece is observed. The thrust force becomes the dominant component below a certain uncut chip thickness value. They suggest that the process can be thought of as transitioning from a cutting dominant process to a plowing/sliding indentation-dominant process when the uncut chip thickness is reduced. They attribute the size effect to the increasingly dominant plowing process. Similarly, Armarego and Brown [29] suggested that the increase in specific cutting force with decrease in uncut chip thickness was due to the greater relative contribution of the ploughing force arising from frictional rubbing and ploughing associated with material removal by a blunt tool.

Masuko [30] introduced the concept of an additional indenting force component necessary to cause the cutting edge to penetrate the workpiece as an indenter. The indenting force component R_n is shown in Figure 2.8. Since this force should be independent of the uncut chip thickness, he concluded that this indenting force was responsible for the size effect.

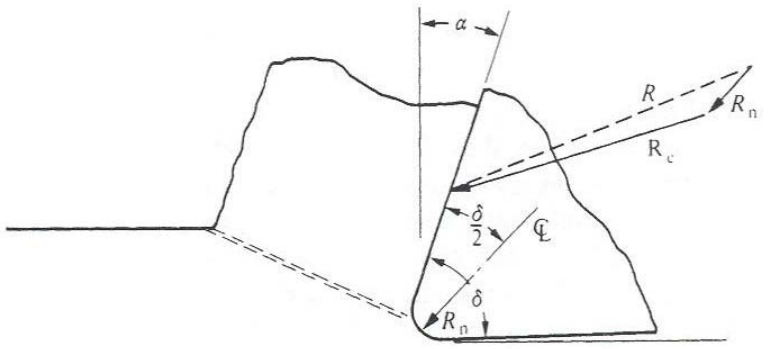

Figure 2.8. Illustration of additional indenting force component [29].

Komanduri [31] also reported size effect due to tool edge radius at nanometer length scales by carrying out molecular dynamics simulations of orthogonal cutting at depths of cut of 0.362~12.172 nm and tool edge radii of 3.62~21.72 nm.

Recent work by Atkins [32] attributes the size effect in cutting to the energy required for new surface creation via ductile fracture. The author found that the work associated with separation criteria in finite element models is close to the typical value of fracture toughness for the material in ductile fracture mechanics. He suggested that the energy required for the formation of new surface should not be considered negligible in metal cutting analysis. This energy is independent of the depth of cut and consequently its contribution to the overall specific energy should increase at small uncut chip thickness values.

It is clear from the literature that the size effect in micro-cutting may arise due to multiple mechanisms. It is also clear that the size effect can arise when cutting with sharp tools [15] and when the effects of temperature and strain rate are negligible (i.e. at very low cutting speeds) [14]. Of the foregoing reasons based on material strengthening, none account for the influence of the steep strain gradients present in cutting at small depths of cut.

Table 2.1. Analogy between micro/nano-indentation and machining process [33].

Machining / Indentation Analogy		
	Indentation	Machining
Shear strain	$\gamma \approx 0.36$	$\gamma \approx 2\sim5$
Strain Gradient	$\eta = 4\gamma / D$	$\eta = 4\gamma / t$
Hardness or specific force	$H = C'Gb\sqrt{\rho_s + (4\gamma / bD)}$	$H \approx AGb\sqrt{\rho_s + (4\gamma / bt)}$
Characteristic length of deformation field	Indentation diameter, D	Uncut chip thickness, t

Recently, Dinesh et al. [33] linked the size effect observed in micro-/nano-indentation to that in machining. The increase in hardness of a metallic material with decrease in indentation depth is a consequence of the dependence of the flow stress of the metal on the strain gradient. They suggested that the size-effect in machining can also be explained by the theory of strain-gradient plasticity since strain gradients in machining are very intense. Building upon the work in [33], Joshi and Melkote [34] presented an analytical model for orthogonal cutting that incorporates a material constitutive law with strain gradient effects. However, their model only considers strain gradient produced in the primary shear zone.

Gradient plasticity appears to be the missing factor that is fundamental to developing a better understanding of the size effect due to material strengthening at very small values of uncut chip thickness. Consequently, the development of a strain gradient based finite element model for microscale cutting process forms the focus of this work.

2.2 Finite Element Modeling of Machining Processes

In 1944, Merchant [35] proposed the first analytical model that laid the framework for modeling of orthogonal machining processes. With the invention of the computer and the following rapid growth in computing power, finite element techniques have been widely used by investigators [36-46] with notable success in modeling the machining process. Previous work in finite element modeling of machining is reviewed in this section.

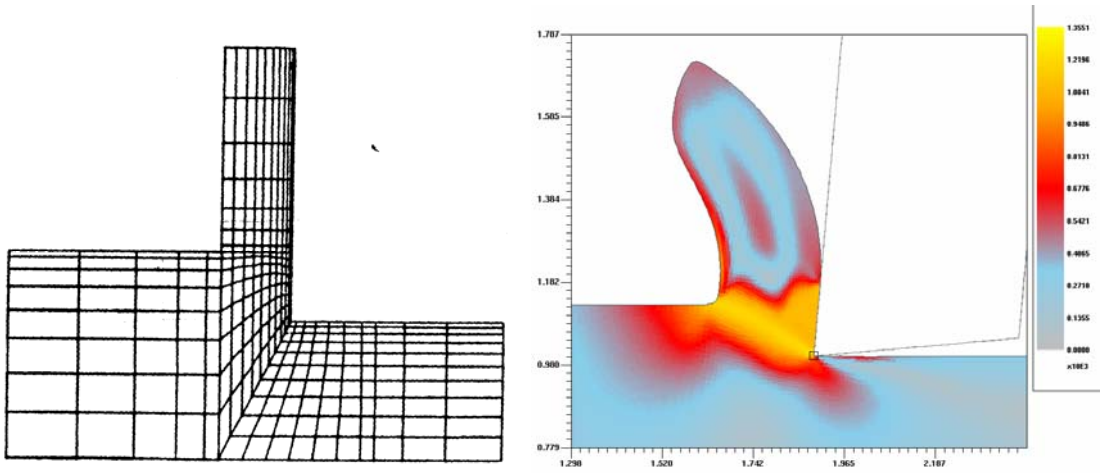

(a) Eulerian formulation (b) Lagrangian formulation

Figure 2.9. Illustration of Eulerian and Lagrangian formulations.

Two finite element formulations, Eulerian and Lagrangian, have been commonly used in the past to simulate machining processes [36-46]. In the Eulerian formulation (see Figure 2.9a), the finite element grid through which the material flows is fixed in space. The advantage of the Eulerian formulation is that the shapes of the elements do not change with time so that element distortion does not take place. However, an initial shape of the free surface of the chip has to be assumed and chip formation process cannot be

modeled. On the other hand, the Lagrangian method (see Figure 2.9b) involves a moving frame of reference. The mesh is attached to the material so that it moves along with the material. However, the elements change shape during the material flow and, in extreme cases, it may become necessary to replace the distorted elements by remeshing. Therefore, mesh rezoning or adaptive meshing is often required for these types of formulations [47]. In addition, a chip separation criterion needs to be specified to simulate chip formation [47].

Although the Eulerian approach possesses the advantage of no element distortion, it can only be used for steady-state analysis and cannot strictly model chip formation. With recent advances in hardware and software, an arbitrary Lagrangian-Eulerian formulation [48-52], which is a finite element formulation that lies between the pure Eulerian formulation and the pure Lagrangian formulation, is used by most of the major software packages such as ABAQUS®, DEFORM® for modeling material removal processes. In an arbitrary Lagrangian-Eulerian formulation, the mesh points move but not necessarily with the material. While the finite element mesh spans the complete analysis domain throughout the solution and its boundaries move with the movements of free surfaces and structural boundaries, the material moves relative to the mesh points. This approach is suitable for modeling large deformation processes, general free surfaces and interactions between fluid flows and structures. In light of this, the arbitrary Lagrangian-Eulerian method is chosen and will form the backbone of the proposed work.

Fully coupled thermal-stress analysis is needed when the stress analysis is dependent on the temperature distribution and the temperature distribution depends on the stress solution. Since machining problems include significant heating due to inelastic

deformation, which in turn changes the material properties, thermo-mechanical modeling is required to obtain stress, strain and temperature solutions simultaneously as the material is being cut.

Finite element modeling machining is greatly influenced by the flow stress characteristics of the material in different cutting regimes. It is a well-known fact that the flow stress of the material is a function of the strain, strain rate and temperature [53]. A number of finite element studies [52, 54-57] have used the empirical flow stress equations combining power law strain hardening, power law or logarithmic strain-rate effects and linear or power law thermal softening and the most popular formulation is that of Johnson and Cook. Several modeling studies have shown the effectiveness of this material flow stress model [52, 54-57].

In recently reported micro- and nano-indentation tests, remarkable material strengthening behavior has been observed and this size dependence cannot be explained by the classical continuum plasticity theory. Based on the notion of geometrically necessary dislocations in dislocation mechanics, strain gradient plasticity theories have been proposed where strain gradient dependence of flow stress is introduced into the material constitutive model, e.g., Fleck and Hutchinson [22, 58], Gao and Huang [59], Acharya and Bassani [60].

At the typical length scales of micro-cutting, since the depth of cut becomes comparable to the size of crystal grains, the effect of tool and workpiece anisotropy on micro-cutting process has been investigated by Zhou et al. [61] and Liang et al. [62]. Chuzhoy et al. [63] developed a finite element model for the orthogonal cutting of ductile iron taking into account the various phases of iron. This is the first attempt of finite

element modeling at the microstructure level to account for the heterogeneity of the workpiece material.

An important feature of the micro-cutting process is that the tool edge radius is often comparable to the uncut chip thickness causing the effective rake angle to be negative. Kim et al. [28] and Yen [64] have considered tool edge geometry effects.

For the calculation of temperature distribution, Jaeger's moving heat source model [65] has been used by the majority of investigators [28, 38, 42, 48, 66, and 67]. Interaction between the chip and workpiece has been alternatively modeled as a simple Coulomb friction type interaction consisting of stick and slip regimes [39, 49, 67] or as a continuous relationship between frictional and normal components [40].

A critical aspect of finite element based simulation of the cutting process is the specification of a chip separation criterion. Different types of chip separation techniques have been used in machining simulation and they basically fall into three categories. Node separation technique [38, 68-70] is geometry-based. A predefined parting line is used to separate the chip layer from the workpiece. At each point on the parting line, two nodes are tied together initially and share the same degrees of freedom. When the tool approaches the tied pair of nodes, the nodes separate when a pre-specified criterion is met. The commonly used criteria are the tool node distance, critical effective stress, and critical effective plastic strain. Element deletion technique [57] is also a geometry-based technique in which the chip layer is predetermined by a sacrificial element layer. This sacrificial element layer is positioned at the bottom of the chip layer. When the tool approaches a sacrificial element, the element is deleted based on a criterion such as the critical effective plastic strain or critical energy density. The major disadvantage of both

methods is that the chip is forced to separate along a pre-determined line. Hence, chip formation is not a natural product of the machining process.

More recently the pure deformation technique [49-50, 52] has become popular with the aid of remeshing techniques. It involves no chip separation criterion since it treats the metal cutting process like an indentation process, or a pure deformation process. There is no pre-defined parting line and therefore the shape of the chip is not pre-determined. There is also no node separation or element removal involved in this method. Instead, as the tool advances, nodes of the workpiece move on the tool surface and the elements may deform strongly close to the tool tip. The severely distorted elements are replaced by new elements that are more regular in shape. The material that overlaps with the tool is removed during the remeshing step.

The use of fracture to determine chip separation is controversial since there is no consensus in the literature on whether chip formation indeed occurs by fracture or not [24, 124]. Considering this, the pure deformation technique is the most favorable, in terms of ease of implementation as well as veracity of the results.

Based on the above review, it can be concluded that fully thermo-mechanical coupled models using arbitrary Lagrangian-Eulerian finite element formulations have been successfully developed for macro-scale machining simulation. It is selected in this dissertation as the platform for process modeling of micro-cutting where size effects are dominant. So far no detailed model (finite element or other) is currently available to simulate chip formation in a micro-cutting process, especially one that accounts for strain gradient strengthening and its contribution to size effect. Therefore, the following section gives an overview of strain gradient plasticity theory.

2.3 Strain Gradient Plasticity

Conventional local continuum mechanics assumes that stress at a material point is a function of state variables, such as strain, at the same point. This local assumption has long been proved to be adequate when the wavelength of the deformation field is much larger than the dominant microstructural length scale of the material. However, when the two length scales are comparable, the assumption is questionable as the material behavior at a point is influenced by the deformation of neighboring points. There is ample experimental evidence to indicate that there is a significant dependence of the material behavior on additional length/size parameters [19-23]. Figure 2.10 shows several plasticity theories and the corresponding typical minimum explicit length scale of resolution. Therefore, a generalized continuum theory that incorporates internal length scales or higher-order continuum structure will allow the inclusion of small length scale physics and eliminate mesh dependency in numerical solutions. Among diverse approaches to introduce the generalized continuum are: non-local (or gradient) continuum theory [71], micropolar (or cosserat) continuum theory [72] and rate dependent continuum [73].

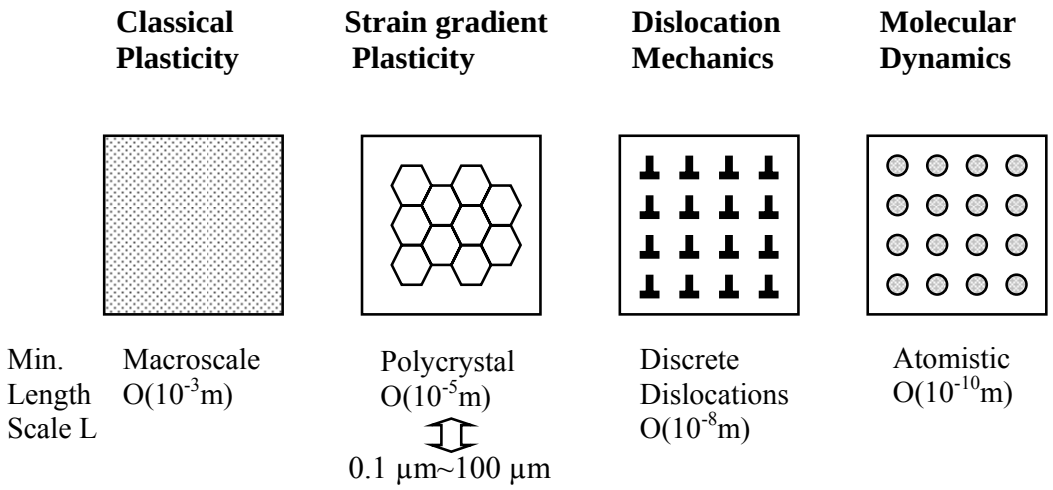

Figure 2.10. Plasticity theories and typical minimum explicit length scale of resolution at each scale [74].

In strain gradient plasticity, length scales are introduced through the coefficients of spatial gradients of strain components. Strain gradient plasticity is motivated by microscopic understanding of plasticity relating to dislocations. When a material is deformed, dislocation are generated, moved and stored in two ways. Statistically stored dislocations accumulate by trapping each other in a random way, while the geometrically stored dislocations are required for compatible deformation. Geometrically stored dislocations can be related to the gradient of plastic strain in material. Plastic strain gradients appear either because of geometry of loading or because of inhomogeneous deformation [22].

A first attempt to incorporate length scale effects in elasticity was made by Toupin [72], Koiter [75] and Mindlin [76], who considered strain gradient elasticity theories, in which the elastic strain energy density is a function of strain as well as strain and rotation gradients. An independent rotation quantity θ was defined in addition to the material displacement u and couple stresses were introduced as the work conjugate to the

micro-curvature. Later, Mindlin [77] proposed a more general theory that includes not only micro-curvature, but also gradients of normal strain.

Fleck and Hutchinson [58] and Fleck et. al [22] extended Toupin and Mindlin's theory by including plasticity in their model. Multi-length parameters are introduced to account for the size effect at the micron scale. They later reformulated their strain gradient plasticity to employ only the displacement components and plastic strain as the primary variables in the variational statement of the boundary value problems [78]. Avoiding the second gradient of the primary variables, the new version [78] has an advantage over the earlier theory [58] in numerical implementation and in representation of elastic behavior.

Aifantis [79, 80] and Zbib and Aifantis [81] introduced an internal length scale by including second- and fourth-order strain gradients into the yield condition of plasticity. The higher-order strain gradients allowed them to account for the thickness, spacing, and velocity of shear bands in metals.

Acharya and Bassani [60] have considered possible formulations of strain gradient plasticity that retain the essential structure of conventional plasticity and obey thermodynamic restrictions. Their proposed formulation is a flow theory with strain gradient effects represented as an internal variable which acts to increase the current tangent-hardening modulus.

Starting from the Taylor relation between the shear strength and dislocation density in a material, Nix and Gao [82] established a linear dependence of the square of the plastic flow stress on the strain gradient. They developed a dislocation model to estimate the density of geometrically necessary dislocations underneath a conical indenter

and derived a hardness formula. The estimated hardness from this formula agrees with the experimental result of depth dependence of the hardness of single crystal copper measured by McElhaney et.al [83].

Gao and Huang et al. [59] proposed an alternative formulation of strain gradient plasticity in which the Taylor hardening model is adopted as a founding principle. Their theory of Mechanism-based strain gradient (MSG) is based on a multiscale, hierarchical framework linking the microscale notion of statistically stored and geometrically necessary dislocations to the mesoscale notion of plastic strain and strain gradient. At the microscale, the Taylor hardening model in dislocation mechanics is used to characterize dislocation interactions and their effect on the flow stress. At the mesoscale the constitutive equations are constructed by averaging microscale plasticity laws over a representative cell.

Recently Gao and Huang [84] proposed a Taylor-based nonlocal theory of plasticity. Their theory is intended to link Taylor's model of dislocation hardening to a nonlocal theory of plasticity in which the density of geometrically necessary dislocations is expressed as a nonlocal integral of the strain field.

Several strain gradient plasticity based finite element formulations have been developed to verify the size effect observed in micro-indentation and microtorsion experiments. However, no strain gradient based finite element formulation has been used to analyze the size effect in micro cutting. The focus of this thesis is to develop a finite element formulation, which incorporates strain gradient plasticity in order to address the intrinsic size effect in micro cutting.

2.4 Surface Roughness Prediction in Micro-cutting

Surface roughness is principally influenced by the cutting variables, the workpiece material and the geometry of the tool. In machining, it generally consists of the following components: kinematic roughness, cutting edge roughness and roughness caused by other disruptive factors. Kinematic or theoretical roughness is a function of the relative motion between the workpiece and the tool and tool geometry. The size of the tool nose radius and the chosen feed rate determine the kinematic roughness. Kinematic surface roughness in the turning process (see Figure 2.11) is approximately given by [24],

$$R_{th} \cong \frac{f^2}{8r_n} \tag{2.1}$$

where f is the feed, r_n is the tool nose radius and R_{th} is the maximum peak-to-valley roughness height (see Figure 2.12).

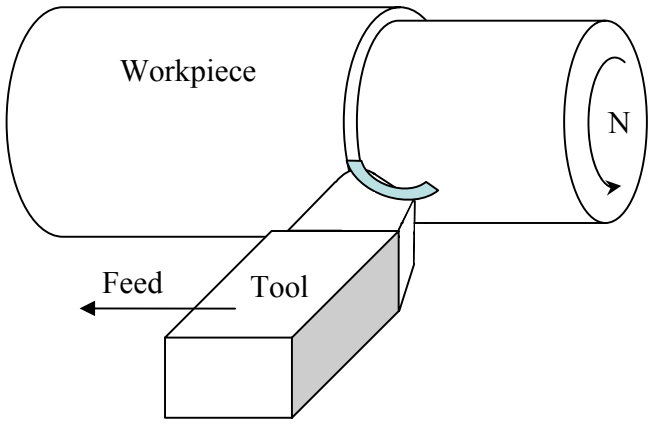

Figure 2.11. A schematic drawing of turning process.

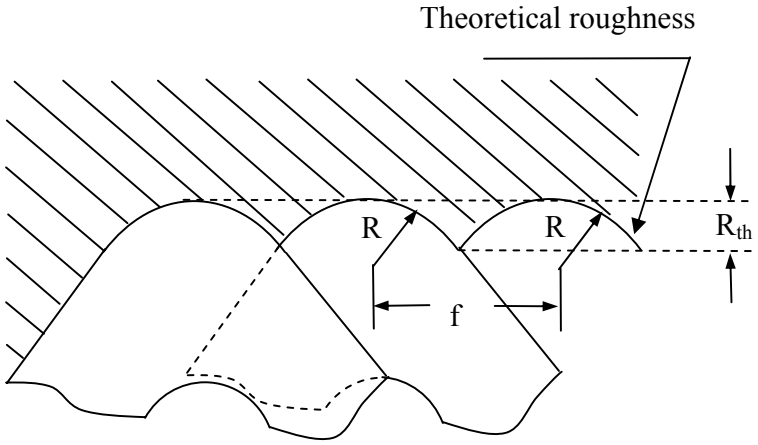

Figure 2.12. Illustration of kinematics/tool geometry induced surface roughness.

However, experimental data (see Figure 2.13) shows that the maximum surface roughness R_{exp} of the machined samples is always larger than the theoretical value estimated using Eq. (2.1), particularly at low feeds i.e. low uncut chip thickness values. The surface roughness generated in machining is known to be influenced by the plastic deformation accompanying chip formation. In micro-cutting process, surface roughness that arises from plastic roughening tends to become more important than kinematic roughness when cutting is performed at small feeds. However, prior work on surface generation in micro-cutting has not addressed this fact adequately. In particular, previous effects to model the surface generation in cutting process do not account for the effect of plastic deformation induced surface roughening.

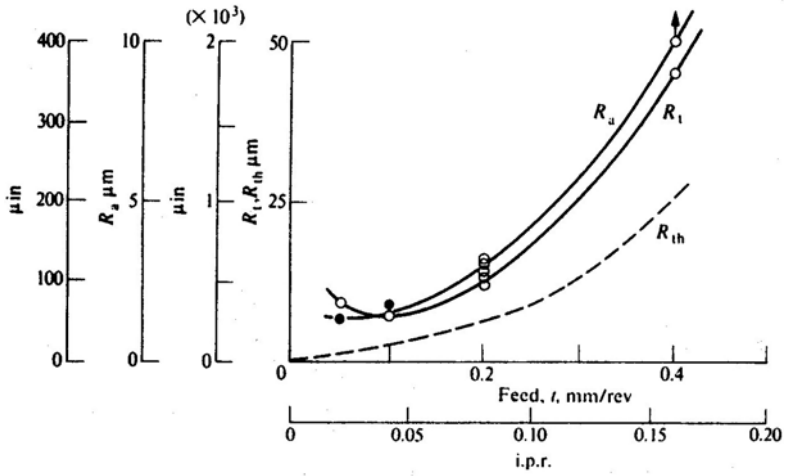

Figure 2.13. Discrepancy between theoretical roughness and measured roughness in turning of a steel [24].

It has been reported [85-89] that the surface roughness in turning is also affected by the depth of cut, cutting speed, tool wear, presence of built-up edge (BUE), workpiece hardness etc. However, due to lack of understanding of the surface roughening mechanism at the micron/submicron level and lack of physics-based surface roughness models, techniques such as regression analysis, neural network etc., are commonly employed [85-89]. In particular, the contribution of material deformation at the micron scale to surface roughening has not been accounted for in modeling the surface generation mechanism in micro-cutting process.

A few studies on roughening of free surfaces of metallic materials due to plastic deformation have been reported in sheet metal forming [90-92]. Plastic deformation roughens a free surface by producing slip bands within grains along with relative rotation and sliding among the grains. It is reported that the horizontal surface roughness parameter in terms of correlation length is proportional to a specimen's average grain

size, and the root mean square (RMS) roughness is mainly due to the relative rotation between the grains that increases linearly with the amount of plastic deformation.

The effect of material swelling in ultra-precision diamond turning has been investigated [93] and a good correlation between the surface roughness and the amount of elastic recovery has been shown. Influences of vibration [94-96] and crystallographic orientation [97] on surface roughness in diamond turning have also been investigated.

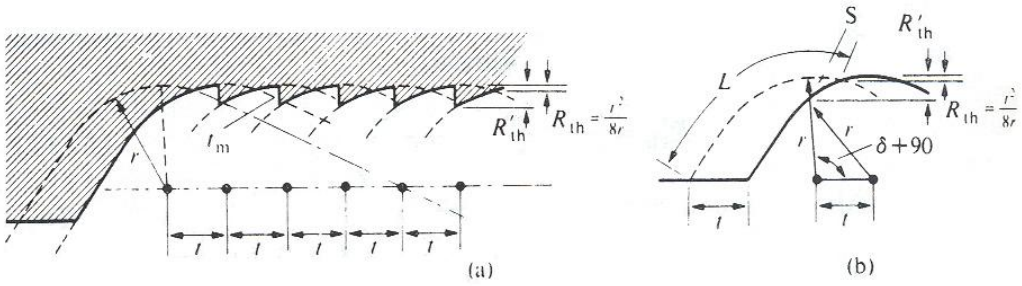

Figure 2.14. Illustration of surface roughness contribution of Spanzipfel [98].

Brammertz [98] analyzed the portion of material left behind the tool due to minimum uncut chip thickness and considered this so called "Spanzipfel" as the main source of the discrepancy between the theoretical and measured surface roughness at small feeds (see Figure 2.14). The second term in Eq. (2.2) proposed by Brammertz represents the contribution of the Spanzipfel.

$$R_{th}' = \frac{f^2}{8r} + \frac{f_m}{2}\left(1 + \frac{rf_m}{2}\right) \qquad (2.2)$$

It is also seen from Figure 2.13 that the surface roughness increases with decrease in feed after reaching a minimum. Grzesik [99] proposed a revised model based on Brammertz's work to account for this increasing trend in surface roughness below a certain feed by introducing the minimum uncut chip thickness as a function of the feed.

However, Shaw [24] suggested that the Spanzipfel will be plastically deformed and reduced in size as it comes into contact with the clearance face of the tool. He suggested that the contribution due to the plastic deformation of the material being pushed to the side by the secondary cutting edge is expected to be significant at very small values of feed and could be partly responsible for the rise in surface roughness at small feeds. He also hypothesized that the size effect in specific cutting energy at small uncut chip thickness levels had a role to play in causing the rise in roughness at small feeds. However, he did not present any model of surface generation that showed this hypothesis was true.

So far, little work has been done to analyze plastic side flow induced surface roughness in micro-cutting. In this work the effect of plastic side flow on the surface roughness in a three-dimensional micro-cutting process such as turning will be analyzed. Specifically, a model for the surface roughening due to plastic side flow in micro-turning will be developed.

2.5 Summary

The size effect in micro-machining has been reported for a number of materials and over a range of cutting conditions. Explanations proposed to explain size effect falls into categories such as material strengthening, sub-surface deformation, tool edge radius effects, and energy required to create new surface via ductile fracture. For process modeling of machining, finite element techniques have been widely used. Specifically, fully thermo-mechanical coupled model using arbitrary Lagrangian-Eulerian finite element formulations have been developed successfully for macro-scale machining simulation. The strain gradient plasticity that was recently proposed to explain the size dependence of material strength in micro/nano indentation could account for size effect in micro-cutting, which is also characterized by steep strain gradient. The review also showed that there is lack of modeling work on the prediction of surface roughness in micro-cutting. Therefore, the following conclusions can be drawn from the literature review,

- Size effect cannot be explained satisfactorily by a single mechanism. Multiple mechanisms including strain gradient strengthening could be responsible for size effect in micro-cutting. However, their relative contribution and dominance in specific cutting regimes have not been investigated.
- No numerical modeling work has considered the effects of strain gradient on size effect in the micro-cutting process.
- Discrepancy between the theoretical and measured roughness in three dimensional micro-cutting process such as micro-turning is found to be

significant at small feeds. The role of plastic side flow induced surface roughening in micro-cutting is not well understood.

CHAPTER 3

FINITE ELEMENT MODELING OF ORTHOGONAL MICRO-CUTTING

The previous chapter discussed the mechanism of size effect and surface finish generation in micro-cutting. These are the phenomenon that will be modeled using a finite element approach. In order to achieve this, a fully coupled thermo-mechanical finite element model incorporating strain gradient plasticity that represents the constitutive behavior of the workpiece material more accurately at micron/submicron level needs to be established first. This chapter details the following aspects of the finite element model: (a) Constitutive model, (b) Modeling of tool-chip interaction, (c) Modeling of chip separation, and (d) Modeling of the heat transfer. Several key techniques and the overall simulation approach employed are discussed in the latter part of this chapter.

3.1 Constitutive Model

A Taylor-based non-local theory of plasticity proposed by Gao and Huang [84] is chosen as the basis for the constitutive model used to represent the material behavior under highly localized inhomogeneous deformation in micro-machining. The rationale for choosing this formulation and its flow theory are described in the following section.

3.1.1 Choice of Strain Gradient Plasticity Formulation

Strain gradient plasticity theories proposed by Fleck and Hutchinson [22, 58], Gao and Huang [59] and Aifantis [60] involve the gradient of plastic strain in the

constitutive equations. Since strain gradients and higher order stresses enter the principle of virtual work as work conjugates, the order of the governing equations becomes higher such that additional boundary conditions must be imposed. The strain gradient quantities are the second-order spatial derivatives of displacement. Therefore, in order to guarantee convergence of a displacement-based finite element analysis upon mesh refinement, the interpolation of displacement should exhibit C1-continuity i.e. both displacement and its first order derivatives must be continuous across inter-element boundaries. Another solution is to employ a mixed formulation which takes the higher order terms as extra nodal degrees of freedom [100-101]. These difficulties in numerical implementation make these higher order theories unattractive and prohibit their application. In comparison with the above higher order theories, the Taylor based nonlocal theory of plasticity by Gao and Huang [84] retains the same order as classical continuum theories. A nonlocal theory does not require additional boundary conditions and the length scale is introduced into the constitutive equations via nonlocal variables expressed as an integral of local variables over all the material points. The key feature of the Taylor-based non-local theory of plasticity is that it does not involve higher order terms and preserves the structure of classical continuum mechanics. Strain gradient enters the constitutive model as a non-local integral and affects the flow stress variation. Thus, it has the advantage of simpler implementation compared to other gradient plasticity theories [22, 58-60].

Therefore, Taylor based nonlocal theory of plasticity is chosen to be the basis of the constitutive model in the present work.

3.1.2 Non-local Theory Formulation

From the viewpoint of dislocation mechanics, the metal material is work hardened due to the formation, motion and interaction of dislocations. Statistically stored dislocations accumulate by trapping each other in a random manner while geometrically necessary dislocations are required for compatible deformation and are related to the gradient of plastic strain. This theory links Taylor's model of dislocation hardening to a non-local theory of plasticity in which the density of geometrically necessary dislocations is expressed as a non-local integral of the strain field. Preserving the structure of classical continuum theory, the balance law of the theory, i.e. the balance of angular and linear momentum, is identical to the classical theories. The Taylor dislocation model defines the shear flow stress τ in terms of the dislocation density ρ as $\tau = \alpha G b \sqrt{\rho}$, where the dislocation density ρ is composed of the density of statistically stored dislocations, ρ_s, and the geometrically necessary dislocations, ρ_g, α is an empirical factor ranging from 0.1~0.5, G is the shear modulus and b is the Burgers vector.

The density of statistically stored dislocation, ρ_s, can be determined from the uniaxial stress-strain law in the absence of strain gradient effects as,

$$\sigma = 3\alpha G b \sqrt{\rho_s} = \sigma_{ref} f(\varepsilon, \dot{\varepsilon}, T) \tag{3.1}$$

where σ_{ref} is the reference stress in uniaxial tension and $f(\varepsilon, \dot{\varepsilon}, T)$ is the flow stress of the workpiece material. On the other hand, the density of geometrically necessary dislocations, ρ_g, can be related to the effective strain gradient η as,

$$\rho_g = 2\eta / b \tag{3.2}$$

Based on these equations, a flow stress equation accounting for the effect of geometrically necessary dislocations can be written as,

$$\sigma = \sigma_{ref} \sqrt{f^2(\varepsilon, \dot{\varepsilon}, T) + l\eta} \tag{3.3}$$

where l is the material length scale and is given as [84],

$$l = 18\alpha^2 \left(\frac{G}{\sigma_{ref}} \right)^2 b \tag{3.4}$$

The flow stress function, f, is assumed to be of the Johnson-Cook [53] form as follows:

$$f(\varepsilon, \dot{\varepsilon}, T) = (A + B\varepsilon^n)\left(1 + C \ln \frac{\dot{\varepsilon}}{\dot{\varepsilon}_o}\right)\left(1 - (T^*)^m\right) \tag{3.5}$$

The strain gradient tensor is defined as,

$$\eta_{ijk} = u_{k,ij} = \varepsilon_{ik,j} + \varepsilon_{jk,i} - \varepsilon_{ij,k} \tag{3.6}$$

The effective strain gradient, which measures the density of geometrically necessary dislocations, is defined as,

$$\eta = \sqrt{\frac{1}{4} \eta'_{ijk} \eta'_{ijk}} \tag{3.7}$$

where the third order deviatoric strain gradient tensor η'_{ijk} is given by,

$$\eta'_{ijk} = \eta_{ijk} - \frac{1}{4}\left(\delta_{ik}\eta_{jpp} + \delta_{jk}\eta_{ipp}\right) \tag{3.8}$$

Writing the strain gradients as a nonlocal integral of strains, the density of geometrically necessary dislocations ρ_g can be linked to the strain gradient in such a way that it can be calculated from the strains without having to resort to the mesoscale.

Consider the Taylor expansion of a strain component ε_{ij} in the neighborhood of the point x,

$$\varepsilon_{ij}(x+\xi) = \varepsilon_{ij}(x) + \varepsilon_{ij,m}\xi_m + O(|\xi|^2) \tag{3.9}$$

where ξ denotes the local coordinates centered at x. For a 2-dimensional problem, integrating Eq. (3.9) with ξ_k over a small representative area A_{cell} containing x gives,

$$\int_{Acell} \varepsilon_{ij}(x+\xi)\xi_k dA = \varepsilon_{ij}(x)\int_{Acell} \xi_k dA + \varepsilon_{ij,m}\int_{Acell} \xi_k \xi_m dA \tag{3.10}$$

where the characteristic size, l_ε, of A_{cell} is assumed to be sufficiently small that higher order terms in l_ε are negligible. Therefore, the gradient term $\varepsilon_{ij,k}$ can be expressed in terms of an integral of strain ε,

$$\varepsilon_{ij,k} = \int_{Acell} \left[\varepsilon_{ij}(x+\xi) - \varepsilon_{ij}(x)\right]\xi_m dA\left(\int_{Acell} \xi_k \xi_m dA\right)^{-1} \tag{3.11}$$

where $\left(\int_{Acell} \xi_k \xi_m dA\right)^{-1}$ is the inverse of $\int_{Acell} \xi_k \xi_m dA$. In the case of a square representative cell centered at x, Eq (3.11) reduces to

$$\varepsilon_{ij,k} = \frac{1}{I_\varepsilon}\int_{Acell} \varepsilon_{ij}\xi_k dA \tag{3.12}$$

where I_ε is the moment of inertia of the cell and is related to the edge length l_ε of the cube as follows,

$$I_\varepsilon = \int_{Acell} \xi_1^2 dA = \frac{1}{12} l_\varepsilon^4 \tag{3.13}$$

Using Taylor series expansion of the strain components [84], the deviatoric strain gradient η'_{ijk} is obtained as the following non-local area integral,

$$\eta'_{ijk} = \int_A \left[\varepsilon_{ik}\xi_j + \varepsilon_{jk}\xi_i - \varepsilon_{ij}\xi_k - \frac{1}{4}(\delta_{ik}\xi_j + \delta_{jk}\xi_i)\varepsilon_{pp}\right] dA\left(\int_A \xi_m \xi_k dA\right)^{-1} \tag{3.14}$$

3.1.3 Flow Theory of Taylor-based Nonlocal Plasticity

In the flow theory of Taylor-based nonlocal plasticity, the constitutive equations are expressed in rate form. The strain rates can be decomposed into a volumetric part and a deviatoric part as

$$\dot{\varepsilon}_{ij} = \frac{1}{3}\dot{\varepsilon}_{kk}\delta_{ij} + \dot{\varepsilon}'_{ij} \tag{3.15}$$

where the volumetric strain rate is purely elastic and is related to the hydrostatic stress rate $\dot{\sigma}_{kk}$ as

$$\dot{\varepsilon}_{kk} = \frac{\dot{\sigma}_{kk}}{3K} \tag{3.16}$$

The deviatoric strain rate consists of an elastic and a plastic part,

$$\dot{\varepsilon}'_{ij} = \dot{\varepsilon}^{e'}_{ij} + \dot{\varepsilon}^{p}_{ij} \tag{3.17}$$

where the elastic strain rate $\dot{\varepsilon}^{e'}_{ij}$ is proportional to the deviatoric stress rate $\dot{\sigma}'_{ij}$ via the shear modulus μ,

$$\dot{\varepsilon}^{e'}_{ij} = \frac{\dot{\sigma}'_{ij}}{2\mu} \tag{3.18}$$

The plastic strain rate $\dot{\varepsilon}^{p}_{ij}$ is proportional to the deviatoric stress $\sigma'_{ij} = \sigma_{ij} - \sigma_{kk}\delta_{ij}/3$ by the association rule

$$\dot{\varepsilon}^{p}_{ij} = \lambda\sigma'_{ij} \tag{3.19}$$

with the coefficient λ given by

$$\lambda = \left(\frac{\dot{\varepsilon}^{p}_{ij}\dot{\varepsilon}^{p}_{ij}}{\sigma'_{ij}\sigma'_{ij}}\right)^{\frac{1}{2}} = \frac{3\dot{\varepsilon}^{p}}{2\sigma_e} \tag{3.20}$$

where

$$\dot{\varepsilon}^p = \sqrt{\frac{2}{3}\dot{\varepsilon}_{ij}^p \dot{\varepsilon}_{ij}^p} \tag{3.21}$$

is the effective plastic strain rate and $\sigma_e = \sqrt{3\sigma'_{ij}\sigma'_{ij}/2}$ is the effective stress. Combining Eqs. (3.17) – (3.20) leads to

$$\dot{\sigma}'_{ij} = 2\mu\left(\dot{\varepsilon}'_{ij} - \frac{3\dot{\varepsilon}^p}{2\sigma_e}\sigma'_{ij}\right) \tag{3.22}$$

The effective plastic strain ε^p is obtained from the effective plastic strain rate $\dot{\varepsilon}^p$ as

$$\varepsilon^p = \int \dot{\varepsilon}^p dt \tag{3.23}$$

For the flow theories of plasticity, it is useful to write the uniaxial stress-strain relation in terms of the plastic strain ε^p as

$$\sigma = \sigma_{ref} f\left(\varepsilon^p, \dot{\varepsilon}^p, T\right) \tag{3.24}$$

where f is a function of plastic strain, strain rate and temperature, and it is related to the elastic-plastic uniaxial stress-strain relation $\sigma = \sigma_{ref} f(\varepsilon)$ as follows,

$$f\left(\varepsilon^p, \dot{\varepsilon}^p, T\right) = f\left(\varepsilon\right) = f\left[\varepsilon^p + \frac{\sigma_{ref}}{E} f_p\left(\varepsilon^p, \dot{\varepsilon}^p, T\right)\right] \tag{3.25}$$

The yield criteria is then given by

$$\sigma_e = \sigma = \sigma_{ref}\sqrt{f^2\left(\varepsilon^p, \dot{\varepsilon}^p, T\right) + l\eta} \tag{3.26}$$

Differentiating the square of Eq. (3.26) with respect to time gives the consistency condition

$$2\sigma_e\dot{\sigma}_e = 3\sigma'_{ij}\dot{\sigma}'_{ij} = \sigma_{ref}^2(2ff'\dot{\varepsilon}^p + l\dot{\eta}) \tag{3.27}$$

where

$$\dot{\eta} = \frac{1}{4\eta}\eta'_{ijk}\dot{\eta}'_{ijk} \tag{3.28}$$

$$\dot{\eta}'_{ijk} = \frac{1}{I_\varepsilon}\int_{Vcell}\left[\dot{\varepsilon}_{ik}\xi_j + \dot{\varepsilon}_{jk}\xi_i - \dot{\varepsilon}_{ij}\xi_k - \frac{1}{4}\left(\delta_{ik}\xi_j + \delta_{jk}\xi_i\right)\dot{\varepsilon}_{pp}\right]dV \tag{3.29}$$

$$\dot{\varepsilon}^p = \frac{6\mu\sigma'_{ij}\dot{\varepsilon}'_{ij} - \sigma^2_{ref}\,l\,\dot{\eta}}{2(3\mu\sigma_e + \sigma^2_{ref}\,ff')} \tag{3.30}$$

The constitutive equations of Taylor-based non-local theory of plasticity [84] are expressed in rate form as follows:

$$\dot{\sigma}_{kk} = 3k\dot{\varepsilon}_{kk} \tag{3.31}$$

$$\begin{aligned} \dot{\sigma}'_{ij} &= 2\mu\dot{\varepsilon}'_{ij} && \text{if } \sigma_e = \sigma \text{ and } \dot{\sigma}_e \geq 0 \\ &= 2G\left(\dot{\varepsilon}'_{ij} - \frac{3\sigma'_{ij}}{4\sigma_e}\frac{6\mu\sigma'_{ij}\varepsilon'_{ij} - \sigma^2_{ref}\,l\,\dot{\eta}}{2\left(3\mu\sigma_e + \sigma^2_{ref}\,ff'\right)}\right) && \text{if } \sigma_e < \sigma \text{ or } \dot{\sigma}_e < 0 \end{aligned} \tag{3.32}$$

The constitutive model is implemented using the user subroutine UMAT available in ABAQUS®/Standard. The measures of stress and strain used are the "true" (Cauchy) stress and logarithmic strain. In a finite strain problem the stress and strain tensor are rotated in an Updated Lagrangian formulation to account for rigid body motion.

3.2 Evaluation of Strain Gradient as Integral of Strains

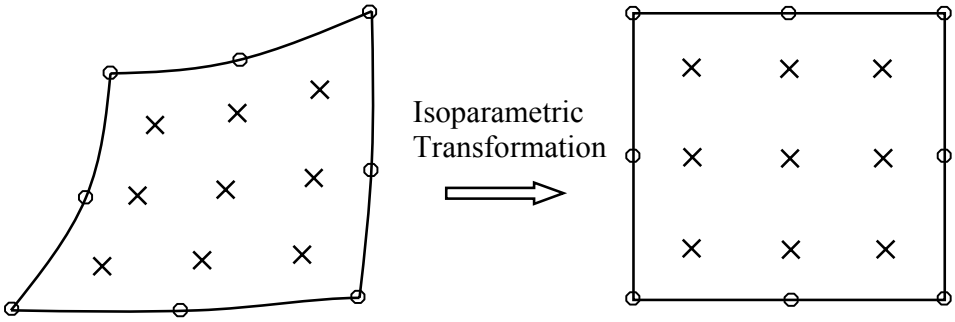

Figure 3.1. A schematic diagram of the isoparametric transformation.

In order to evaluate the strain gradient in an element, the strain components need to vary within the element. First order elements with linear shape functions generate constant strain and result in a zero strain gradient in the element. Thus, higher order elements (second order or higher) are required for full evaluation of the strain gradient within each element. The strain gradient evaluation algorithm used in this work is demonstrated for an 8-node quadratic element. For an 8 node bi-quadratic fully integrated element used in the model, each element has 9 Gaussian integration points as shown in Figure 3.1. The isoparametric transformation is used such that each element is converted to a square in the isoparametric space.

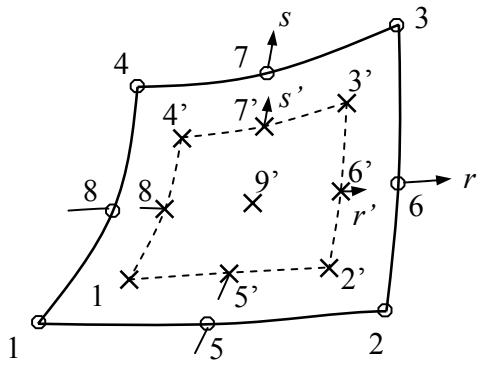

Figure 3.2. Extrapolation from an 8-node quad Gauss points.

The finite element solution of strains and stresses are obtained at the Gaussian integration points, which are identified as 1', 2', 3', 4', 5', 6', 7', 8' and 9' in Figure 3.2. To obtain the strain field within each element, the first step is to obtain the strain at the element nodal point. Each strain component is carried to the corner nodes 1 through 8 through a bi-quadratic extrapolation based on the strain values at 1' through 8'. To understand this extrapolation procedure more clearly, it is convenient to consider the region bounded by the Gauss points as an internal element or Gauss element. The Gauss element is also an 8-node quadrilateral. Its quadrilateral coordinates are denoted by *r'* and *s'*. These are linked to *r* and *s* by the simple relations

$$r = r' / \sqrt{\frac{5}{3}}, \qquad s = s' / \sqrt{\frac{5}{3}} \tag{3.33}$$

Table 3.1. Coordinate conversion between the quadrilateral element and its internal element.

Corner node	r	s	r'	s'	Gauss node	r	s	r'	s'
1	-1	-1	$-\sqrt{\frac{5}{3}}$	$-\sqrt{\frac{5}{3}}$	1’	$-\sqrt{\frac{3}{5}}$	$-\sqrt{\frac{3}{5}}$	-1	-1
2	1	-1	$\sqrt{\frac{5}{3}}$	$-\sqrt{\frac{5}{3}}$	2’	$\sqrt{\frac{3}{5}}$	$-\sqrt{\frac{3}{5}}$	1	-1
3	1	1	$\sqrt{\frac{5}{3}}$	$\sqrt{\frac{5}{3}}$	3’	$\sqrt{\frac{3}{5}}$	$\sqrt{\frac{3}{5}}$	1	1
4	-1	1	$-\sqrt{\frac{5}{3}}$	$\sqrt{\frac{5}{3}}$	4’	$-\sqrt{\frac{3}{5}}$	$\sqrt{\frac{3}{5}}$	-1	1
5	0	-1	0	$-\sqrt{\frac{5}{3}}$	5’	0	$-\sqrt{\frac{3}{5}}$	0	-1
6	1	0	$\sqrt{\frac{5}{3}}$	0	6’	$\sqrt{\frac{3}{5}}$	0	1	0
7	0	1	0	$\sqrt{\frac{5}{3}}$	7’	0	$\sqrt{\frac{3}{5}}$	0	1
8	-1	0	$-\sqrt{\frac{5}{3}}$	0	8’	$-\sqrt{\frac{3}{5}}$	0	-1	0

Any scalar quantity v whose values v'_i at the Gauss integration points are known can be interpolated using the bi-quadratic shape functions now expressed in terms of r' and s',

$$\nu(r',s') = \begin{bmatrix} \nu'_1 & \nu'_2 & \nu'_3 & \nu'_4 & \nu'_5 & \nu'_6 & \nu'_7 & \nu'_8 \end{bmatrix} \begin{bmatrix} N_1 \\ N_2 \\ N_3 \\ N_4 \\ N_5 \\ N_6 \\ N_7 \\ N_8 \end{bmatrix} \tag{3.34}$$

where N_1~N_8 are the shape functions of the quadrilateral element

$$N_1 = \frac{(1-r')(1-s')(-r'-s'-1)}{4} \tag{3.35}$$

$$N_2 = \frac{(1+r')(1-s')(r'-s'-1)}{4} \tag{3.36}$$

$$N_3 = \frac{(1+r')(1+s')(r'+s'-1)}{4} \tag{3.37}$$

$$N_4 = \frac{(1-r')(1+s')(-r'+s'-1)}{4} \tag{3.38}$$

$$N_5 = \frac{(1-r'^2)(1-s')}{2} \tag{3.39}$$

$$N_6 = \frac{(1+r')(1-s'^2)}{2} \tag{3.40}$$

$$N_7 = \frac{(1-r'^2)(1+s')}{2} \tag{3.41}$$

$$N_8 = \frac{(1-r')(1-s'^2)}{2} \tag{3.42}$$

Once the strains at the 8 nodal points are obtained, the strain at any specific point within the element can be calculated by interpolation using the shape functions. Next, a mesoscale cell centered at each element integration point as shown in Figure 3.3 is defined for the integration of the strain field. The mesoscale cell is taken to be a square surrounding the Gaussian integration points in the isoparametric space. The size of the mesoscale cell in the isoparametric space must be small such that it is completely contained in the element. Specifically, for an element size of 2 in the isoparametric space, the mesoscale cell size must be less than 0.45 for the element with nine-point Gaussian integration. A wide range of the mesoscale cell sizes, 0.4, 0.2, 0.02, and 0.002, has been used in the study. The differences in numerical results are shown to be less than 0.1%.

Therefore, 0.02 is used as the mesoscale cell size in the isoparametric space. It should be noted that there are two different levels of Gaussian integration in the finite element analysis for Taylor-based nonlocal theory. The first is at the element level, which is the same as in classical plasticity theories. Stresses and strains are evaluated at the Gaussian integration points in each element. The second is at the mesoscale cell level, which is special for Taylor-based nonlocal theory. There is a mesoscale cell surrounding each element-level Gaussian integration point.

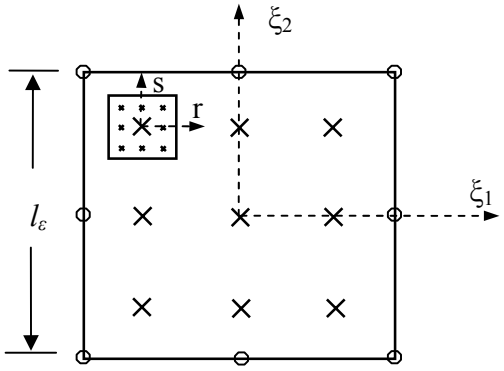

Figure 3.3. Mesoscale cell in an 8-node quadratic element.

For a two dimensional plane strain problem, the non-zero strain gradient component at each Gaussian integration point includes η'_{111}, η'_{121} (η'_{211}), η'_{221}, η'_{112}, η'_{122} (η'_{212}) and η'_{222}, which can be derived as follows,

$$\eta'_{111} = \frac{1}{I_\varepsilon}\int_{Acell}\left(\frac{1}{2}\varepsilon^r_{11}\xi_1 - \frac{1}{2}\varepsilon^r_{22}\xi_1\right)dA \tag{3.43}$$

$$\eta'_{121} = \eta'_{211} = \frac{1}{I_\varepsilon}\int_{Acell}\left(\frac{3}{4}\varepsilon^r_{11}\xi_2 - \frac{1}{4}\varepsilon^r_{22}\xi_2\right)dA \tag{3.44}$$

$$\eta'_{221} = \frac{1}{I_\varepsilon}\int_{Acell}\left(2\varepsilon^r_{21}\xi_2 - \varepsilon^r_{22}\xi_1\right)dA \tag{3.45}$$

$$\eta'_{112} = \frac{1}{I_\varepsilon}\int_{Acell}(2\varepsilon^r_{12}\xi_1 - \varepsilon^r_{11}\xi_2)dA \tag{3.46}$$

$$\eta'_{122} = \eta'_{212} = \frac{1}{I_\varepsilon}\int_{Acell}(\frac{3}{4}\varepsilon^r_{22}\xi_1 - \frac{1}{4}\varepsilon^r_{11}\xi_1)dA \tag{3.47}$$

$$\eta'_{222} = \frac{1}{I_\varepsilon}\int_{Acell}(\frac{1}{2}\varepsilon^r_{22}\xi_2 - \frac{1}{2}\varepsilon^r_{11}\xi_2)dA \tag{3.48}$$

The Gauss-Legendre integration scheme is used for the two dimensional integration in isoparametric space in Eq. (3.43) ~ Eq. (3.48). Note that all the strain components in Eq. (3.43) ~ Eq. (3.48) within the mesoscale cell is relative strain with respect to the center point of the mesoscale cell. Third order of Gauss-Legendre integration is adequate for accurate numerical integration (see Eq. 3.49) and its abscissae and weights are given in Table 3.2.

$$\int_{-1}^{1}\int_{-1}^{-1} f(\xi_1,\xi_2)d\xi_1 d\xi_2 = \sum_{i=1}^{k}\sum_{j=1}^{k} w_i w_j f(\xi_{1i},\xi_{2j}) \tag{3.49}$$

Table 3.2. Gauss-Legendre abscissae and weights.

No. k	$r_{k,}\, s_k$	weight w($r_{k,}\, s_k$)
2	$\pm\frac{\sqrt{3}}{3}$	1
3	0	$\frac{8}{9}$
	$\pm\sqrt{\frac{3}{5}}$	$\frac{5}{9}$

3.3 Tool-Chip Interaction

Two types of contact are involved in modeling of frictional interactions between the tool and the workpiece:

- Contact between the rake face of the tool and the chip.
- Contact between the flank face of the tool and the machined surface.

Accurate representation of the frictional interaction between the tool and workpiece is vital to obtaining a reliable and realistic machining simulation. This is because of the intimate link between machining forces and the tool-workpiece interaction as well as the thermo-mechanical coupled effect of the system due to heat generation by frictional dissipation. However, the friction characteristic at the tool-chip interface is difficult to determine since it is influenced by many factors such as cutting speed, contact pressure, and temperature. Extensive studies have been performed on the mechanics of interaction along the tool-chip interface and several models have been developed. Of these, Zorev's model [102], which reveals that two distinct regions of sliding and sticking on the interface exist, is widely accepted. In the sliding region, the shear stress is a fraction of the normal contact pressure, p. As the shear stress reaches a limiting shear stress value, τ^*, sticking occurs and the shear stress equals the limiting shear stress value regardless of the normal contact pressure. Plastic flow occurs in the sticking regime, whereas the same does not occur in the sliding regime. Further experimental work performed by Shirakashi and Usui [103] and Iwata et al.[37] revealed that a constant coefficient of friction was observed in the sliding regime, where the frictional shear stress was lower than a certain critical value, and a constant value of shear stress was observed in the sticking region. This critical value was found to be equal to the shear flow stress of

the work material. Also, Shaw [24] estimated that the critical value of contact pressure required for a rapid increase in the ratio of real area of contact to the apparent area of contact in a pin-on-disk experiment approached the flow stress of the material.

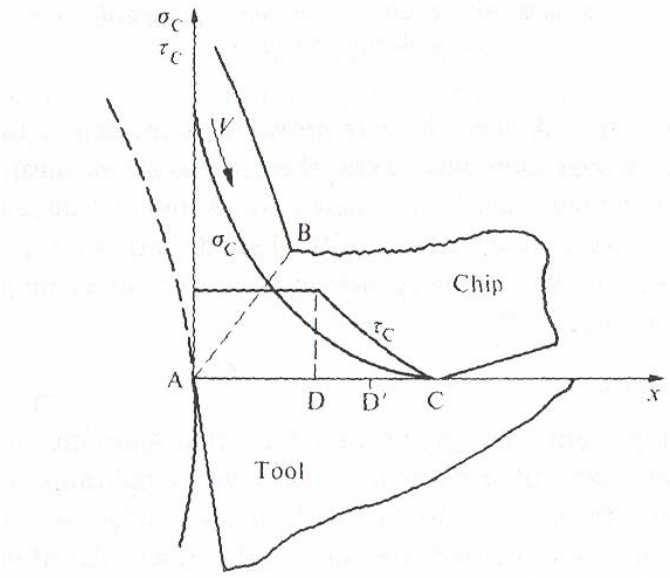

Figure 3.4. Illustration of normal and shear stress distribution at the tool chip interface [24].

The coefficient of friction for the sliding region may be estimated from pin-on-disc type experiments. Burwell and Strang [104] found that in order for subsurface plastic flow to take place in the weaker material when two materials are in contact, the value of the contact pressure equaled the shear flow stress of the material when the coefficient of friction approached 0.3.

For the aluminum alloy Al5083-H116 chosen as workpiece material in this work, very limited machining data has been reported since the material is more commonly used in bulk deformation process. Radwan [105] reported the mean coefficient of friction during machining of Al5083-H34 using high speed steel and sintered carbide tools to be 0.5~1.0. An average value of the coefficient of friction was estimated from the measured

frictional and normal forces in the experiments. However, the mean friction coefficient is expected to be less for machining Al5083-H116 with diamond tools.

Based on the above observations of the mechanics of interaction along the tool-chip and tool-work interfaces, the Coulomb friction model (see Eqs. (3.50)-(3.51)) seems to fit the machining problem most adequately. This model has been used with success by several researchers [39, 49, 106, and 107] and is chosen in this work to model the tool-chip interaction.

$$s = \mu\sigma \text{ when } \mu\sigma < \tau^* \text{(sliding)} \tag{3.50}$$

$$s = \tau^* \text{ when } \mu\sigma \geq \tau^* \text{(sticking)} \tag{3.51}$$

where s is the frictional shear stress,

μ is the coefficient of friction,

σ is the frictional normal stress, and

τ^* is the shear flow stress of the workpiece material and equals to $\sigma_y / \sqrt{3}$, σ_y is the uniaxial flow stress of the material in machining.

A sensitivity analysis for the coefficient of friction was run at a cutting speed (V_c) of 200 m/min, uncut chip thickness (t) of 0.2 mm and a width of cut of 1 mm. A value of 135 MPa, obtained from Equation (3.51), was used for τ^*. The cutting tool has a 5 degree rake angle. Finite Element simulations were run with coefficient of friction values of 0.3, 0.4 and 0.5. The cutting and thrust forces were compared with experimental values (see Page 91, 95 of Chapter 4 for details of the experiments). The results are shown in Table 3.3. It can be seen that friction coefficient at the tool-chip interface has a large influence on both cutting forces and thrust forces, with the forces showing a slight increase with increasing values of μ. The best prediction of the cutting force was obtained for μ=0.3

while the best prediction of the thrust force was obtained for μ=0.5. However, values of μ=0.3 under-predicted the thrust force and μ=0.5 over-predicted the cutting force respectively by significant amounts. A value of μ=0.4, which is closer to the apparent friction coefficient derived from experimental data (see Page 95 of Chapter 4), gives reasonable prediction within 20% percentage error for both cutting and thrust forces. Using a constant coefficient of friction, shear flow stress τ* was varied by ±10% to examine its effect on machining forces. It was found that variation of the shear flow stress has little effect on the machining forces.

Table 3.3. Friction coefficient sensitivity analysis.

Fric. Coeff. (μ)	F_c Sim. (N)	F_c Exp. (N)	F_t Sim. (N)	F_t Exp. (N)
0.3	136	133.4	26	54.1
0.4	150		43	
0.5	160		56	

3.4 Chip Separation Modeling

The pure deformation method of chip formation [49-50, 52] has been implemented in this work with the help of the adaptive remeshing technique. In the pure deformation method, the cutting process is likened to a metal forming operation. When the cutting tool advances, the material in front of the tool meets the tool and simply flow on the two sides of the tool. There is no need to debond any tied nodes or remove sacrificial elements to facilitate chip formation. Thus, a chip separation criterion can be avoided. Furthermore, there is no pre-defined parting line and therefore, the shape of the chip is not pre-determined. Instead, the material point, which is initially above the cutting

tool tip can be deformed and moved below the machined surface, which enables the modeling of subsurface material plastic flow. When cutting with a sharp tool, nodes in the workpiece move along the tool surface causing the elements to deform severely near the tool tip. The severely distorted elements usually cause convergence difficulties and should be replaced during the remeshing step by new elements that are more regular in shape. The small amount of material that overlaps the tool is removed during the remeshing step (see Figure 3.5).

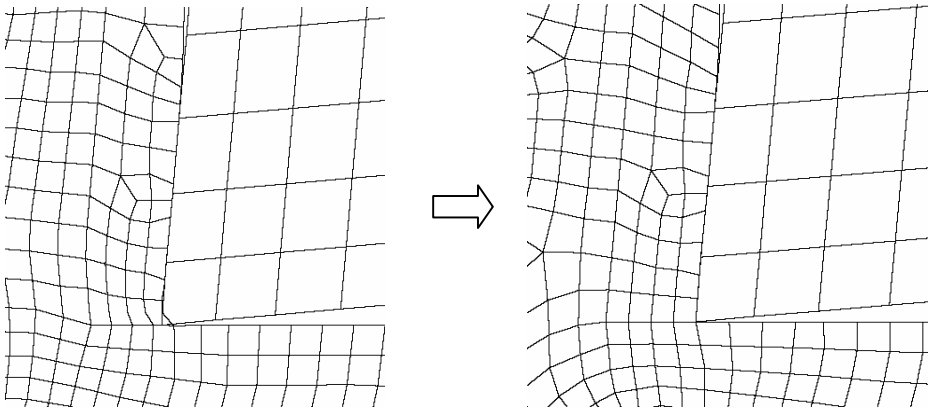

Figure 3.5. Illustration of material separation using the pure deformation method.

3.5 Heat Transfer Modeling

In applications such as machining, substantial amounts of heat may be generated due to plastic deformation and friction at the tool-chip interface. The temperature attained can be quite high and have a considerable influence on the mechanical properties of the material. In the finite element model, heat generation due to plastic deformation and friction is modeled as a volume heat flux. Heat conduction is assumed as the primary mode of heat transfer, which occurs within the workpiece material and at the tool-chip interface.

The governing equation of heat transfer is as follows:

$$\int_V \rho_m \dot{U} dV = \int_S q dS + \int_V \dot{Q} dV \tag{3.52}$$

where V is the volume of solid material with surface area S, $\dot{U}$ is the material time rate of internal thermal energy, ρ_m is the mass density, q is the heat flux per unit area of the body flowing into the body, and $\dot{Q}$ is the heat supplied externally into the body per unit volume.

The fraction of dissipated energy converted into heat due to plastic deformation and friction is assumed to be 0.9. Heat generated due to friction is distributed via a weighting factor of 0.5 between the two contact surfaces.

3.6 Finite Element Model Set-Up

There are many commercial finite element codes that are capable of modeling the machining process. Examples include DEFORM® 2D/3D, ABAQUS®, and Third Wave's AdvantEdge® Classic. Based on the modeling requirements noted above, the finite element package required for the present work must have the important feature of adaptive remeshing. A few of the aforementioned packages such as DEFORM®, AdvantEdge®, and MARC® 2D possess this feature. However, the program should also provide the user with the flexibility to define a genuine strain gradient plasticity material model using higher order elements. Higher order elements are necessary for fully evaluating the strain gradient tensor since constant strain components in first order elements yield zero strain gradients. Although ABAQUS®/Standard does not have true adaptive remeshing capability, it is more flexible than some of the other codes as it allows user-defined subroutines and higher order elements. Consequently, the general

FEA package ABAQUS®/Standard was selected as the finite element platform for this work.

A coupled temperature-displacement plane strain element is required for simulating the orthogonal metal cutting process. For a fully coupled simulation, ABAQUS® only allows fully integrated elements. However, as explained earlier, higher order elements are required for the evaluation of strain gradient at the element integration points. Therefore, an 8-node bi-quadratic displacement and bilinear temperature element was chosen to approximate the workpiece geometry.

In order to aid the initial progress of the simulation, the shape of the workpiece at the end close to the cutting tool was altered as shown in Figure 3.6 prior to the start of simulation. As can be seen in Figures 3.6-3.7, a step was created to aid the fast transition from incipient to steady stage. Since the steady state mechanical response is of primary interest, the initial shape modification will not affect the overall results obtained in the steady stage.

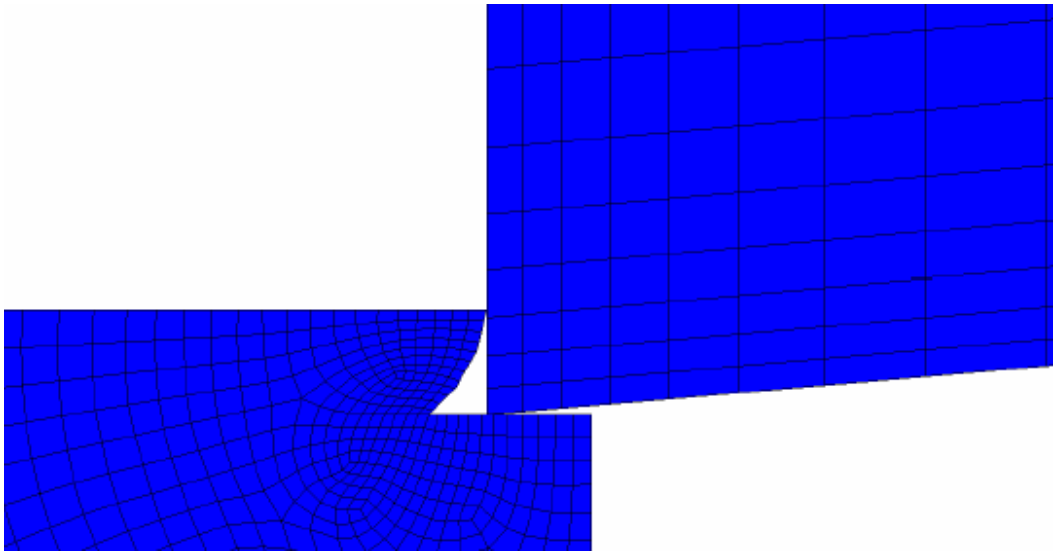

Figure 3.6. Region of workpiece showing modified initial shape for sharp tool.

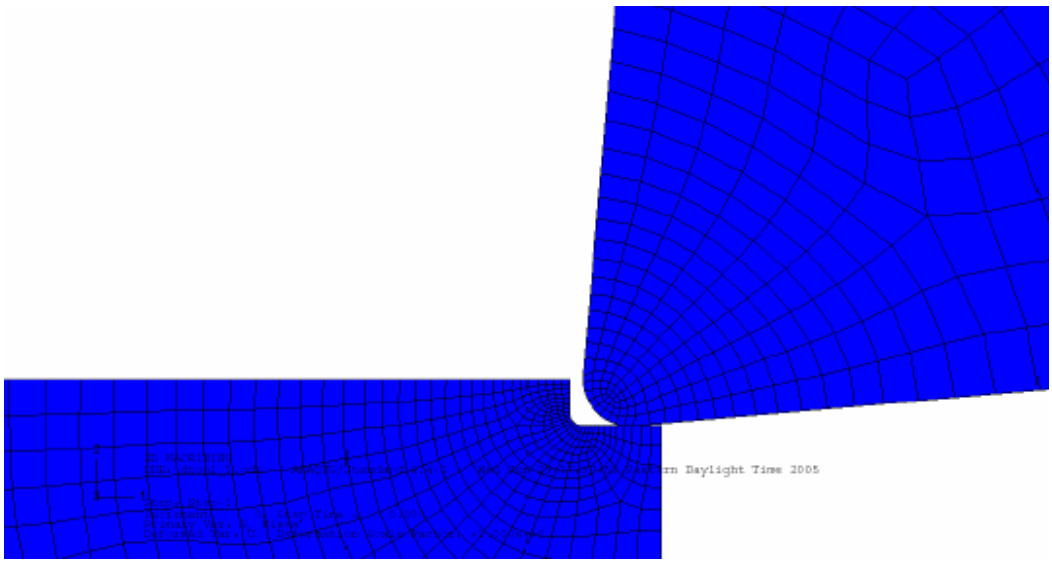

Figure 3.7. Region of workpiece showing modified initial shape for tool with a finite edge radius.

Since the overall dimensions of the model were significantly larger than the area of interest, mesh refinement was necessary to keep the total number of elements to a minimum for computational efficiency. It is necessary to have a very fine mesh in the primary and secondary deformation zones to resolve the relatively steep stress and strain gradients present in these zones. An element size of several microns is desired in these zones. However, using the same mesh size throughout the workpiece increases the computational cost significantly. Therefore, the mesh pattern generated in each remeshing step was designed to be much denser in the vicinity of the two deformation zones, and coarser away from these zones.

A mesh density windowing technique was used for mesh refinement. As seen in Figure 3.8, different mesh density windows were defined in and away from the major deformation zones. This approach reduces the number of elements by a factor of ten or

more and greatly reduces the computational cost while maintaining a sufficiently high resolution for the solution.

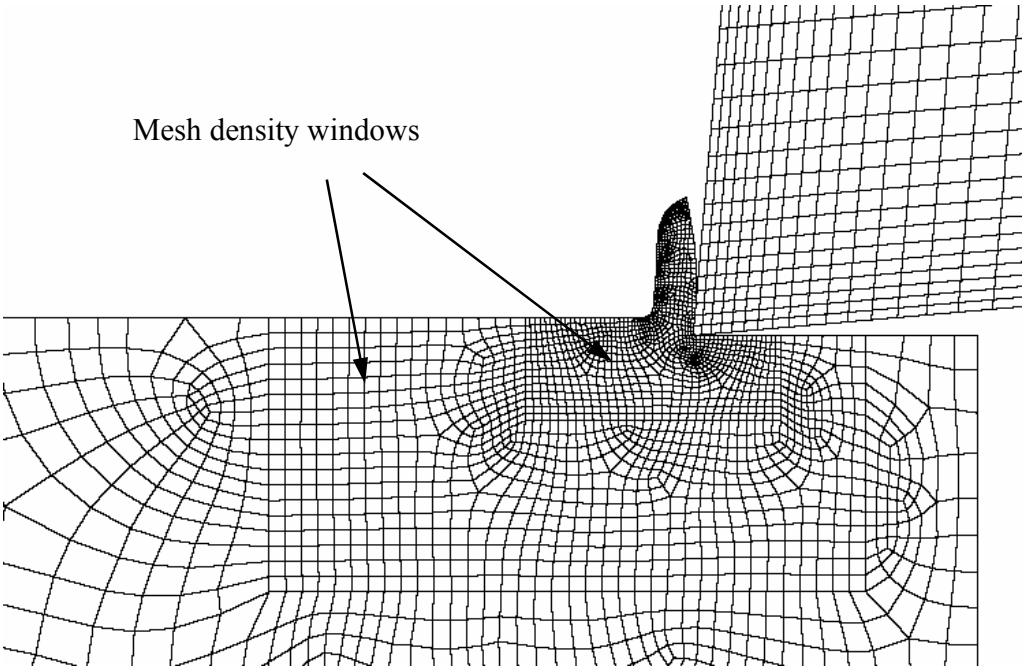

Figure 3.8. Illustration of mesh density windows in mesh refinement scheme.

The boundary conditions imposed on the model are shown in Figure 3.9. The nodes along the bottom side of the workpiece are constrained from movement in all directions. The nodes along the top and right side of the tool are constrained against movement in the y-direction. They are given a velocity in the x-direction equal to the cutting speed. An initial temperature of 25^{o}C was applied to all nodes in the model.

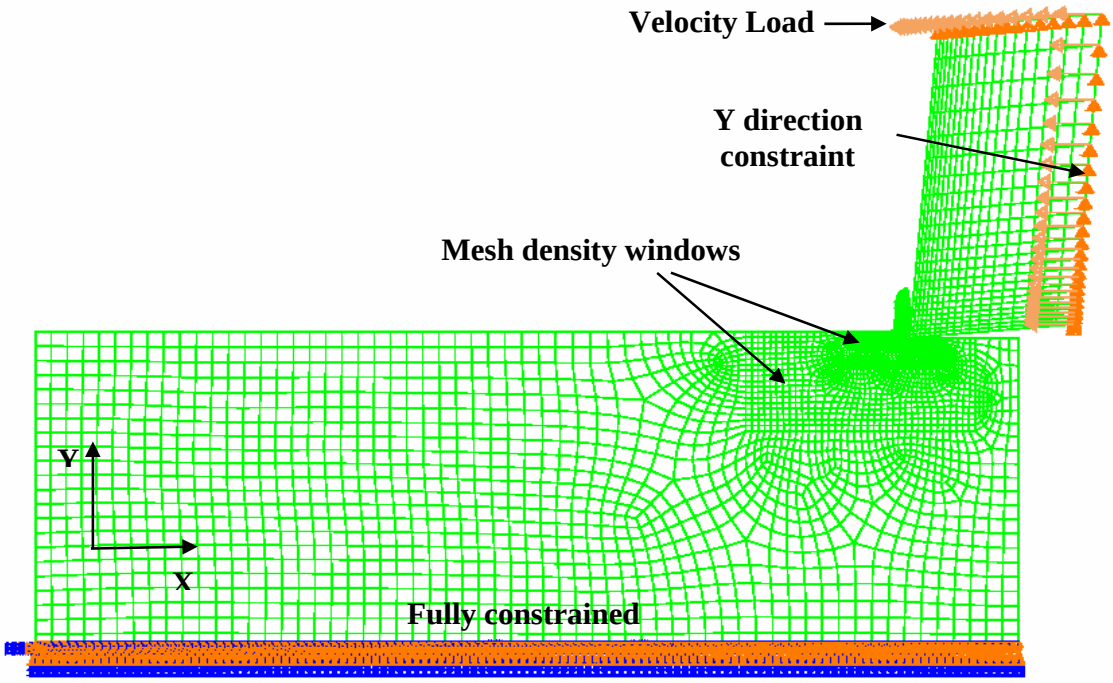

Figure 3.9. Illustration of boundary condition prescribed in finite element model.

Automatic time incrementation was used for the solution procedure. ABAQUS® determines a suitable time increment based on the model size and stiffness. Time increments during the solution procedure were found to be on the order of 10^{-9} seconds. Since the time integration step approaches zero, it may be concluded that the round-off and truncation errors are negligible.

A summary of physical properties of the workpiece and tool materials is presented in the next chapter. The workpiece was modeled as elasto-plastic, whereas the tool was modeled as rigid.

3.7 Overall Simulation Approach

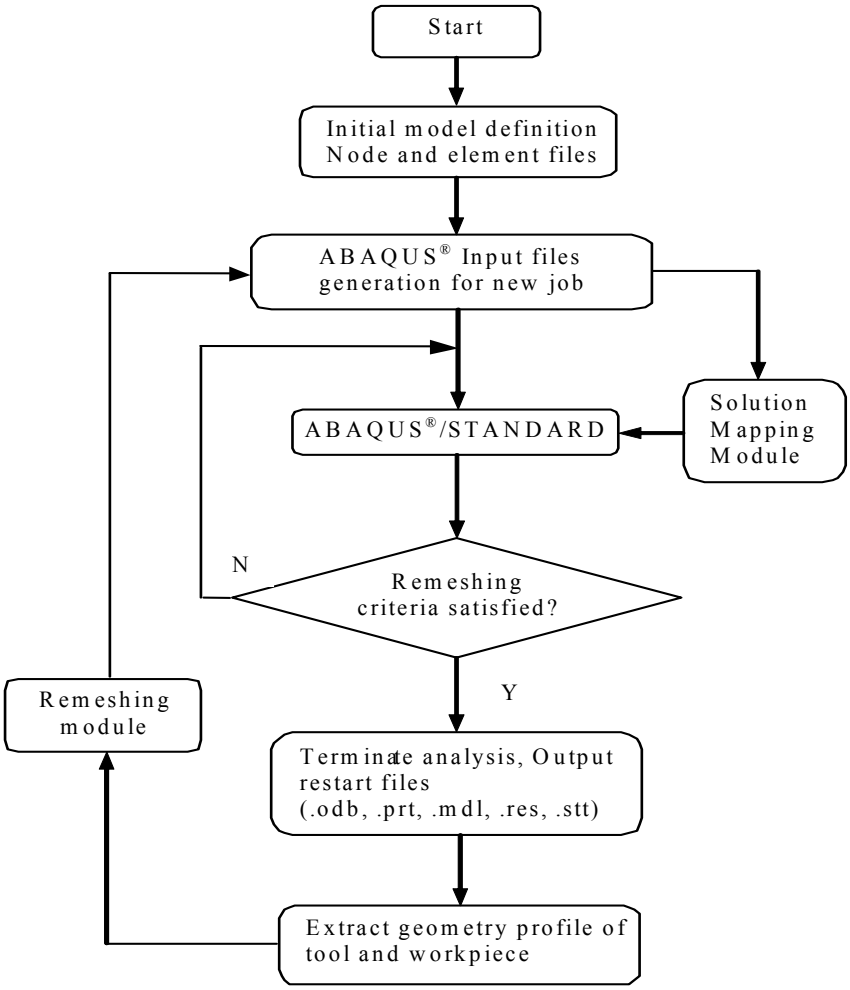

Figure 3.10. Overall simulation approach.

A flow chart summarizing the overall simulation approach is shown in Figure 3.10. Note that the complete simulation of one cutting pass consists of a large number of short analysis jobs. A DOS® script program is used to execute the loop without manual interruption. ABAQUS® starts the simulation with initial model definition, stress/strain calculation is executed using ABAQUS®/Standard and remeshing criteria is checked during each time increment. Once the remeshing criterion is met and a remeshing step is

considered to be necessary, the current simulation stops and outputs all the results. Then the geometry profile of the workpiece and tool is extracted from the results and submitted to the remeshing module to generate a new mesh. Next, the solution at the last step of the previous simulation job is mapped to the new simulation job as initial conditions. ABAQUS® then continues the cutting simulation by carrying out a new simulation subsequently. The strain gradient plasticity based constitutive model is realized by using the user defined subroutine URDFIL. Reading from and writing to the external database file is realized by using the user defined subroutine UEXTERNALDB. The solution mapping module is realized by using the ABAQUS® post-processing subroutine HKSMAIN. The remeshing module consisted of a pre-processor coded in FORTRAN 77 plus the automatic mesh generator feature of ANSYS®.

3.8 Hardware Details

Table 3.4 gives the details of the different machines the simulations were run on. Typical models with dimension of 3 mm by 1 mm and smallest element size of 2 μm have about 3000 elements and 12000 nodes. ABAQUS® is not a very RAM intensive program, with 1 GB being found more than adequate for common simulations. However, it should be noted that the simulations performed in this work consist of hundreds of small jobs, which requires high I/O capability of the system.

Table 3.4. Configurations of computer systems used to run simulations.

No.	Machine	Details
1	Dell Optiplex GX270	Intel Pentium IV processor @ 2.99 GHz Windows XP ™ OS 2 GB RAM
2	Dell Dimension 8200	Intel Pentium IV processor @ 2.53 GHz Windows XP ™ OS 1 GB RAM
3	Dell Dimension 4550	Intel Pentium IV processor @ 2.66 GHz Windows XP ™ OS 1 GB RAM
4	Dell Dimension 8200	Intel Pentium IV processor @ 2.20 GHz Windows XP ™ OS 1 GB RAM

3.9 Adaptive Remeshing

As discussed earlier, adaptive remeshing was implemented to avoid convergence difficulties typically caused by severely distorted elements. The adaptive remeshing module developed in this work differs from the "adaptive meshing" feature available in ABAQUS® in that it has the capability of adjusting, refining and/or coarsening the mesh.

Several remeshing criteria can be used to determine the best time to execute the remeshing step. During simulation, the remeshing criteria are checked at each time step to determine whether a remeshing step is required. Once the remeshing criterion is satisfied, the outline of the workpiece is stored and the automatic mesh generating module of ANSYS® is used to create a new mesh for this region. Subsequently, the solution is mapped from the old mesh to the new mesh. Several remeshing criteria such as interference depth, element shape, critical effective plastic strain, critical cutting distance and minimum time increment were investigated. Of these, interference depth,

critical cutting distance and minimum time increment were found to work the best for the simulations presented in this thesis. Details of these criteria are presented below.

3.9.1 Interference Depth

Interference depth is used as the main criteria in the sharp tool cutting simulation. ABAQUS®/Standard defines the contact conditions between two bodies using a strict "master-slave" algorithm. Generally, contact interactions occur between two surfaces. However, in the strict master-slave contact formulation used in ABAQUS®/Standard, only the master surface is used as a surface, where its geometry and orientation are taken into consideration. The direction of the slave surface's normal is not relevant in strict master-slave contact and a slave surface is recognized by the program as a group of nodes i.e. a node-based surface. The master surface that is attached to the sharp tool penetrates into the workpiece mesh at the tool tip as the tool advances. If too much penetration occurs, workpiece elements get badly distorted and make simulation results deviate from the correct solution. Also convergence issues arise with badly distorted elements. Therefore, interference depth is chosen as the remeshing criterion for the cutting simulation with sharp tool to prevent the workpiece elements near cutting tool tip from becoming severely distorted. This criterion was used for most sharp tool cutting simulations. Typical values of interference depth used varied from ¼ of the minimum element size to ¾ of the minimum element size.

3.9.2 Cutting Distance

In certain situations, element property based criteria do not work as nicely as expected. Then the remeshing step can be forced to occur by criteria such as cutting distance. When the cutting tool advances and exceeds certain critical distance, no matter

if the element shape is bad or not, or how much the maximum plastic strain is, a remeshing step is executed. This criterion was found to work well for the tool edge radius cases simulated and discussed in Chapter 5. A typical value used was two times of the minimum element size in the cutting zone.

3.9.3 Minimum Time Increment

The minimum time increment acts as an important supplemental remeshing criterion. By default, ABAQUS®/Standard automatically adjusts the size of the time increments to solve nonlinear problems efficiently. The user needs to suggest only the size of the first increment in each step of the simulation, after which ABAQUS®/Standard automatically adjusts the size of the increments. For highly nonlinear problems ABAQUS®/Standard has to reduce the increment size repeatedly to obtain a solution. The simulation usually fails to achieve convergence after too many cutbacks in the last time increment attempted. Therefore, when the time increment during one analysis is reduced to a certain value, the simulation is considered to need a remeshing step. This remeshing criterion was used in combination with the critical cutting distance criterion in the tool edge radius simulations presented in Chapter 5. Typical value of minimum time increment used in these simulations was $1x10^{-11}$ s, which is 1% of the initial time increment for the first step.

3.10 Solution Mapping Scheme

The solution and state variables need to be mapped from the old mesh to the newly created mesh after each remeshing step. Discontinuity in the solution is inevitable because of changes in the mesh. Therefore, it is important to keep the cumulative error under control so that it will not adversely affect the results after several hundred

remeshing steps. Remeshing before the elements become excessively distorted and using a sufficiently fine mesh tend to reduce the discontinuity. For a micro-cutting simulation, which needs as many as several hundred remeshing steps, the solution mapping scheme is found to be important and needs to be chosen carefully.

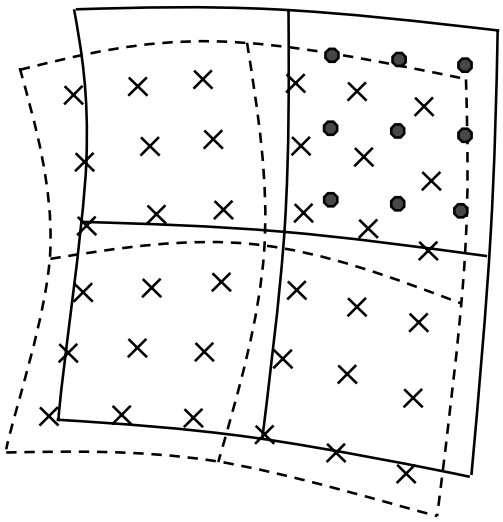

Figure 3.11. Illustration of ABAQUS solution mapping between old and new mesh.

ABAQUS®/Standard employs a standard interpolation technique for solution mapping. Basically, the solution variables are first obtained at the nodes of the old mesh by extrapolating the values from the gauss integration points to the element nodes and then averaging these values over all elements abutting each node. Next, the location of each integration point in the new mesh is obtained with respect to the old mesh and the variables are then interpolated from the nodes of the old element to the integration points of the new element (see Figure 3.11). However, this technique works well only with first–order reduced integration elements. Problems arise from the extrapolation step when used with higher order elements. If a new gauss integration point is located near the

nodes of the old mesh, the solution error at the new gauss point will tend to be magnified due to extrapolation of the solution variables to the nodes of the old mesh prior to interpolating them to the integration point in the new element. This magnification effect can eventually make the cumulative error grow out of bounds.

In the present work, the diffuse approximation method [108] was used to eliminate this error. Without extrapolating the solution to the nodes, a weighted least squares approximation is applied directly to a local window around the estimation points. The method is as follows.

At a given gauss integration point x of the new mesh, let $\sigma = <p(x, y)>\{\beta\}$ be the field to be estimated; $<p(x, y)>$ is the polynomial basis and $\{\beta\}$ is the coefficient vector depending on the coordinates (x, y). The coefficient vector $\{\beta\}$ is determined by minimizing the following function:

$$\sum_{i=1}^{N} w(x_i, y_i)(< p(x_i, y_i) > \{\beta\} - \sigma_i)^2 \tag{3.53}$$

where (x_i, y_i) and σ_i are the coordinates and the field values at the integration points of the old mesh, respectively. The approximation is based on the n closest neighbors of x (see Figure 3.12), and $w(x, y)$ is a weighting function centered at x and is given by,

$$w(x_i, y_i) = \exp\left(\frac{\ln(\lambda) \,||\, \bar{X}_i - \bar{X} \,||}{r(x)} \right) \tag{3.54}$$

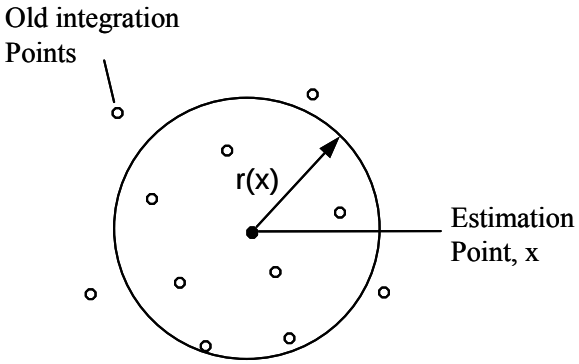

Figure 3.12. The diffuse approximation method.

By avoiding the extrapolation step and directly estimating based on the exact solution at the old integration points, the diffuse approximation method yields a more accurate mapping of the solution and minimizes the cumulative error.

The solution mapping scheme discussed above was coded in FORTRAN 77 and implemented as a post-processor in ABAQUS®/Standard thereby bypassing the default mapping routine available in the software.

3.11 Achieving Convergence

For an implicit algorithm, it is important to ensure convergence with reasonable time increments. In this section, some techniques that help in achieving convergence are described.

The ABAQUS® software used in the simulation checks the largest residual force and compares this to the average force within the model in order to test for convergence. This method is not appropriate for the metal cutting process, as the average force in the model is small compared to the maximal forces occurring in the shear zone. This standard convergence criterion is therefore much too strict. Convergence controls have to be

adjusted accordingly and comparison has to be made to a typical value of the force within the shear zone. The same applies for the calculation of temperatures and heat flows. It can be ensured that this convergence criterion is strict enough by comparing the calculated corrections to the calculated increments during the iteration procedure and ensuring their smallness.

Nonlinear static problems can be unstable due to change of the model due to remeshing. The instability is localized since only the new mesh within the cutting zone exhibits observable difference from the old mesh. After remeshing, the force equilibrium may not be fulfilled because of the mapping of the deformation and the material state variables. There will be a local transfer of strain energy from one part of the model to neighboring parts. This may cause initial deformations and thus lead to convergence problems that hinder the simulation restart. These kinds of problems have to be solved either dynamically or with the aid of artificial damping. ABAQUS®/Standard provides an automatic mechanism for stabilizing unstable quasi-static problems through the automatic addition of volume-proportional damping to the model. The mechanism is triggered by including the STABILIZE parameter in any nonlinear quasi-static procedure. Viscous forces of the form

$$F_v = C_d M^* v \tag{3.55}$$

are added to the global equilibrium equations

$$P_e - I_i - F_v = 0 \tag{3.56}$$

where M^* is an artificial mass matrix calculated with unity density, C_d is a damping factor, $v = \Delta u / \Delta t$ is the vector of nodal velocities, and Δt is the increment of time (which may or may not have a physical meaning in the context of the problem being solved).

In this work artificial damping has been introduced for the first $5x10^{-11}$ s of a simulation. This is a very short time period comparing to the whole time step so that this deformation is kept small. For most applications, the first increment of the step is stable without the need for damping. The damping factor is then determined in such a way that the extrapolated dissipated energy for the step is a small fraction of the extrapolated strain energy. The fraction is called the dissipated energy fraction and has a default value of 2.0×10^{-4}. However, for the case of restart analysis in machining, the first increment is unstable due to remeshing. In such cases it is not possible to obtain a solution to the first increment without applying some damping. Therefore, some damping is applied during the first increment. In many cases the amount of damping may not be appropriate and the damping factor used for the initial increment has to be chosen based on trial and error. The damping factor includes information not only about the amount of damping but also about mesh size and material behavior.

Another source of convergence difficulties comes from remeshing of a contact problem. In a region of contact the new mesh must conform closely to the shape of the surface from the old analysis. This requirement is especially important for problems involving contact between two deformable bodies. If the surfaces defined by the new mesh are even slightly different from the surfaces in the old analysis, the contact algorithms may fail to converge.

3.12 Summary

In this chapter, a fully coupled thermo-mechanical finite element model incorporating strain gradient plasticity has been established. A Taylor-based nonlocal theory of plasticity was used in constitutive model. Coulomb friction model was chosen to model the tool-chip interaction. Sensitivity of critical parameters such as the coefficient of friction and the shear flow stress at the tool-chip interface were studied. Values of these parameters were then chosen such that errors in the predicted forces were minimized. Pure deformation technique is used for modeling of chip separation. Adaptive meshing and diffuse approximation method based solution mapping techniques have been implemented to achieve reliable simulation.

CHAPTER 4

MICRO-CUTTING MODEL VERIFICATION

The previous chapter established a strain gradient based thermal-mechanical coupled finite element model that is aimed at accurately representing the constitutive behavior of a metallic material in micro/meso scale cutting. In this chapter the proposed finite element model is verified by comparing the predicted cutting forces with measured forces obtained from a series of machining experiments. Two sets of orthogonal cutting experiments, at high and low cutting speeds, have been carried out on aluminum alloy Al5083-H116, a strain rate insensitive material. A detailed description of the machines, cutting tools, workpiece materials, experimental setup and the experimental procedure is presented in this chapter.

4.1 Experimental Goal

The goal of the experiments discussed in this chapter is to verify that the established finite element model for micro/meso scale cutting process is able to provide good predictions of the cutting forces. It is known that at the current stage, there is lack of reliable and robust techniques for measuring the cutting variables such as cutting temperature, shear strains within deformation zone, etc. However, cutting force measurement can be obtained with fairly good resolution and repeatability and is therefore chosen as the variable for verification purposes. To demonstrate the capability of the established finite element model at different cutting conditions, one set of orthogonal cutting experiments was performed at low cutting speed and small uncut chip

thickness where the strain gradient effect is expected to be dominant. Another set of orthogonal cutting experiments was performed at high cutting speed and relative large uncut chip thickness where the strain gradient effect is expected to be negligible. Due to variation in the edge radius of the cutting tool and convergence difficulties encountered when incorporating strain rate into the material constitutive model, edge radius and strain rate effects are minimized in the model verification by choosing an upsharp tool and a strain rate insensitive material AL5083-H116.

4.2 High Precision Machines

It has been highlighted by many researchers that one of the major disparities between macro-scale and micro scale machining is the positional accuracy and resolution requirement of the machines used. Further, miniaturization of engineering components is often limited by the accuracy and resolution of the machine tool's actuation and sensor systems. However, recent technical developments in ultra-precision machines have significantly improved both the achievable accuracy and resolution of the machines. Therefore, to ensure the precise position and movement of cutting tools with respect to the workpiece in this experimental investigation, a Hardinge conquest T42SP lathe and a precision 2-axis motion control stage with excellent positioning and repetition accuracy were used. Detailed descriptions of the high precision machines used in this experimental investigation are presented in the following section.

4.2.1 Hardinge Conquest T42SP Lathe

The Hardinge Conquest T42SP lathe, shown in Figure 4.1, is a 2-axis super precision Computer Numerical Control (CNC) lathe. The machine has a positioning

resolution of 1 μm in the X and Z axes and an overall axis repeatability of 0.76 μm. The minimum axial feed rate of the Hardinge lathe is 1 mm/min. It utilizes heavy duty linear guideways for improved positioning accuracy. The machine is also mounted on a 2200 kg HARCRETE® polymer composite base for increased vibration isolation. The Hardinge Conquest T42SP lathe was used in this study for orthogonal cutting experiments on Al5083-H116 with Polycrystalline Diamond (PCD) tools at relative high cutting speeds (≥200 m/min) and large uncut chip thickness values (≥20 μm).

Figure 4.1. Hardinge Conquest T42SP Lathe.

4.2.2 Precision 2-Axis Motion Control Stage

The precision 2-axis motion control stage consists of two Aerotech ATS125 linear ball screw stages. The ATS125 with integral motor option directly couples a brushless motor to the ballscrew drive. This eliminates the flexible coupling typically present in screw driven stages and yields a stiffer system with higher servo bandwidth. The lack of a coupling also improves system reliability by removing a component susceptible to failure. The control stage has a maximum travel length of 600 mm and maximum speed of 36 m/min. The resolution of the precision 2-axis motion control stage is within 0.1 μm. For

a maximum travel distance of 100 mm, its accuracy is within 6 μm and straightness and flatness are within 5 μm. The precision 2-axis motion control stage, as shown in Figure 4.2, was used in this study for orthogonal cutting experiments on Al5083-H116 with single crystal diamonds (SCD) tools at low cutting speeds (≤ 10m/min) and small uncut chip thicknesses (≤ 10μm).

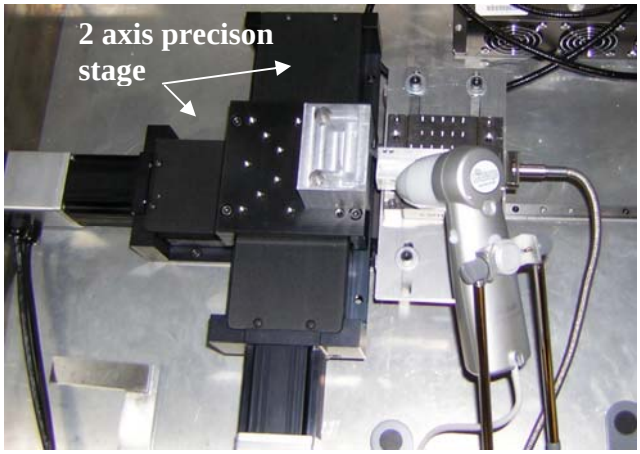

Figure 4.2. Precision 2-axis motion control stage.

4.2.3 ZYGO NewView 200 White Light Interferometer

The ZYGO NewView 200, shown in Figure 4.3, is a scanning white-light interferometer used for characterization of the surface texture. It is a high-resolution, non-contact, non-destructive, three-dimensional surface measurement device. It is typically used for surface characterization of silicon wafers, automotive parts and machined components. This device utilizes the pairing of a highly precise vertical scanning transducer and a camera to generate a three-dimensional surface image of the sample. This is achieved by using the fringes produced by the optical path difference between the reference and reflected beam. The image of the surface is subsequently processed to

provide a precise measurement of the surface topography of the sample. The ZYGO NewView 200 was used to measure the surface roughness of the machined samples.

Figure 4.3. ZYGO NewView 200 white light interferometer.

4.2.4 Cutting Force Dynamometers

A three-component piezoelectric cutting force dynamometer was used to measure the cutting forces in this study. Since the magnitude of the cutting forces in micro and nano scale cutting is expected to be small, an important requirement of the dynamometer used is that it should have a low threshold and high sensitivity so that it can accurately measure small fluctuations in the cutting forces. Two types of force dynamometers were used in the experimental investigation.

A Kistler Type 9256C2 three-component force mini-dynamometer, shown in Figure 4.4, was used to measure the cutting forces in the micro scale cutting experiments. The type 9256C2 mini-dynamometer allows measurement of three extremely small orthogonal components of force due to its high sensitivity and low threshold (< 0.002 N). It can accurately measure force components as small as 0.001 N and has a working range of ±250 N.

A Kistler Type 9257 three-component force dynamometer, shown in Figure 4.5, was used to measure the cutting forces in experiments where the uncut chip thickness exceeded 10 μm. The Type 9257 dynamometer can measure force components as small as 0.01 N with a working range of ±5 kN.

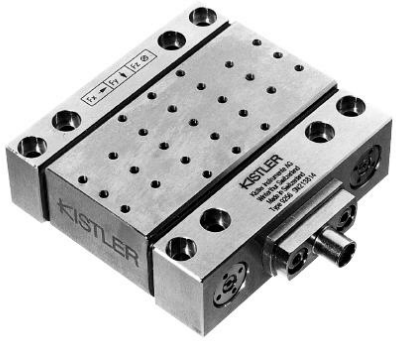

Figure 4.4. Kistler Type 9256C2, three-component force mini-dynamometer.

Figure 4.5. Kistler Type 9257, three-component force dynamometer.

4.3 Workpiece Material

AL5083-H116 is an Al-Mg-Mn alloy developed for applications requiring a weldable moderate strength alloy having good corrosion resistance. As such it is an excellent all round alloy ideal for many applications. Superplasticity of Al5083-H116 allows economical forming of complex components while retaining the high strength- and stiffness-to-weight ratios characteristic of aluminum alloys used in automotive, aerospace and military applications. As a non-heat-treatable alloy, microstructural damage incurred in the Heat affected zone (HAZ) in welding for Al5083-H116 is limited to recovery, recrystallization and grain growth. Thus, loss in strength in the HAZ is not nearly as severe as that experienced in heat-treatable alloys. For this reason, Al5083-H116 alloy is popular for use in welded pressure vessels where reasonable joint strengths can be obtained in the as-welded condition without the need for post-weld heat treatment. Al5083-H116 allows a good compromise between formability and corrosion resistance, combined with moderate strength. Typical applications include automotive, rail, architectural and marine applications.

According to a recent sensitivity study of material flow stress in machining by Fang [109], the predominant factor governing the material flow stress is either strain hardening or thermal softening, depending on the specific work material employed and the varying range of temperatures. Strain-rate hardening is reported as the least important factor governing the material flow stress, especially when machining aluminum alloys. It is also reported in [110] that aluminum alloy is one category of metal that possesses the smallest strain rate sensitivity exponent. Among aluminum alloys, Al5083-H116 is observed to have negative strain rate sensitivity at room temperature. Al5083-H116 has

been found to have the least strain rate sensitivity exponent based on available material data. Therefore, in this study, aluminum alloy Al5083-H116, a rate insensitive material with small strain rate hardening exponent [111, 112], is chosen as the workpiece material. The chemical composition of Al5083-H116 is given in Table 4.1.

Table 4.1. Nominal chemical composition of Al5083-H116 [113].

Component	**Weight (%)**
Al	92.4 – 95.6
Cr	0.05 – 0.25
Cu	Max 0.1
Fe	Max 0.4
Mg	4 – 4.9
Mn	0.4 – 1
Other, each	Max 0.05
Other, total	Max 0.15
Si	Max 0.4
Ti	Max 0.15
Zn	Max 0.25

4.4 Cutting Tools

The primary objective of this experimental work is to perform mechanical micro-cutting of Al5083-H116 at small uncut chip thicknesses. As highlighted in an earlier section, it is well known that the edge radius of the cutting tool, shown in Figure 4.6, greatly influences various aspects of the cutting process (e.g. cutting forces, chip formation process, surface finish and power consumption) at the micro and nano scale.

Furthermore, the minimum thickness of cutting attainable is also known to be influenced by the sharpness of the cutting edge [114].

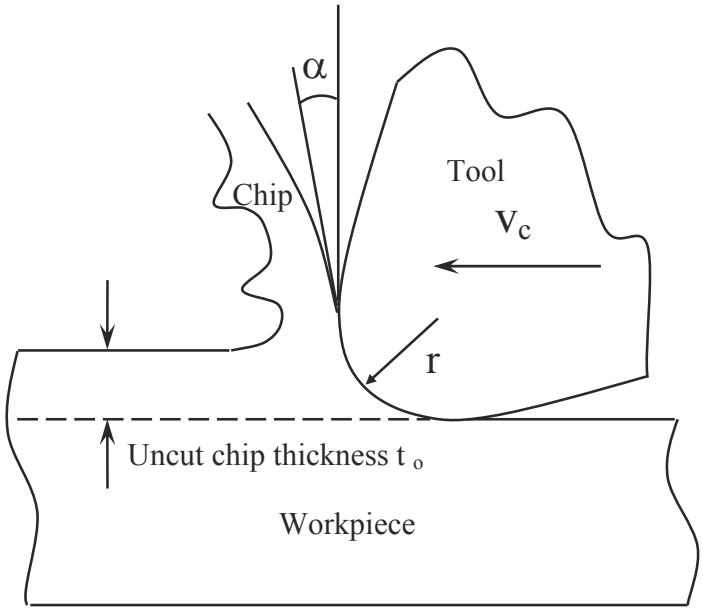

Figure 4.6. Schematic of cutting edge radius of cutting tool.

However, due to lack of control over the edge radius of the cutting tool from the commercial tool supplier, using a cutting tool with the sharpest available cutting edge radius would effectively eliminate the edge radius effect until the cutting edge radius of the tool is of the same order of magnitude as the uncut chip thickness. In addition, a sharp tool would allow micro and nano scale cutting to be conducted at very small uncut chip thicknesses while producing continuous chips. Therefore, the main selection criterion of the cutting tool is to minimize the cutting edge radius.

4.4.1 Single Crystal Diamond Tool

Single crystal diamonds (SCD) are the hardest known material. In addition, SCD tools have the sharpest cutting edge radius currently available. Therefore, SCD tools are commonly used in micro and nano scale cutting of non-ferrous materials.

SCD tools used in this study are made from natural diamond. Each SCD tool has a cutting edge width of 2 mm, a rake angle of 0˚ and a clearance angle of 5˚. An included angle of 85˚ provides strength to the cutting edge. The cutting edge radius of the SCD tools was measured and estimated to be approximately in the range of 65 nm to 100 nm. This was accomplished by fitting a circle on a highly magnified SEM image of the tool's cutting edge. An example of the SEM image used to estimate the cutting edge radius of the tool is shown in Figure 4.7.

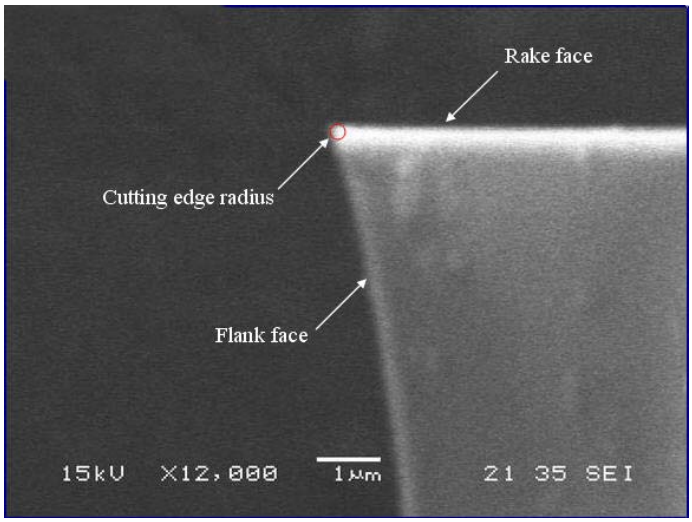

Figure 4.7. SEM image of SCD tool [115].

4.4.2 Polycrystalline Diamond Tool

Polycrystalline diamonds (PCD) tools are designed to machine non-ferrous and non-metallic materials at high speeds. They have proved that they can outperform many

ordinary tools in production applications. Tools with Polycrystalline Diamond blanks are made by brazing PCD blanks to steel shanks, then grinding the tool point to its final configuration with diamond wheels. PCD blank tools are replacing tools made with single crystal natural diamond, particularly where impact is high due to interrupted cuts. Significant performance increases are seen over the life of several tools because the properties of PCD blank tools are much more consistent then natural diamond tools. Also, natural diamond tools are much more susceptible to accidental impact damage.

The sharpness of the PCD tool cutting edge used in this work is determined by the grinding process and usually is not as good as the SCD tools. In this study, PCD tool inserts NGP-3189L, Grade KD100 from Kennametal Inc. is used and trace analysis of the PCD tool edge gives a radius that is less than 7 μm.

4.5 Experimental Setup

A face turning (end turning of a tube) dry cutting operation simulating the orthogonal cutting process was conducted on the Hardinge Conquest T42SP lathe. A plane shaping dry cutting operation was conducted on the Precision 2-axis motion control stage. Since the two machines had different fixturing requirements, two different experimental setups were used. Both setups were designed to reduce the overhang of both the tool and workpiece in order to maintain the rigidity of the tool and workpiece. The design thus eliminated potential sources of errors caused by the deflection and vibration of the workpiece during the cutting experiments.

4.5.1 Setup on the Hardinge Conquest T42SP Lathe

The Hardinge Conquest T42SP lathe is built with a collet chuck, hence the workpiece, which was pre-machined to the form of tube can be directly mounted onto the lathe. The workpiece was held rigidly by the collet and its overhang was minimized. Light cuts were made with up-sharp turning tools to reduce the outer diameter of the workpiece to 38.1 mm. This ensured that the center axis of the workpiece was along the axis of rotation of the work spindle to minimize runout. The workpiece was subsequently bored internally to a diameter of 36.1 mm to form a tube of 1 mm wall thickness. The Kistler Type 9257 dynamometer was mounted onto the turret of the machine with the tool being subsequently mounted on the dynamometer. The configuration of the experimental setup in the Hardinge Conquest T42SP lathe is shown in Figure 4.8. The Hardinge Conquest T42SP lathe was used for orthogonal cutting experiments on Al5083-H116 with Polycrystalline Diamond (PCD) tools at relative high cutting speeds (≥200 m/min) and large uncut chip thickness values (≥20 μm).

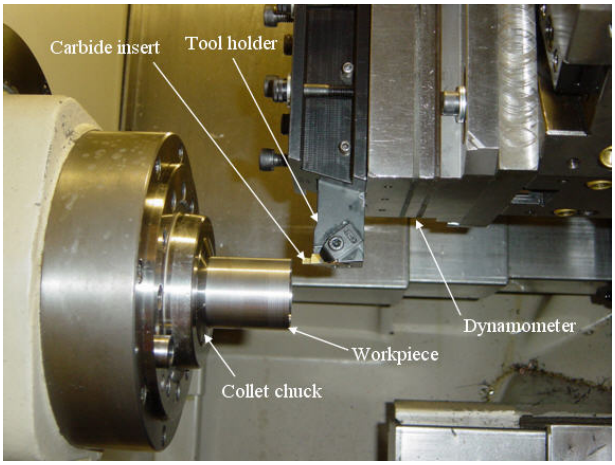

Figure 4.8. Schematic of orthogonal cutting experiment carried out on Hardinge lathe.

4.5.2 Setup on the Precision 2-Axis Motion Control Stage

A precision 2-axis motion control stage (Aerotech ATS-125) was used. The workpiece was designed to be of cubic shape with a 1mm wide, 2 mm height ridge on one outer surface. The workpiece was fixed to the 2-axis stage and translated in the X and Y directions (see Figure 4.9). The SCD tool was mounted on a mini three component piezoelectric force dynamometer (Kistler Minidyne® 9256C2), which was fixed on a supporting stage. All components of the setup were mounted on an aluminum base plate and the entire setup was placed on a vibration isolation table. The depth of cut was imparted by moving the workpiece along the Y-axis and the cutting velocity was imparted by moving the workpiece along the X-axis. The precision 2-axis motion control stage was used for orthogonal cutting experiments on Al5083-H116 with single crystal diamonds (SCD) tools at low cutting speeds (≤ 10m/min) and small uncut chip thicknesses (≤ 10μm).

A schematic drawing of the relative position of workpiece and the tool are provided in Figure 4.9.

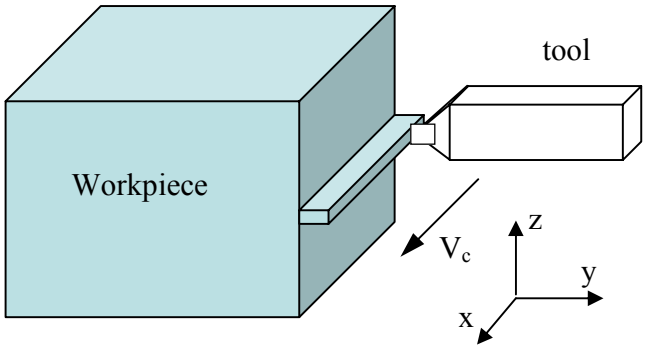

Figure 4.9. Schematic of orthogonal micro-cutting carried out on a precision 2-axis motion control stage.

4.6 Experiment Design and Procedure

As stated earlier, the size effect in micro-cutting can arise from various factors such as the cutting temperature, strain rate and strain gradient. To verity the material strengthening due to strain gradient effects with decrease in uncut chip thickness, it is desirable to design the experimental conditions such that the effect of strain gradient is highlighted while the other effects are minimized. One more set of experiments is designed to be conducted under conditions where the strain gradient effect becomes negligible while other factors such as temperature in the secondary shear zone take over the dominant role of causing size effect.

In order to minimize the edge radius effect, a single crystal diamond (SCD) tool and a polycrystalline diamond (PCD) tool with upsharp cutting edge were chosen. Scanning Electron Microscope (SEM) measurements of the cutting edge of the SCD tool shown in Figure 4.7 yields a radius of 65~100 nm. Trace analysis of PCD tool edge (Kennametal NGP-3189L, KD100) gives a radius that is less than 7 μm. Since the edge radius is less than 10% of the smallest uncut chip thickness used in the experiments with each tool, the tool edge radius influence is assumed to be negligible.

The range of values for the cutting speed and uncut chip thickness were chosen as follows. At higher cutting speeds, a larger drop in cutting temperature is expected as the uncut chip thickness is decreased. A rough calculation based on Oxley's method [116] shows that the temperature rise at a cutting speed of 10 m/min produces a negligible effect on the flow stress, while the temperature rise at a cutting speed of 200 m/min is large enough to have a considerable effect on the material flow stress. Further, as can be seen from Eq. (3.3), the strain gradient strengthening effect is prominent only when the

size of the inhomogeneous plastic flow, given by the uncut chip thickness in micro-cutting, is comparable to the intrinsic material characteristic length, which for aluminum alloy Al5083-H116 is about 5.7 μm (calculated using Eq. (4) and α=0.3, G=26.4GPa, σ_{ref}=228 MPa, b=0.256nm). Hence, the strain gradient effect becomes significant when the uncut chip thickness is of the order of a few microns.

Orthogonal cutting experiments were therefore conducted at two cutting speeds: 10 m/min and 200 m/min. At a cutting speed of 10 m/min, the uncut chip thickness was varied between 0.5 μm and 10 μm, a range where the strain gradient effect is expected to be dominant. At a cutting speed of 200 m/min, the uncut chip thickness was varied between 20 and 200 μm in order to highlight material strengthening due to a decrease in the secondary shear zone temperature with uncut chip thickness.

Orthogonal cutting experiments at the cutting speed of 200 m/min were performed on the Hardinge T42SP super precision lathe with the PCD tool. The workpiece was in the form of tube of 1 mm wall thickness (see Figure 4.6). Cutting forces were measured with a piezoelectric force dynamometer (Kistler dynamometer® 9257B). Three replications of the cutting tests were performed for each uncut chip thickness value. The tool was examined under the microscope before and after each cutting experiment to see if it had undergone any changes. Smearing of material on cutting tool was found to be negligible at a cutting speed of 200 m/min. The tool was subsequently used to conduct replications of the experiment. The force data collected in subsequent cutting experiments show good agreement with previous replications. This indicates that the cutting tool was not worn nor adversely affected by the smearing of the work material on it.

Due to the 1 mm/min minimum axial feed rate limit of the Hardinge lathe, orthogonal cutting tests at the cutting speed of 10 m/min could not be performed on this lathe for uncut chip thickness values ranging from 0.5 μm to 10 μm. Therefore, the set of experiments at low cutting speed and small uncut chip thickness were performed on the precision 2-axis motion control stage (Aerotech ATS-125). A workpiece with a 1 mm wide ridge was fixed to the 2-axis stage and translated in the X and Y directions (see Figure 4.9). The SCD tool was mounted on a mini three component piezoelectric force dynamometer (Kistler Minidyne® 9256C2). Figure 4.10 shows the image of the SCD tool during cutting of Al5083-H116 at 10 m/min. First, the workpiece was brought close to the cutting edge of the SCD tool carefully for initial engagement. A ramp section was created at the beginning of the ridge to facilitate a smooth transition from transient to steady state cutting. Five replications of the cutting test were performed at each uncut chip thickness value. Again, the tool was examined under a microscope before and after each cutting experiment and the force data collected in subsequent cutting tests was compared with the previous replications. The force data showed good repeatability throughout the cutting experiments.

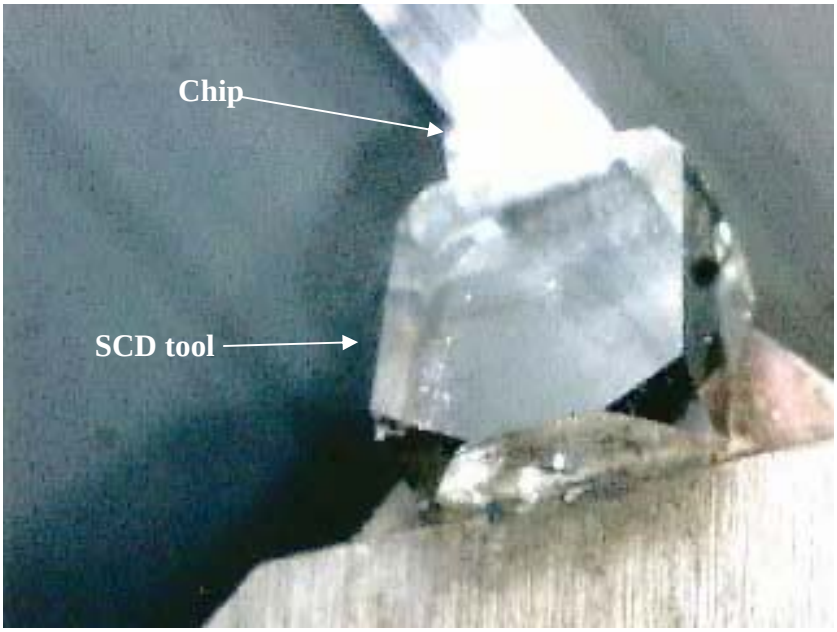

Figure 4.10. Orthogonal cutting of Al5083-H116 with SCD tool at 10 m/min.

Tables 4.2 and 4.3 summarize the orthogonal cutting experimental conditions used for studying the strain gradient and temperature effects, respectively.

Table 4.2. Experimental conditions highlighting the strain gradient effect.

Machine Tool	Precision 2-axis motion control stage (Aerotech ATS-125)
Cutting Speed (m/min)	10
Uncut Chip Thickness (μm)	0.5, 1, 2, 5, 7.5, 10
Cutting tool	SCD tool 0^0 rake, 5^0 clearance edge radius 65~100 nm
Workpiece material	Al5083-H116
Dynamometer	Kistler Minidyne® 9256C2

Table 4.3. Experimental conditions highlighting the temperature effect.

Machine Tool	Hardinge T42SP
Cutting Speed (m/min)	200
Uncut Chip Thickness (μm)	20, 50, 75, 100, 150, 200
Cutting tool	PCD tool 5^0 rake, 11^0 clearance edge radius 7 μm
Workpiece material	Al5083-H116
Dynamometer	Kistler 9257B

4.7 Model Verification

Orthogonal cutting simulations were run with the full model, which includes strain, strain gradient and temperature effects, to validate the model predictions against the experimental data at the two cutting speeds for the two sets of uncut chip thickness. Flow stress data for Al5083-H116, derived from a hot torsion test, has been reported by Zhou and Clode [117]. The magnitude of the plastic strain in micro-cutting is found to fall within the range of strain of the flow stress data. Although the flow stress data for Al5083-H116 from the hot torsion test is obtained at a strain rate of 18.04 and temperature range from 350^oC~550^oC, it is assumed that the plastic behavior of Al5083-H116 during cutting can still be correctly represented since the strain rate dependence of the flow stress for Al5083-H116 is negligible. A modified Johnson-Cook flow stress equation Eq. (4.1) was used to fit the flow stress data of Zhou and Clode reproduced in Figure 4.11 with a zero strain rate hardening exponent. The coefficients of the modified Johnson-Cook model are listed in Table 4.4 and were used to obtain the finite element simulation results presented in the paper.

There is little machining data in the literature for Al5083-H116 that could be used as a guide for determining the frictional interaction between the diamond tool and the chip. Therefore, in this study, the mean apparent friction coefficient derived from Eq. (4.2) is used in the Coulomb friction model presented earlier in Eqs. (3.50-3.51). A friction coefficient of 0.21 was used in the Coulomb friction model for the frictional interaction between the PCD tool and the Al5083-H116 at 200 m/min cutting speed. A friction coefficient of 0.14 was used to represent the frictional interaction between the SCD tool and the Al5083-H116 at 10 m/min cutting speed. Material properties of Al5083-H116 and the diamond tools are given in Table 4.5 and 4.6, respectively.

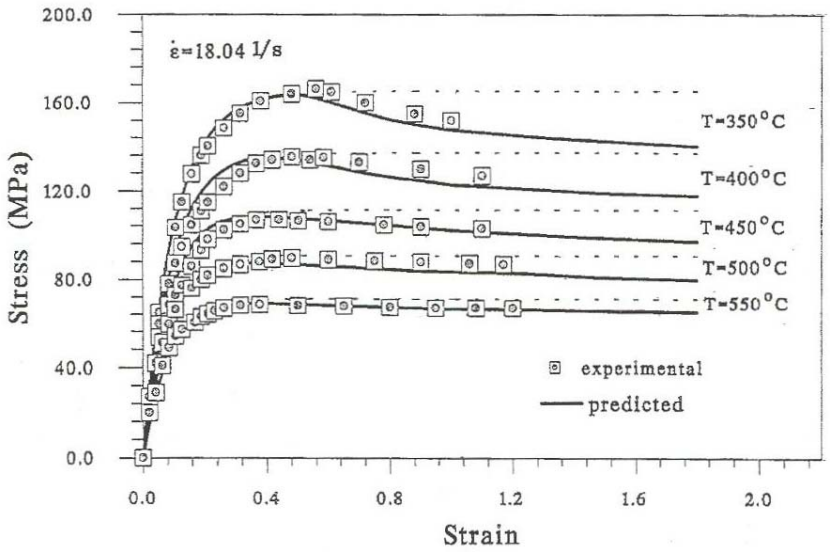

Figure 4.11. Flow stress data for Al5083-H116 [110].

$$f\left(\varepsilon,\dot{\varepsilon},T\right)=(A+B\varepsilon^{n})(1+\dot{\varepsilon})^{c}\left(1-\left(\frac{T-T_{o}}{T_{m}-T_{o}}\right)^{m}\right) \tag{4.1}$$

$$\mu=\frac{F_{t}+F_{c}\tan\alpha}{F_{c}-F_{t}\tan\alpha} \tag{4.2}$$

Table 4.4. Modified Johnson-Cook flow stress model coefficients for Al5083-H116.

A (MPa)	*B* (MPa)	*n*	*c*	*m*
167	300	0.12	0	0.89

Table 4.5. Material properties of Al5083-H116.

Density (Kg/m^3)	2660
Specific heat (J/kg °C)	900
Thermal conductivity (W/m K)	117
Coefficient of thermal expansion (μm/m °C)	12.6
Melting temperature (°C)	591~638
Yield strength (MPa)	228
Young's modulus (GPa)	71
Shear modulus (GPa)	26.4
Poisson's ratio	0.33

Table 4.6. Material properties of diamond tools [106].

Density (Kg/m^3)	3500
Specific heat (J/kg °C)	471.5
Thermal conductivity (W/m k)	1500
Coefficient of thermal expansion (μm/m °C)	2.0
Melting temperature (°C)	4027
Young's modulus (GPa)	850
Poisson's ratio	0.1

Table 4.7. Cutting force data at 200 m/min.

Uncut chip thickness (µm)	Cutting force, F_c (N)	Thrust force, F_t (N)	F_c Standard deviation (N)	F_t Standard deviation (N)
20	21.38	11.40	1.56	0.99
50	39.47	15.48	0.10	0.50
75	53.11	19.79	0.94	1.01
100	67.24	25.67	1.74	0.69
150	103.98	45.98	1.93	3.21
200	133.40	54.11	4.40	1.23

Table 4.8. Comparison of measured and predicted cutting forces at 200 m/min (all forces in N/mm width of cut).

Uncut chip thickness (µm)	Cutting speed (m/min)	Cutting force, F_c Exp. (N)	Cutting force, F_c Sim. (N)	Error	Thrust force, F_t Exp. (N)	Thrust force, F_t Sim. (N)	Error
20	200	21.4	19.5	-8.78%	11.4	5	-56.15%
50	200	39.5	40	1.34%	15.5	12.5	-19.23%
75	200	53.1	55	3.56%	19.8	18	-9.04%
100	200	67.2	73	8.57%	25.7	23	-10.40%
150	200	104.0	105	0.98%	46.0	35	-23.88%
200	200	133.4	130	-2.55%	54.1	43	-20.54%
		Absolute avg. error		4.25%	Absolute avg. error		23.21%

Force data obtained from the cutting experiments performed on the Hardinge Lathe at a cutting speed of 200 m/min is reported in Table 4.7. The good repeatability of the cutting force data proved that the cutting edge of the PCD tool was not significantly influenced by tool wear or smearing during cutting. The comparison between experimental and simulated cutting forces at 200 m/min from 20 µm uncut chip thickness to 200 µm uncut chip thickness is given in Table 4.8. The comparison is also presented in the plot shown in Figure 4.12. It can be seen that reasonably good agreement between the simulated results and measured forces is obtained. The maximum percentage error in the cutting force prediction is -8.78% and the absolute average percentage error is 4.25%.

The comparison of the measured and predicted thrust forces comparison is found to be not as good as for the cutting force. The maximum percentage error is -56.15% and the absolute average percentage error is 23.21%. It is also observed that the maximum percentage error in the thrust force prediction occurs at the smallest uncut chip thickness value.

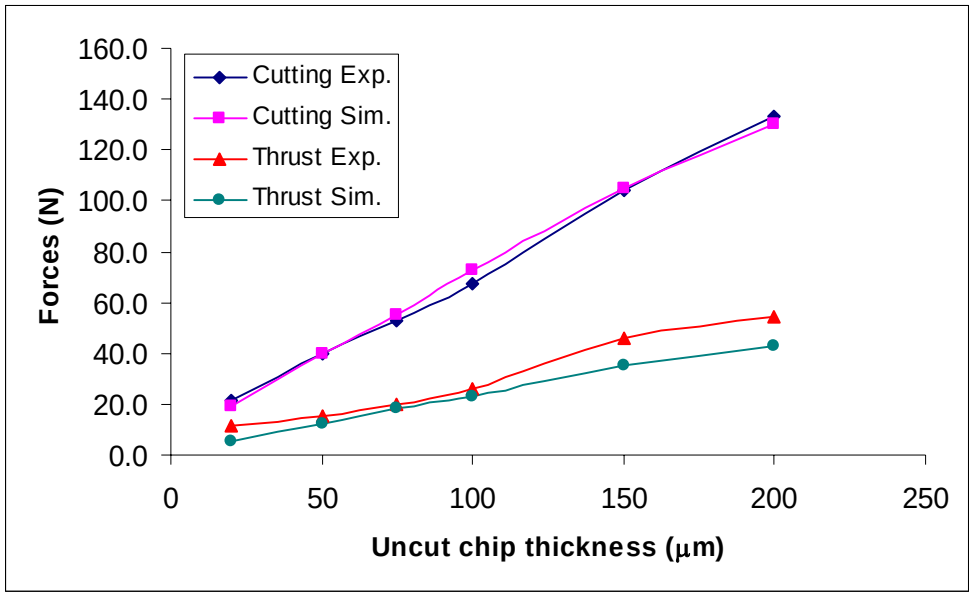

Figure 4.12. Comparison of measured and predicted cutting forces at 200 m/min.

Table 4.9. Cutting force data at 10 m/min.

Uncut chip thickness (μm)	**Cutting force, F_c (N)**	**Thrust force, F_t (N)**	**F_c Standard deviation (N)**	**F_t Standard deviation (N)**
0.5	0.97	0.37	0.10	0.06
1	1.45	0.40	0.18	0.03
2	2.47	0.45	0.27	0.08
5	5.31	1.05	0.13	0.09
7.5	7.71	1.56	0.10	0.07
10	9.77	1.90	0.15	0.06

Table 4.10. Comparison of measured and predicted cutting forces at 10 m/min (all forces in N/mm width of cut).

Uncut chip thickness (μm)	**Cutting speed (m/min)**	**Cutting force, F_c Exp. (N)**	**Cutting force, F_c Sim. (N)**	**Error**	**Thrust force, F_t Exp. (N)**	**Thrust force, F_t Sim. (N)**	**Error**
0.5	10	0.97	0.95	-2.14%	0.37	0.10	-72.93%
1	10	1.45	1.75	20.57%	0.40	0.25	-37.93%
2	10	2.47	3.00	21.61%	0.45	0.50	11.71%
5	10	5.31	5.80	9.20%	1.05	1.05	0.44%
7.5	10	7.71	7.95	3.14%	1.56	1.45	-7.03%
10	10	9.77	9.86	0.93%	1.90	1.84	-3.20%
		Absolute avg. error		9.6%	Absolute avg. error		22.2%

The cutting force data obtained from cutting experiments on the precision 2-axis motion control stage at a cutting speed of 10 m/min are reported in Table 4.9. Again, good repeatability of the force data shows that the cutting edge of the SCD tool was not significantly affected by tool wear or smearing during cutting. The comparison between the measured and simulated cutting forces at 10 m/min from 0.5 μm uncut chip thickness to 10 μm uncut chip thickness is given in Table 4.10. The comparison is also presented in the plot shown in Figure 4.13. It can be seen that better agreement is obtained for the cutting force. The maximum percentage error in the predicted cutting force is 21.61% and the absolute average percentage error is 9.6%. The thrust forces comparison is found to be not as good as for the cutting force. The maximum percentage error in the thrust force prediction is -72.93% and the absolute average percentage error is 22.2%. Similarly, it is observed that the maximum percentage error in the thrust force prediction occurs at the smallest uncut chip thickness value.

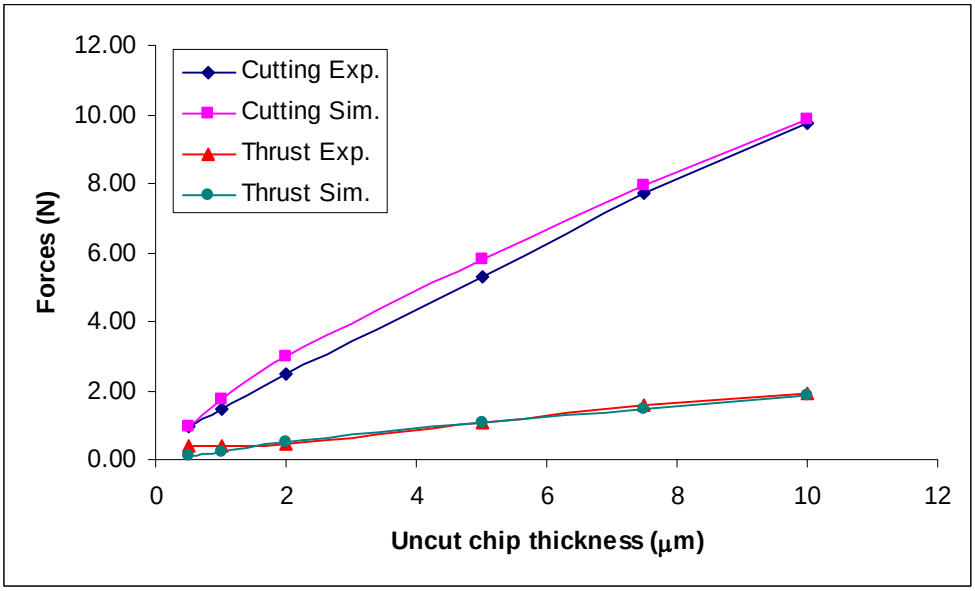

Figure 4.13. Comparison of measured and predicted cutting forces at 10 m/min.

As seen from Figures 4.12 and 4.13, the strain gradient based finite element model developed in this study gives reasonable predictions of the cutting and thrust forces at both cutting speeds. The sources of error in the force predictions could be due to the flow stress data at the machining condition not being accurately represented and the simple constant friction model applied at the tool-chip interface. It is noticed that for both cutting speeds the simulated thrust forces are mostly under predicted compared to the measured thrust forces and that the percentage error increases when the uncut chip thickness is decreased. This could be caused by the use of a constant friction coefficient for the whole range of uncut chip thickness examined whereas the friction coefficient estimated from the measured forces shows an increasing trend with decrease in uncut chip thickness. Nevertheless, the model gives reasonable predictions in terms of the absolute error. In particular, the model yields good predictions of the cutting force component, which is necessary for the size effect analysis. Thus, the finite element model

is considered to be satisfactorily validated and is used in the following section to analyze the contribution of each material strengthening factor to the size effect in micro-cutting.

4.8 Summary

This chapter presented the experimental design and procedure employed in the micro-cutting model verification experiments. The technical specifications of the equipment used, selection of cutting tools, workpiece material and experimental setup were described in detail. Simulated forces from the established strain gradient based thermal-mechanical finite element model were compared to the measured force data. An absolute average percentage error of 4.25% for cutting force and an average percentage error of 23.21% for thrust force are obtained at a cutting speed of 200 m/min. An absolute average percentage error of 9.6% for cutting force and an absolute average percentage error of 22.2% for thrust force are obtained for orthogonal cutting tests at a cutting speed of 10 m/min. Thus, the established finite element model is considered to be satisfactorily validated and able to accurately represent the constitutive behavior of the Al5083-H116 alloy in micro scale cutting. The model is used in the following chapter to analyze the contribution of each material strengthening factor to the size effect in micro-cutting.

CHAPTER 5

SIZE EFFECT ANALYSIS

The previous chapter dealt with the verification of a thermo-mechanical finite element model for simulating orthogonal micro cutting. The next step in analyzing the micro-cutting process is to apply the model developed in Chapter 3 and verified in Chapter 4 to quantitatively study the contribution of strain gradient strengthening as well as other material strengthening mechanisms to size effect. Three main factors, namely the strain gradient effect, temperature effect and edge radius effect are analyzed in this chapter. The temperature effect refers to the apparent increase in material strength associated with a decrease in cutting temperature due to a reduction in the uncut chip thickness. Their relative contribution to the size effect in specific cutting energy under certain conditions and domain of applicability are identified. In addition, the material length scales associated with the starting point of the nonlinearity in specific cutting energy are discussed.

5.1 Material Strengthening Mechanisms in Micro-Cutting

It is known that the flow stress of a metal is affected by strain, strain rate and temperature. Recent experimental evidence in micro/nano indentation also shows strain gradient dependence of flow stress at micron/submircon level length scales [19-23]. Experimental observations of size effect reveal that the nonlinearity in specific cutting energy is likely an intrinsic material behavior. A recent sensitivity study of material flow stress in machining by Fang [109] shows that strain-rate hardening is the least important

factor governing the material flow stress, especially when machining aluminum alloys. In this chapter, the aluminum alloy Al5083-H116, a rate insensitive material with a small strain rate hardening exponent [111-112], is chosen as the workpiece material to minimize strain rate effects. Therefore, the effects of strain gradient, temperature and edge radius on size effect are studied in this chapter. The workpiece and tool material properties used in the simulation presented in this chapter are the same as given in chapter 4 (see Tables 4.4-4.6). The tool geometry and frictional condition used in the simulations run at cutting speeds of 200 m/min and 10 m/min are also set to be the same as the corresponding cases presented in Chapter 4 (see Table 4.2-4.3 and page 88).

5.2 Effect of Strain Gradient

It was stated earlier that the material strength is strongly influenced by the strain gradient at micron/submicron level length scales. In micro-cutting, the material strength in the primary and secondary shear zones can be significantly affected by the intense strain gradient within the highly localized deformation zones. Therefore, the magnitude and distribution of strain gradient within the deformation zones are examined first. Then, their effect on the distribution of effective plastic strain, effective stress and temperature are studied by comparing the results of finite element simulations with and without strain gradient. Specifically, the effect of strain gradient strengthening on specific cutting energy is analyzed.

5.2.1 Strain Gradient Distribution in Deformation Zones

Figure 5.1 shows the effective strain gradient distribution obtained from the finite element simulation at 10 μm uncut chip thickness and 10 m/min cutting speed. It is found

that very high strain gradients are present in the chip at the tool-chip interface and in the workpiece surface layers. As expected, a high strain gradient band is also present in the primary deformation zone. Analysis of the simulation results shows that the normal plastic strain components ε_{11} and ε_{22} (shown in Figures 5.2 and 5.3) contribute to the strain gradient in the primary deformation zone and secondary deformation zone at the tool-chip interface, while the high strain gradient in the surface layers comes mainly from the distribution of shear plastic strain ε_{12} (shown in Figure 5.4). With an effective strain gradient of several hundred and a calculated material length scale of 5.7 μm (calculated using Eq. (4) and α=0.3, G=26.4GPa, σ_{ref}=228 MPa, b=0.256nm), it can be seen that the term associated with the strain gradient in Eq. (3.3) is significant compared to the other term. Consequently, the strain gradient strengthening effect is considerable. This also suggests that the effect will become even more dominant at smaller uncut chip thickness, which will produce an even steeper strain gradient.

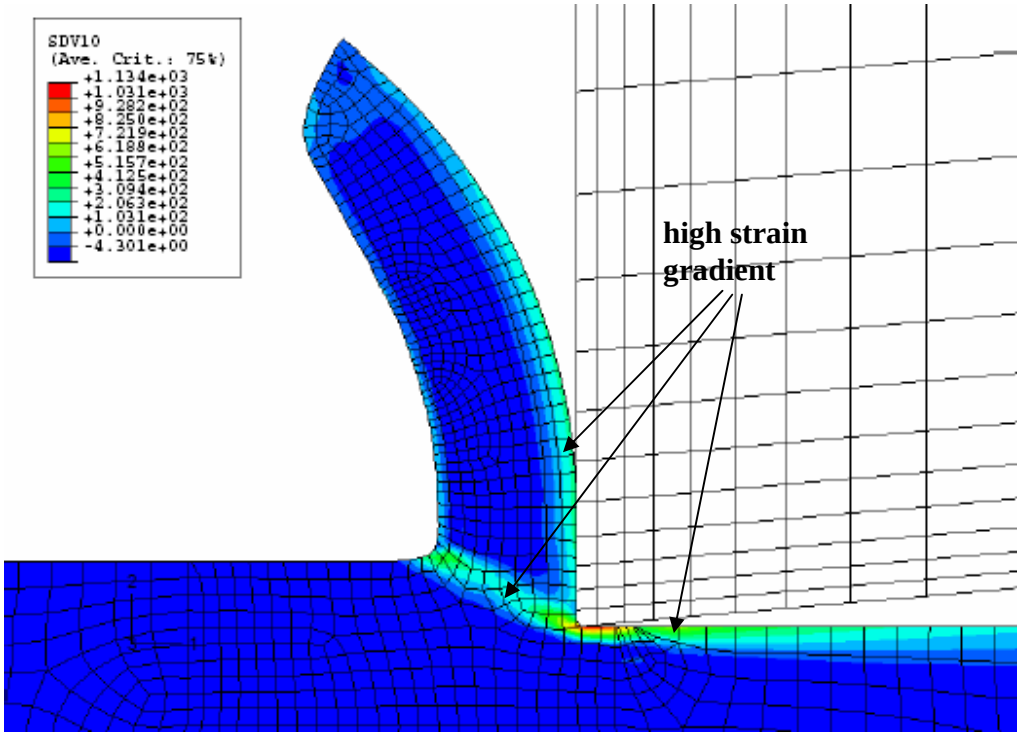

Figure 5.1. Effective strain gradient contour (10 μm uncut chip thickness, 10 m/min cutting speed).

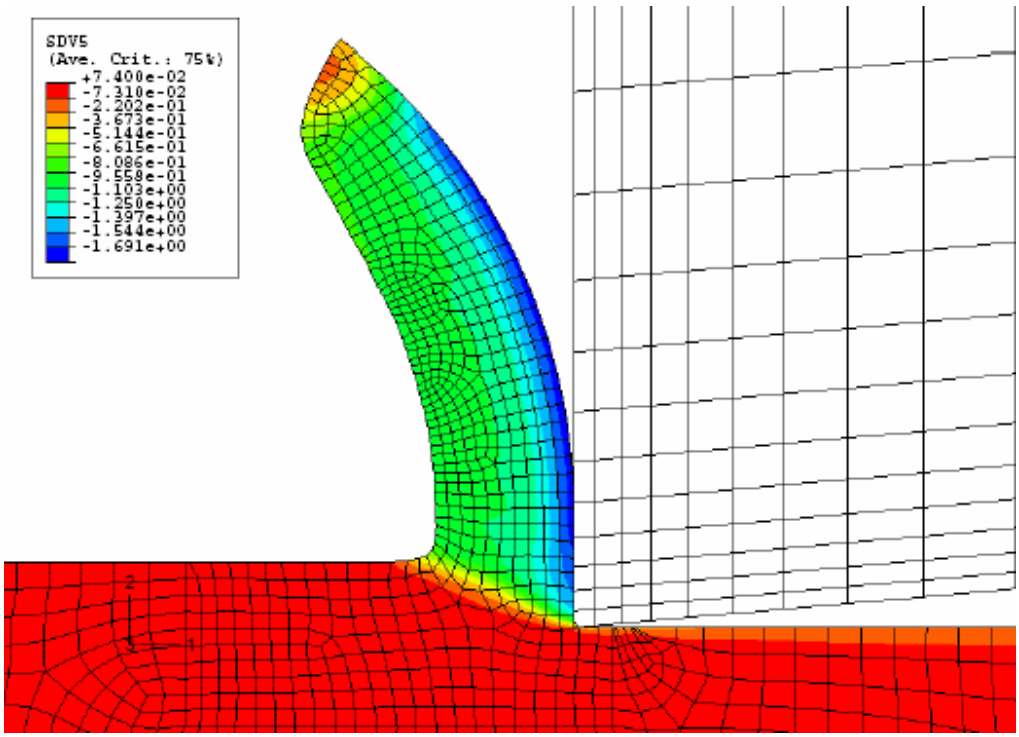

Figure 5.2. Plastic strain component ε_{11} contour.

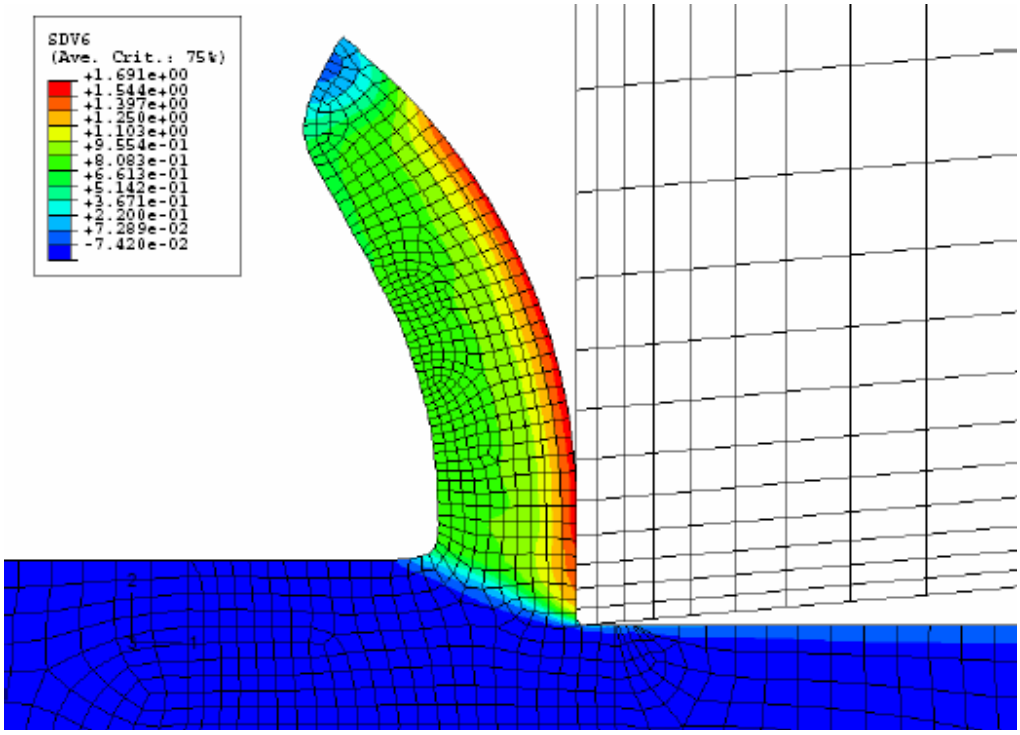

Figure 5.3. Plastic strain component ε_{22} contour.

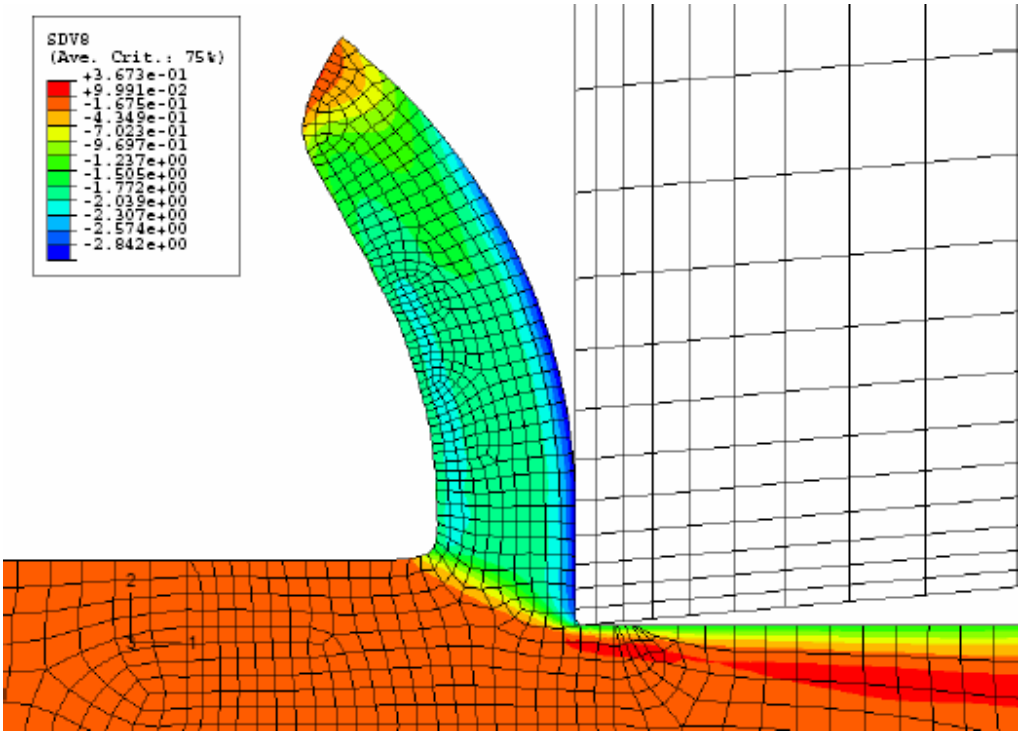

Figure 5.4. Plastic strain component ε_{12} contour.

5.2.2 Effects of Strain Gradient Strengthening on the Distribution of Effective Plastic Strain, Effective Stress and Temperature

In order to examine the effect of strain gradient on the distribution of effective plastic strain, effective stress and temperature, a comparison between the finite element model based on conventional plasticity and the finite element model with strain gradient plasticity is presented in Figures. 5.5-5.10 for the 2 μm uncut chip thickness and 240 m/min cutting speed case. It is evident from the figures that all contour plots of the same variable in both cases exhibit a similar overall pattern. Examination of the chip shape suggests that it is easier for the chip to curl in the absence of strain gradient strengthening than in the presence of strain gradient strengthening.

It can be seen from Figures 5.5 and 5.6 that higher effective plastic strain occurs in the secondary shear zone than in the primary shear zone in both cases. However, lower maximum effective plastic strain (= 3.32) is observed in Figure 5.6 compared to 3.46 in Figure 5.5, which is due to strain gradient strengthening and consequently reduced plastic deformation. The contours of von Mises stress in Figures 5.7-5.8 show that the maximum effective stress is higher with strain gradient effects (max. von Mises stress = 1.913E+3 MPa) than without (max. von Mises stress = 8.483E+2 MPa). It can be also seen that the effective stress in the workpiece surface layers is higher for the case with strain gradient. A higher temperature (371.5, max.) is also predicted when the strain gradient effect is accounted for compared to when the strain gradient effect is not accounted for (341, max.), as seen in Figures. 5.9 and 5.10.

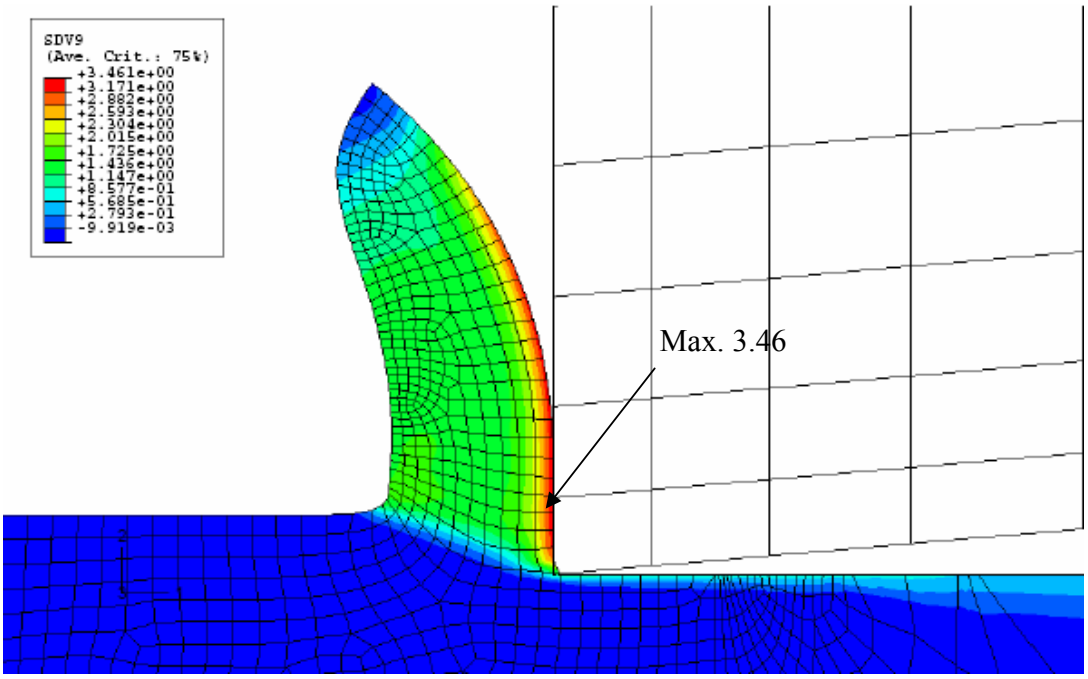

Figure 5.5. Effective plastic strain contour (w/o strain gradient effects).

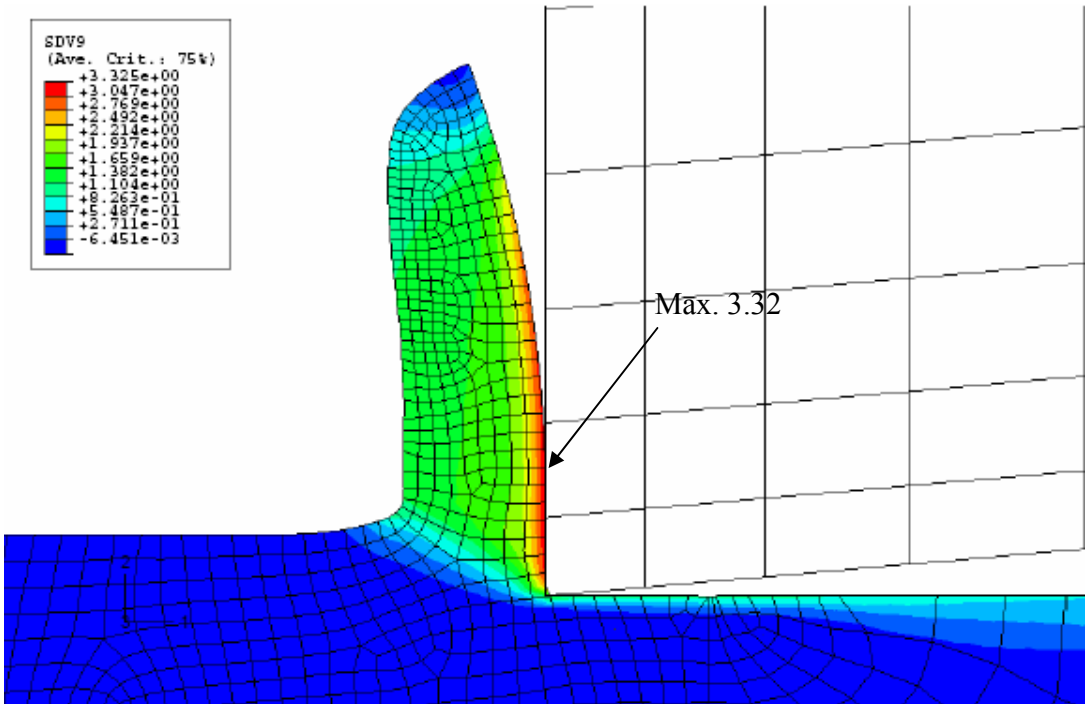

Figure 5.6. Effective plastic strain contour (with strain gradient effects).

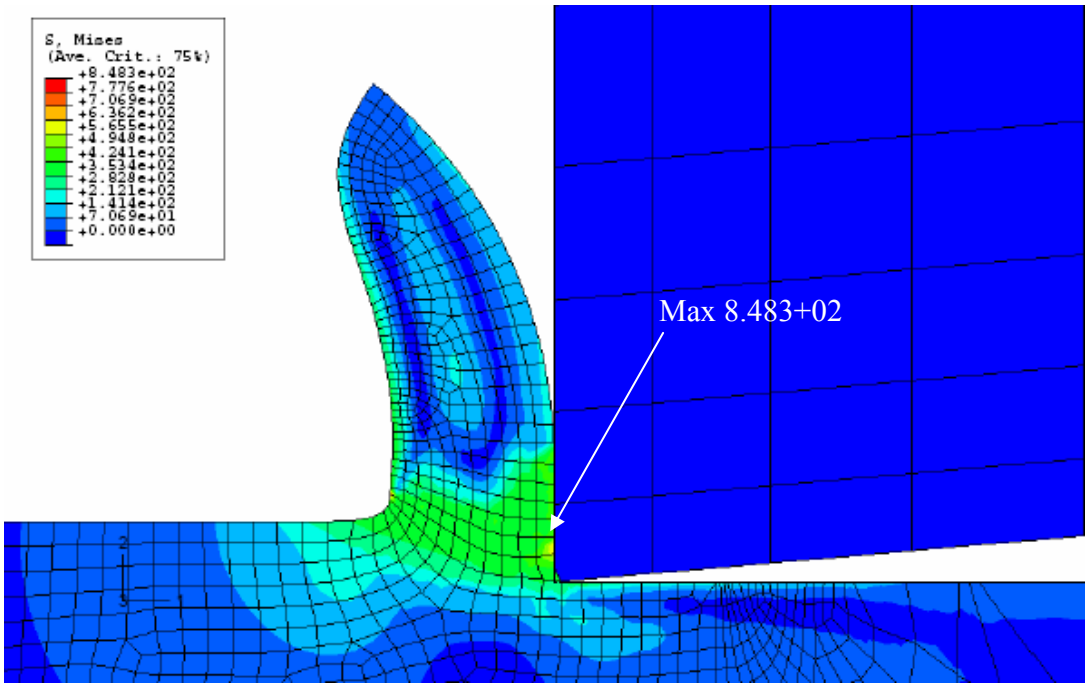

Figure 5.7. von Mises Stress contour (w/o strain gradient effect).

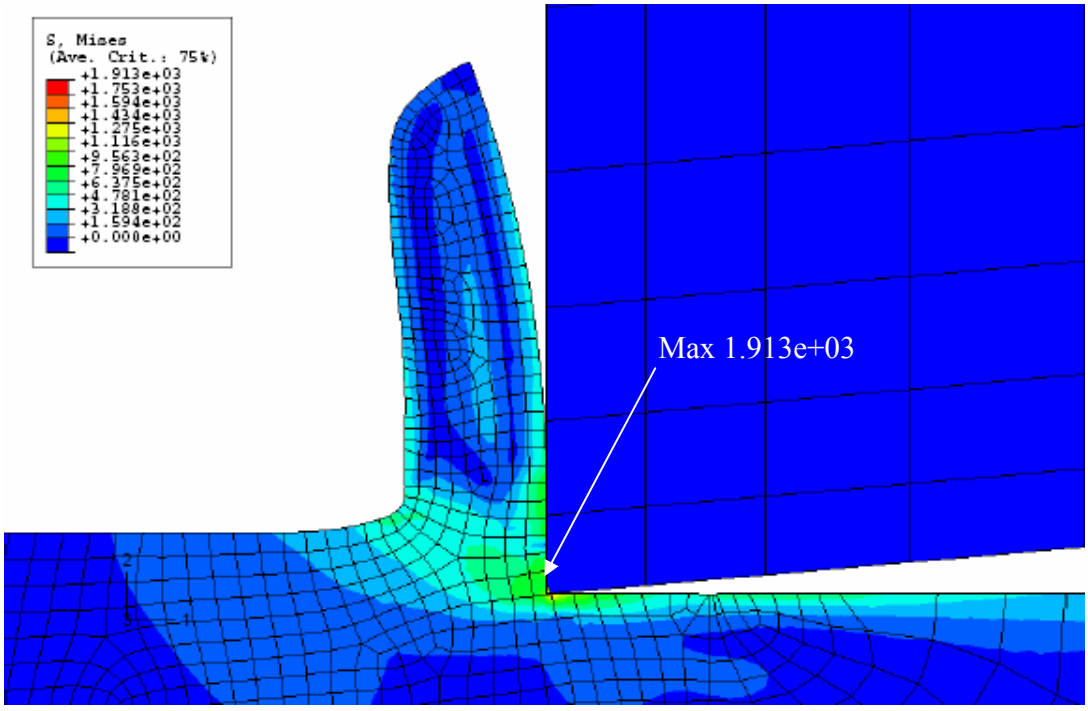

Figure 5.8. von Mises Stress contour (with strain gradient effect).

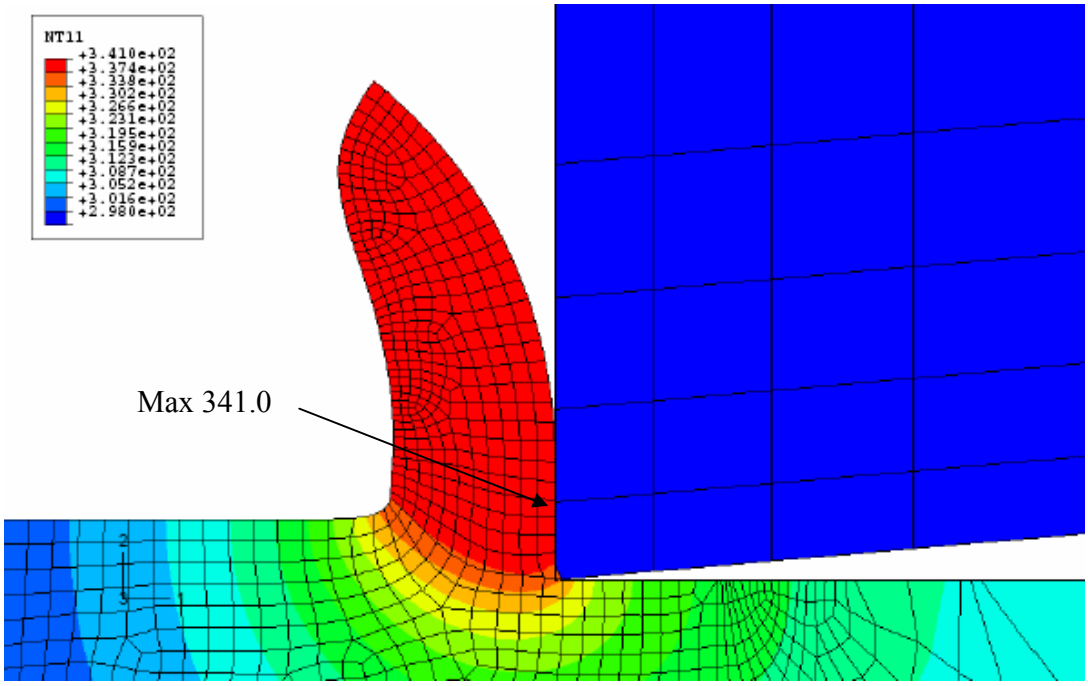

Figure 5.9. Temperature contour (w/o strain gradient effect).

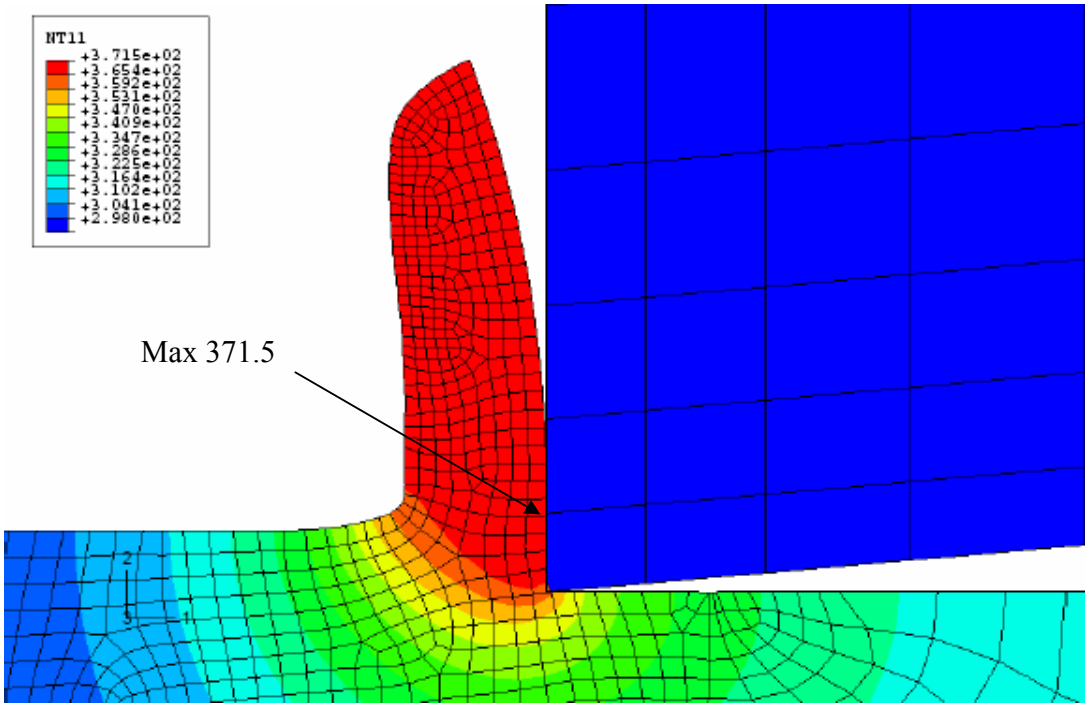

Figure 5.10. Temperature contour (with strain gradient effect).

5.2.3 Strain Gradient Effects on Specific Cutting Energy

In order to examine the strain gradient effect at a low cutting speed of 10 m/min, two sets of orthogonal cutting simulations were run at uncut chip thickness values ranging from 0.5 to 10 μm. The first set of simulations was run with all terms in Eq. (3.3) while the second set of simulations was run without the strain gradient term $l\eta$ in Eq. (3.3).

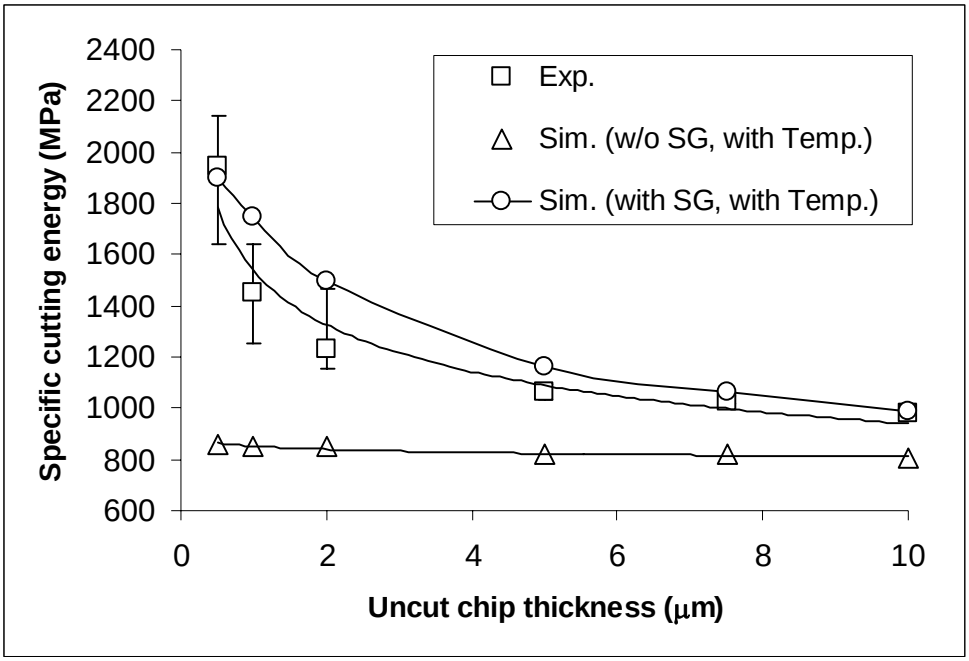

Figure 5.11. Variation of specific cutting energy with uncut chip thickness at 10 m/min.

Figure 5.11 shows a plot of the specific cutting energy versus the uncut chip thickness with and without the strain gradient effect. The specific cutting energy was computed by dividing the total force acting on the tool in the cutting direction by the product of the workpiece width (unity) and uncut chip thickness. It can be seen that the specific cutting energy predicted by the model with strain gradient effect matches well with the experimental data and captures the size effect. For the model without strain

gradient effect, the predicted specific cutting energy remains fairly constant with decrease in uncut chip thickness. It is clear from Figure 5.11 that at a low cutting speed and for small uncut chip thickness, strain gradient strengthening is the dominant mechanism responsible for the size effect.

Table 5.1. Predicted forces with and without strain gradient (SG) effect.

Uncut chip thickness (μm)	Cutting force, F_c (sim.) (N)		Thrust force, F_t (sim.) (N)	
	with SG	w/o SG	with SG	w/o SG
0.5	0.95	0.5	0.1	0.09
1	1.75	1.01	0.25	0.2
2	3	1.7	0.5	0.32
5	5.8	4.12	1.05	0.78
7.5	7.95	6.13	1.45	1.18
10	9.86	8.03	1.84	1.55

The predicted cutting and thrust forces with and without strain gradient effect are listed in Table 5.1. It can be seen that strain gradient strengthening influences the cutting force significantly, especially at small uncut chip thickness values. The percent difference between the cutting force predicted with strain gradient effect and cutting force without strain gradient effect increases from 22% at 10 μm uncut chip thickness to 90% at 0.5 μm uncut chip thickness. This shows that it is important to consider the strain gradient effect in order to obtain accurate force predictions for cutting processes at micron/submicron uncut chip thickness levels.

Figures 5.12 and 5.13 plot the temperature contours for 0.5 μm and 10 μm uncut chip thickness, respectively, at 10 m/min cutting speed. It can be seen from the plots that the temperature is uniformly distributed within the chip in both cases. The difference between the maximum temperatures is less than 15 ^{o}C, which suggests that the temperature effect is small at a cutting speed of 10 m/min.

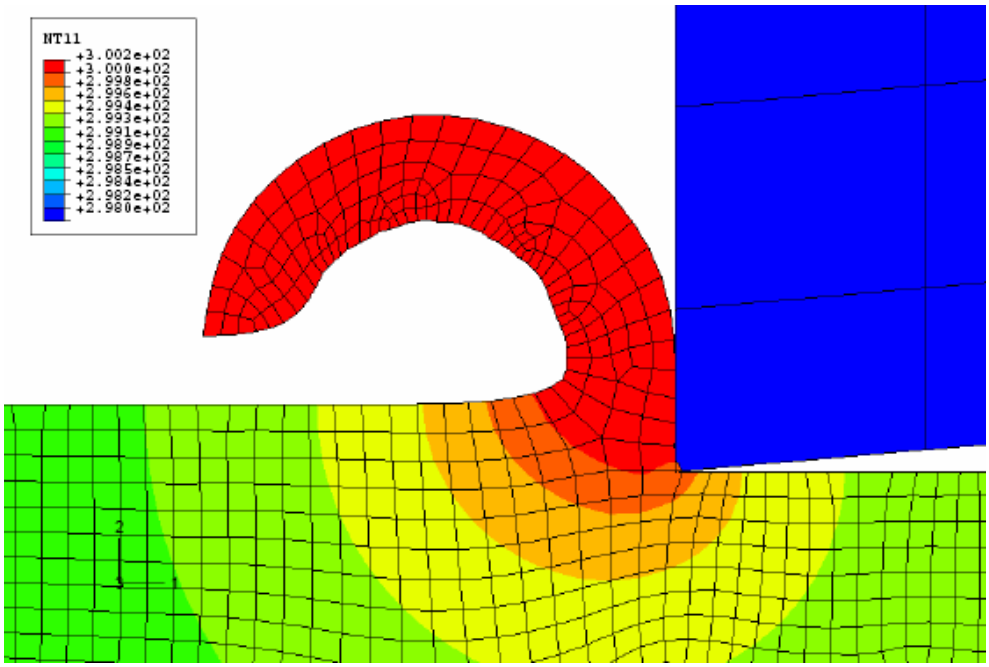

Figure 5.12. Temperature contour for 0.5 µm uncut chip thickness and 10 m/min cutting speed.

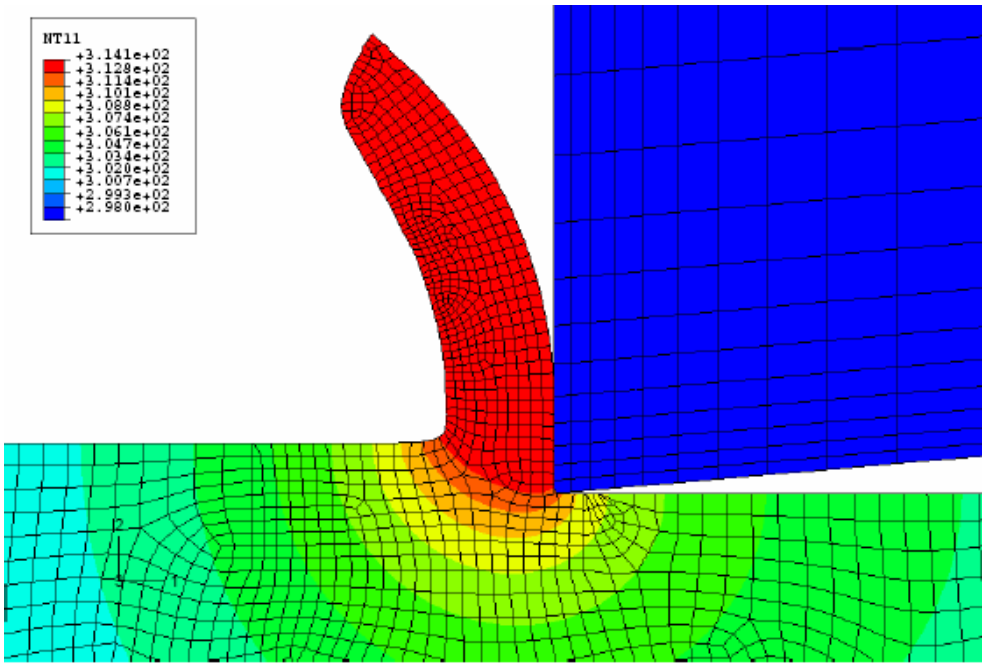

Figure 5.13. Temperature contour for 10 µm uncut chip thickness and 10 m/min cutting speed.

5.3 Temperature Effects

In machining, a large amount of heat is generated due to the plastic work and friction at the tool-chip interface. It is observed that the strength of the material is usually lowered by an increase in temperature and vice-versa. From dislocation mechanics, material strength in plastic deformation of metal crystals is determined by the motion of dislocations and their interactions. An increase in temperature increases the thermodynamic probability of the dislocations achieving sufficient energy to move past a peak in the potential thereby producing a softening effect on the flow stress.

It is found that the temperature gradient within the chip changes with uncut chip thickness. Specifically, the maximum temperature within the secondary shear zone decreases with reduction in uncut chip thickness. The temperature drop in the secondary shear zone tends to have a hardening effect on the material strength, which in turn causes an increase in the cutting force and consequently the specific cutting energy. The temperature gradient within the deformation zones and the temperature drop induced hardening effect on the size effect observed in specific cutting energy are analyzed in this section.

5.3.1 Temperature Gradient Within the Deformation Zones

Figures 5.14 and 5.16 show the temperature contours within the workpiece for an uncut chip thickness of 75 μm and 7.5 μm, respectively, at 200 m/min. The temperature profile for both cases along the **a-a** direction across the chip thickness and along the **b-b** direction across the primary deformation zone are plotted versus distance from the origin *o* in Figures 5.15 and 5.17. Figure 5.14 shows that range of temperatures exists in the **a-a**

direction across the chip thickness and in the **b-b** direction across the primary deformation zone.

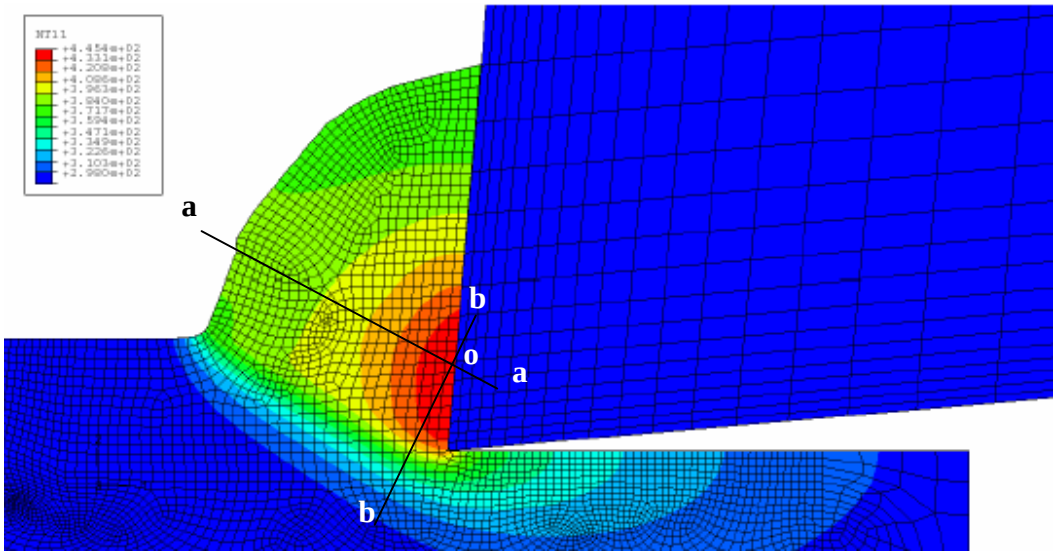

Figure 5.14. Temperature contour at 75 μm uncut chip thickness and 200 m/min cutting speed.

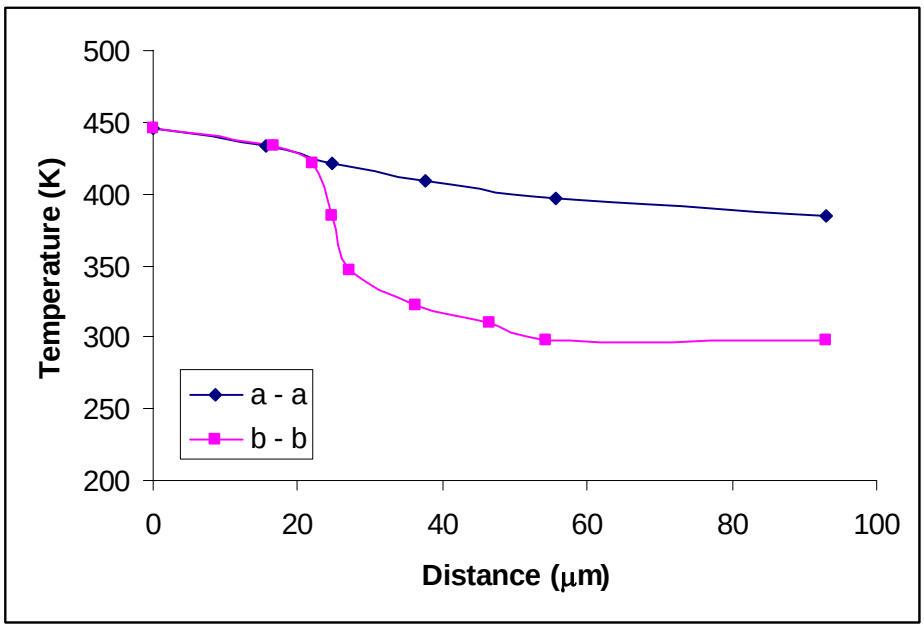

Figure 5.15. Temperature gradient along a-a and b-b directions at 75 μm uncut chip thickness and 200 m/min cutting speed.

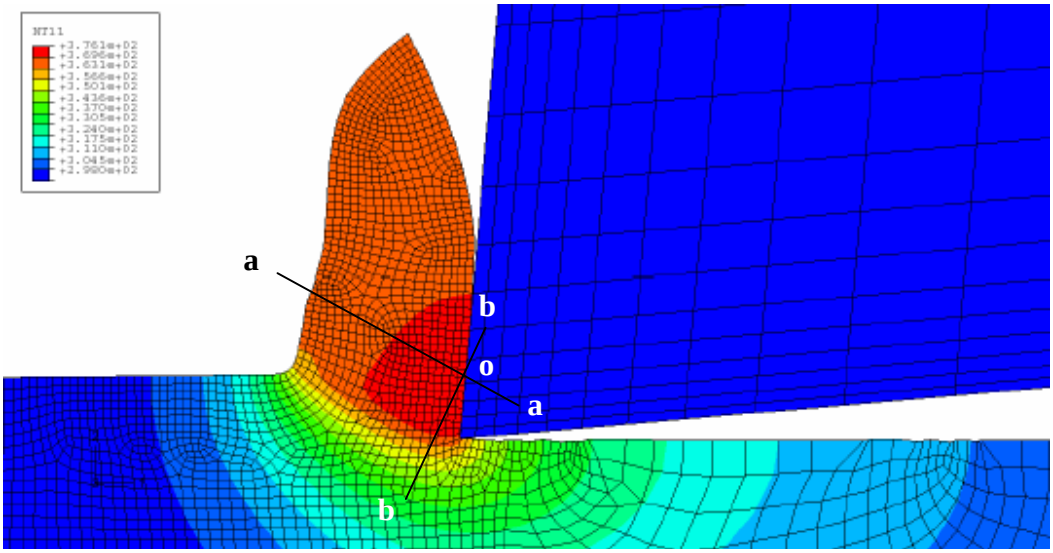

Figure 5.16. Temperature contour at 7.5 µm uncut chip thickness and 200 m/min cutting speed.

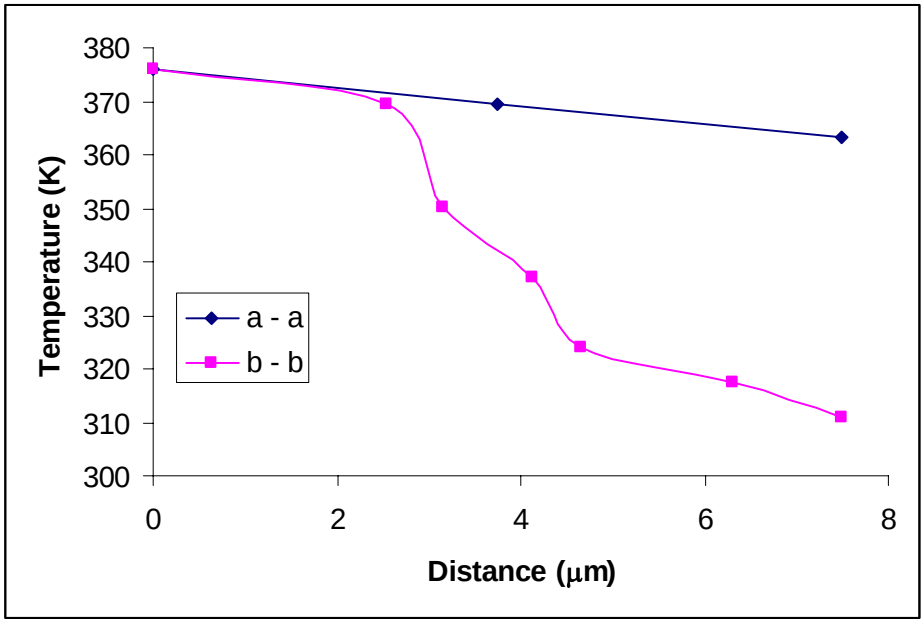

Figure 5.17. Temperature gradient along a-a and b-b directions at 7.5 µm uncut chip thickness and 200 m/min cutting speed.

Figure 5.16 shows the temperature contour within the workpiece for an uncut chip thickness of 7.5 µm at 200 m/min. The temperature distribution within the workpiece

shows a different pattern compared to the 75 μm uncut chip thickness case shown in Figure 5.14. The steady state temperature distribution shows a more uniformly distributed temperature profile within the chip. It can be seen from Figures 5.15 and 5.17 that steeper temperature gradient exists in the direction across the primary deformation zone than in the direction across the chip thickness for both cases.

5.3.2 Temperature Effects on Specific Cutting Energy

In order to examine the temperature effect at a cutting speed of 200 m/min, two sets of orthogonal cutting simulations were run from 20 to 200 μm uncut chip thickness. The first set of simulations was run with all terms in Eq. (3.3) while the second set of simulations was run without the temperature term in Eq. (3.5) (and hence in Eq. (3.3)).

Figure 5.18 shows a plot of the specific cutting energy versus uncut chip thickness with and without the temperature effect. It can be seen that the specific cutting energy predicted by the model including the temperature effect is in good agreement with the experimental data and captures the size effect. Simulations without the temperature effect show that the specific cutting energy remains fairly constant with reduction in uncut chip thickness. Clearly, at the higher cutting speed the temperature effect is dominant compared to the strain gradient effect, especially at large uncut chip thickness values ($\geq$ 20 μm).

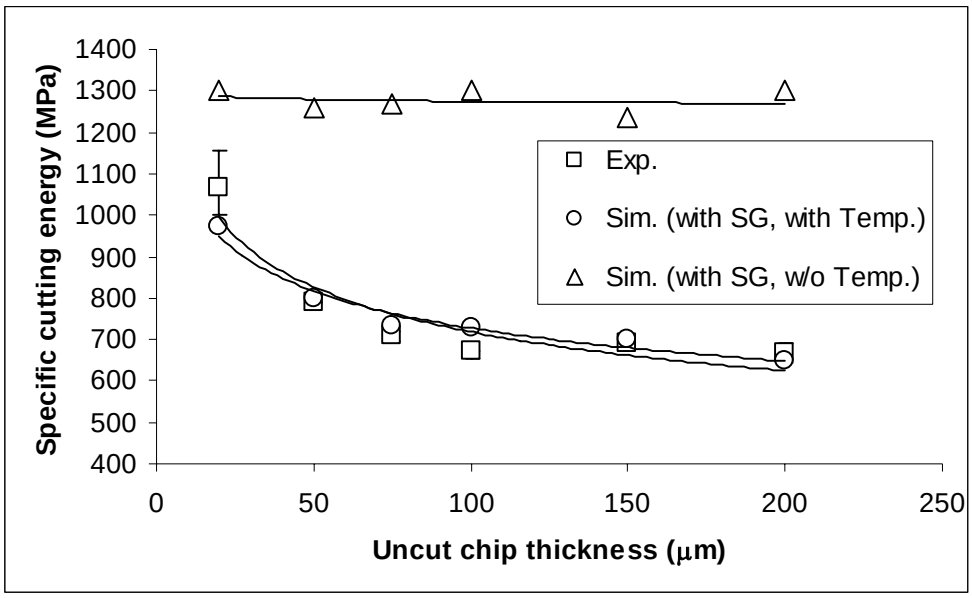

Figure 5.18. Variation of specific cutting energy with uncut chip thickness at 200 m/min.

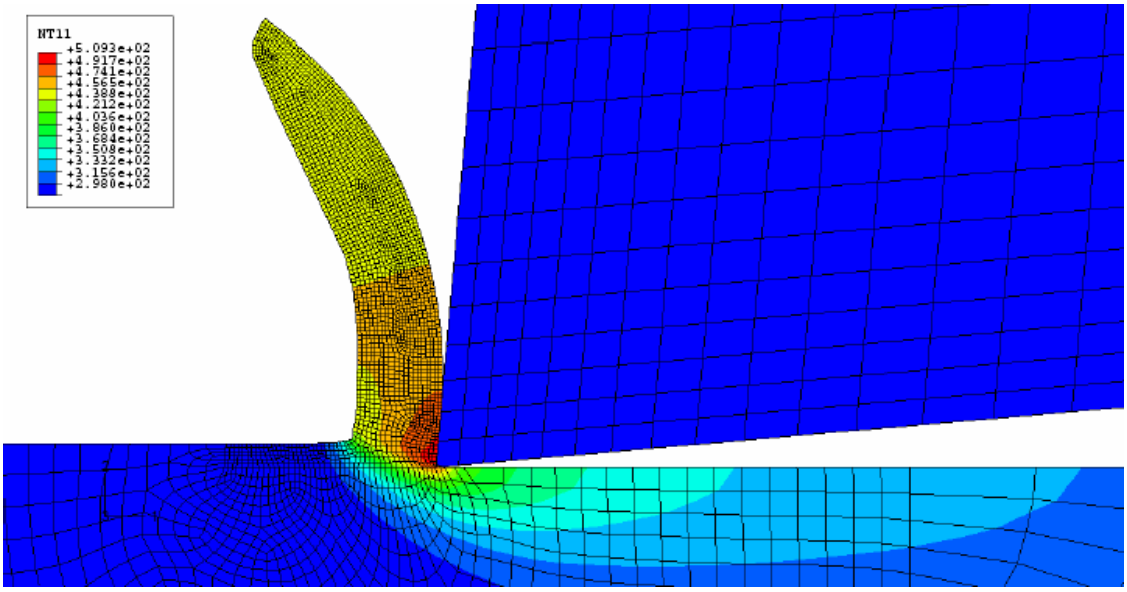

Figure 5.19. Temperature contour at 20 μm uncut chip thickness and 200 m/min cutting speed.

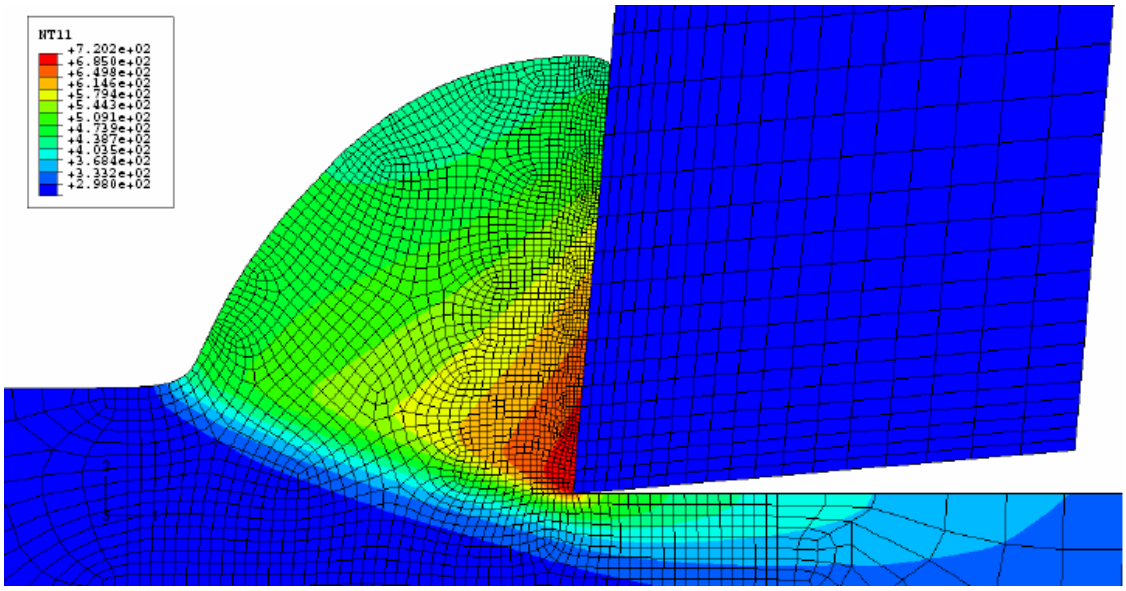

Figure 5.20. Temperature contour at 200 µm uncut chip thickness and 200 m/min cutting speed.

Figures 5.19 and 5.20 show the temperature contours for 20 µm and 200 µm uncut chip thickness at a cutting speed of 200 m/min. A significant difference in the maximum temperature (about 200 degree) within the secondary shear zone is observed, which affects the material strength within the secondary deformation zone.

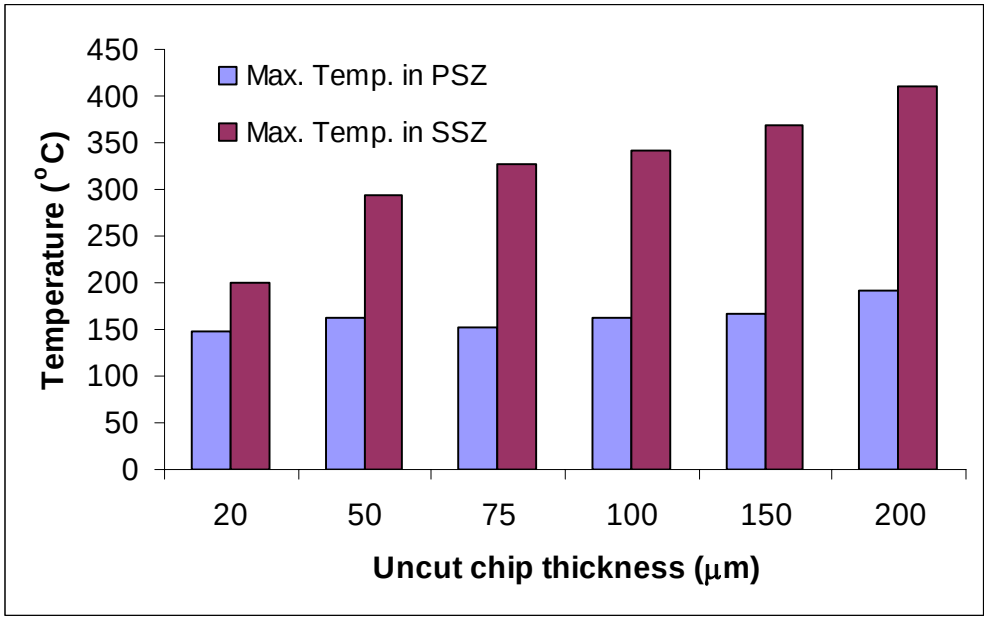

Figure 5.21. Variation of maximum temperature in the primary and secondary shear zones at 200 m/min cutting speed (PSZ: primary shear zone, SSZ: Secondary shear zone).

The maximum temperatures in the primary and secondary shear zones versus uncut chip thickness are shown in Figure 5.21. It can be seen that the maximum temperature in the secondary shear zone drops by nearly 200°C while the maximum temperature in the primary shear zone remains almost unchanged with a decrease in uncut chip thickness from 200 μm to 20 μm. This directly supports the reasoning proposed by Kopalinsky and Oxley [13] and Marusich [26] that the size effect in machining at high cutting speeds and large uncut chip thickness is primarily caused by an increase in the shear strength of the workpiece material due to a decrease in the tool-chip interface temperature.

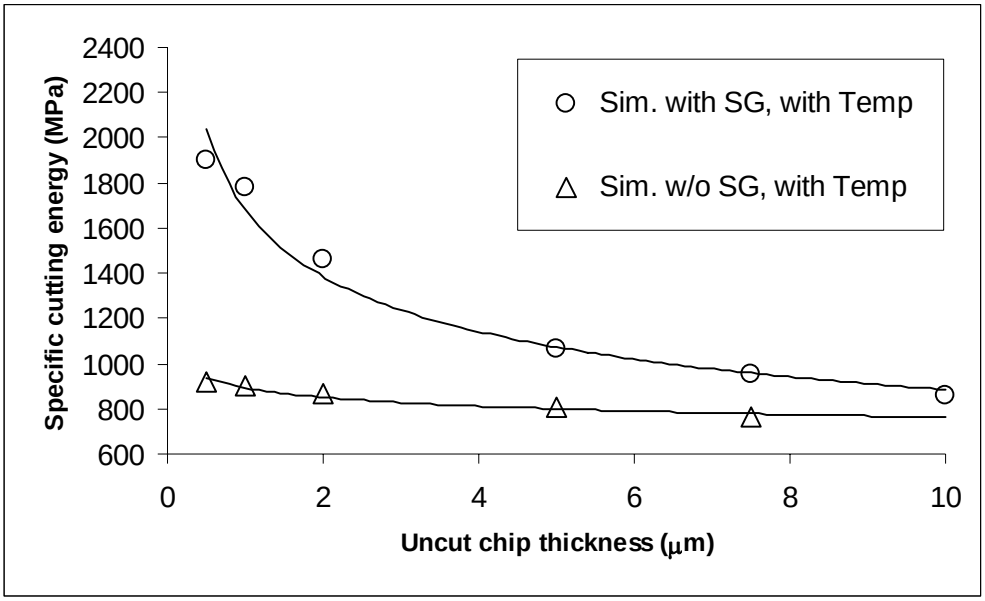

Figure 5.22. Variation of specific cutting energy with uncut chip thickness at 240 m/min.

It is also of interest to examine the contributions of the two material strengthening factors, strain gradient strengthening and material strengthening due to a drop in the cutting temperature, at cutting conditions characterized by high cutting speed and small uncut chip thickness. Under such conditions, both temperature and strain gradient effects may contribute to the size effect in specific cutting energy. Therefore, orthogonal cutting simulations were run at a cutting speed of 240 m/min for uncut chip thickness values ranging from 0.5 to 10 μm. Figure 5.22 shows a plot of the specific cutting energy versus uncut chip thickness with and without strain gradient effect. It can be seen that the specific cutting energy predicted by the model with strain gradient almost doubles when the uncut chip thickness is reduced from 10 μm to 0.5 μm, while only about 10% of the increase is captured by the model without strain gradient effect. The plot shows that at a high cutting speed and small uncut chip thickness, strain gradient strengthening is more

significant than material strengthening due to a drop in the secondary shear zone temperature.

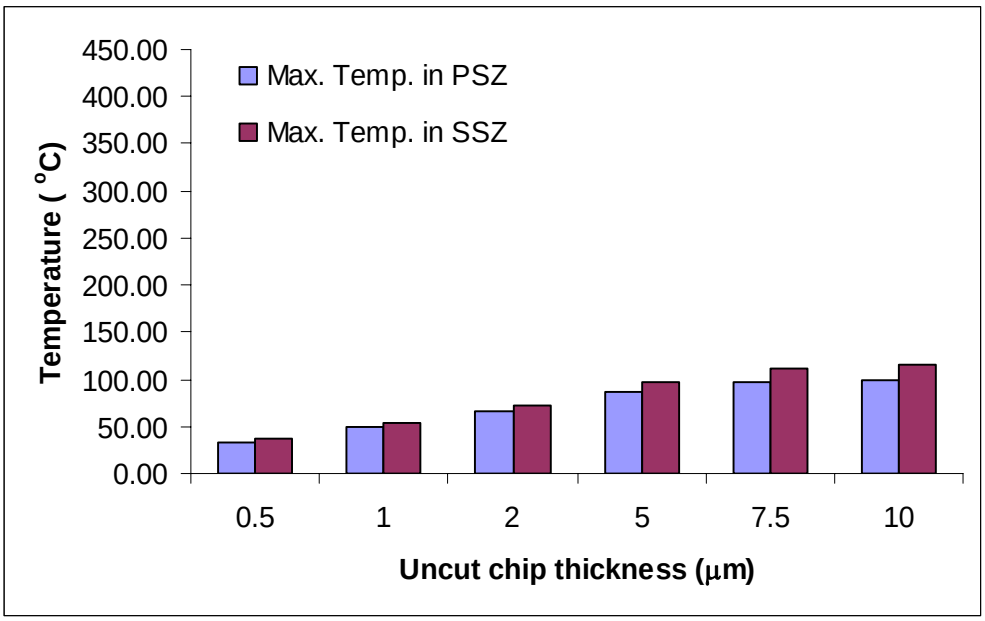

Figure 5.23. Variation of maximum temperature in the primary and secondary shear zones at 240 m/min cutting speed (PSZ: primary shear zone, SSZ: Secondary shear zone).

It is evident from Figure 5.23 that the temperature drop at the tool-chip interface is less prominent at high cutting speeds and small uncut chip thickness, which suggests that the temperature effect contributes only a small fraction of the size effect in micro-cutting under such conditions.

5.4 Tool Edge Radius Effects

Tool edge radius has been studied by many researchers and linked to the size effect in micro-cutting. Since the edge radius of the cutting tool normally falls in the range of several microns to several hundred microns, it has been suggested that the edge radius is the main factor responsible for the size effect observed in micro-cutting [15, 28-

30]. However, size effect is still observed in micro-cutting experiments with sharp tool [15] (where the edge radius of the tool is less than 10% of the uncut chip thickness). In previous literature review it has been established that the edge radius is not the only factor, but one of the factors that contributes to size effect.

The tool edge radius is known to affect the micro-cutting process by changing the geometrical parameters such as the effective rake angle [15], enhancing the plowing effect [29] and introducing an indenting force component [30]. However, these studies are based on a mechanistic modeling approach, which does not realistically represent the condition in cutting with a radiused edge tool. In this section, a cutting tool with a finite edge radius is incorporated into the finite element model to study the edge radius effect and its contribution to size effect.

Cutting tools with two different edge radii, 5 μm and 20 μm, are used in the cutting simulation. The tool with the edge radius of 5 μm is used in cutting simulations of uncut chip thickness ranging from 3 μm to 20 μm while the tool with the edge radius of 20 μm is used in cutting simulations of uncut chip thickness ranging from 7.5 μm to 75 μm.

Orthogonal cutting simulations have been conducted with the two edge radii, with and without strain gradient effect, at a cutting speed of 200 m/min. The *t/r* ratio, ratio of uncut chip thickness *t* to edge radius *r*, varies from 0.375 to 3.75 and from 0.6 to 4.0 for the 5 μm and 20 μm edge radius cases, respectively.

$t / r = 0.6$

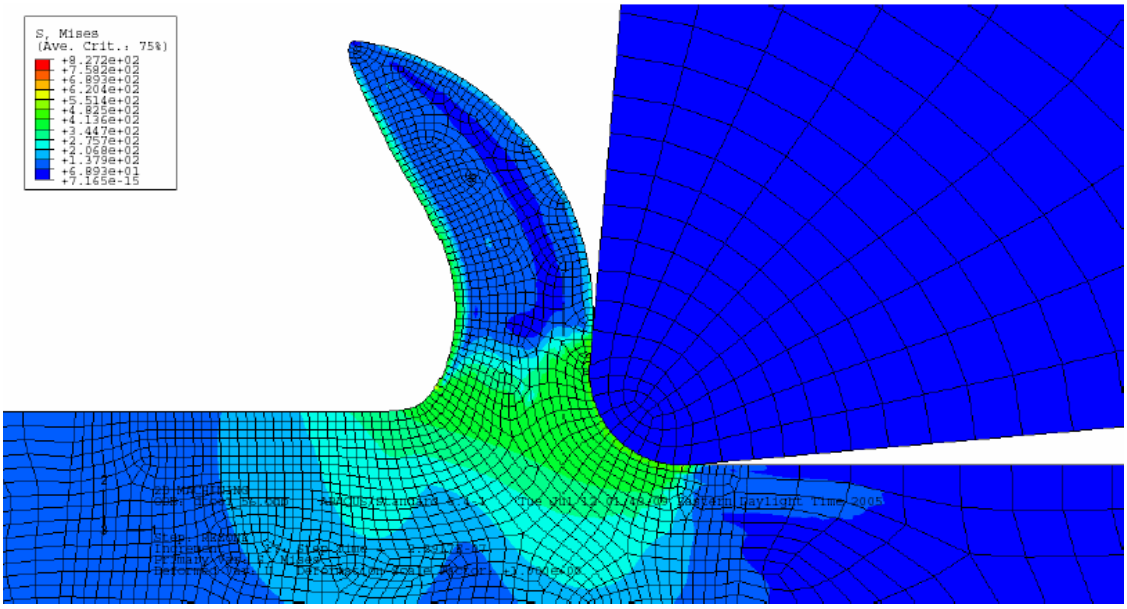

Figure 5.24. Steady state von Mises stress contour for edge radius of 5 μm, uncut chip thickness of 3 μm, cutting speed of 200 m/min, w/o strain gradient effect.

$t / r = 1$

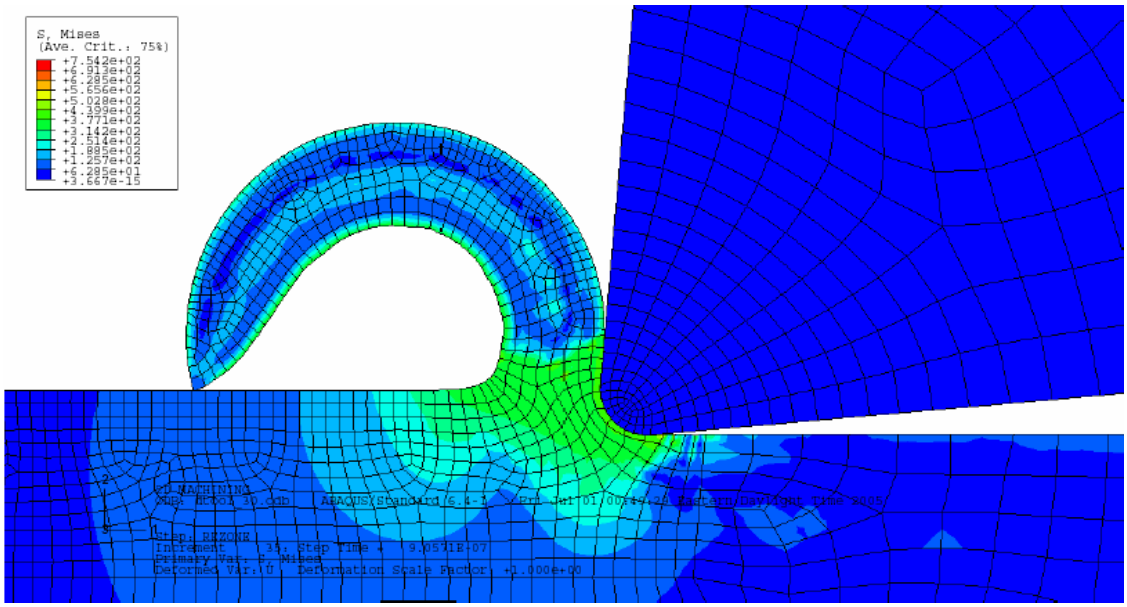

Figure 5.25. Steady state von Mises stress contour for edge radius of 5 μm, uncut chip thickness of 5 μm, cutting speed of 200 m/min, w/o strain gradient effect.

$t / r = 1.5$

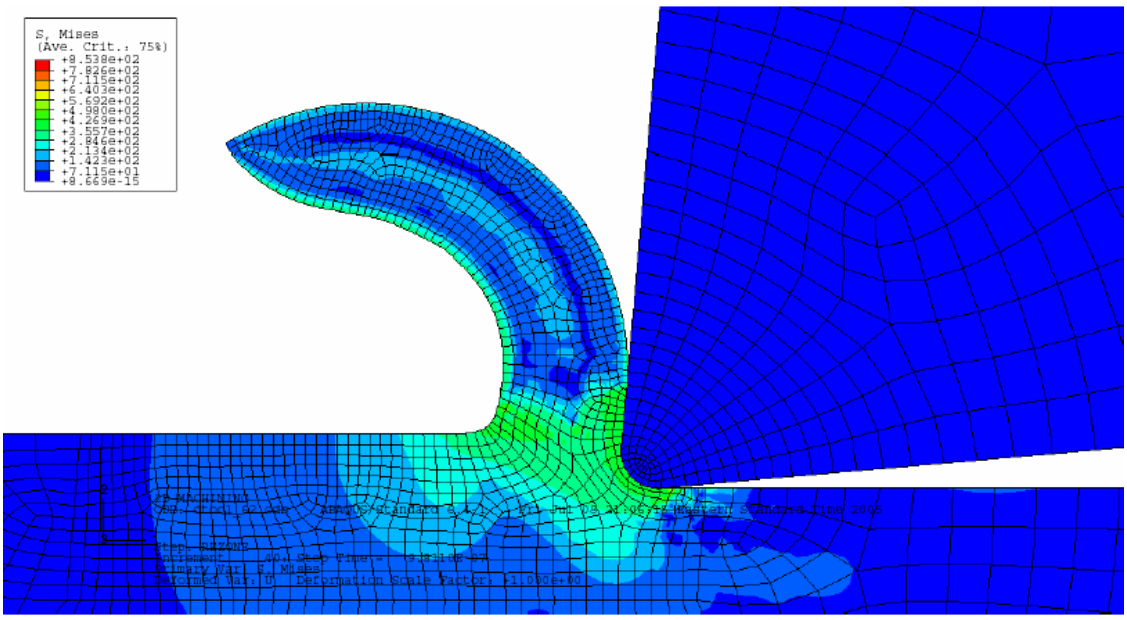

Figure 5.26. Steady state von Mises stress contour for edge radius of 5 µm, uncut chip thickness of 7.5 µm, cutting speed of 200 m/min, w/o strain gradient effect.

$t / r = 2$

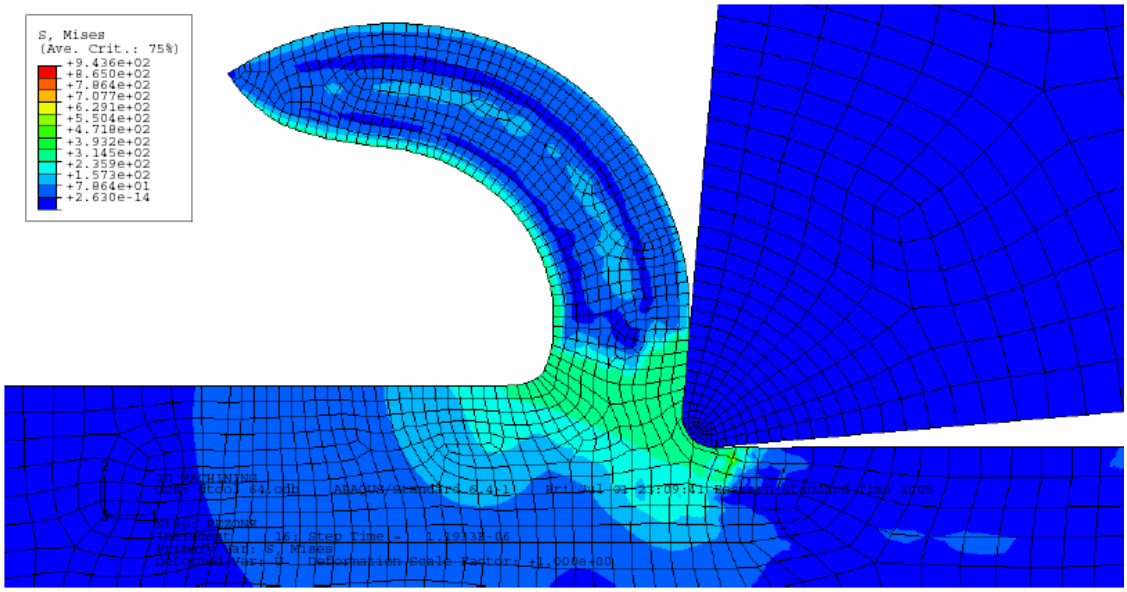

Figure 5.27. Steady state von Mises stress contour for edge radius of 5 µm, uncut chip thickness of 10 µm, cutting speed of 200 m/min, w/o strain gradient effect.

$t / r = 4$

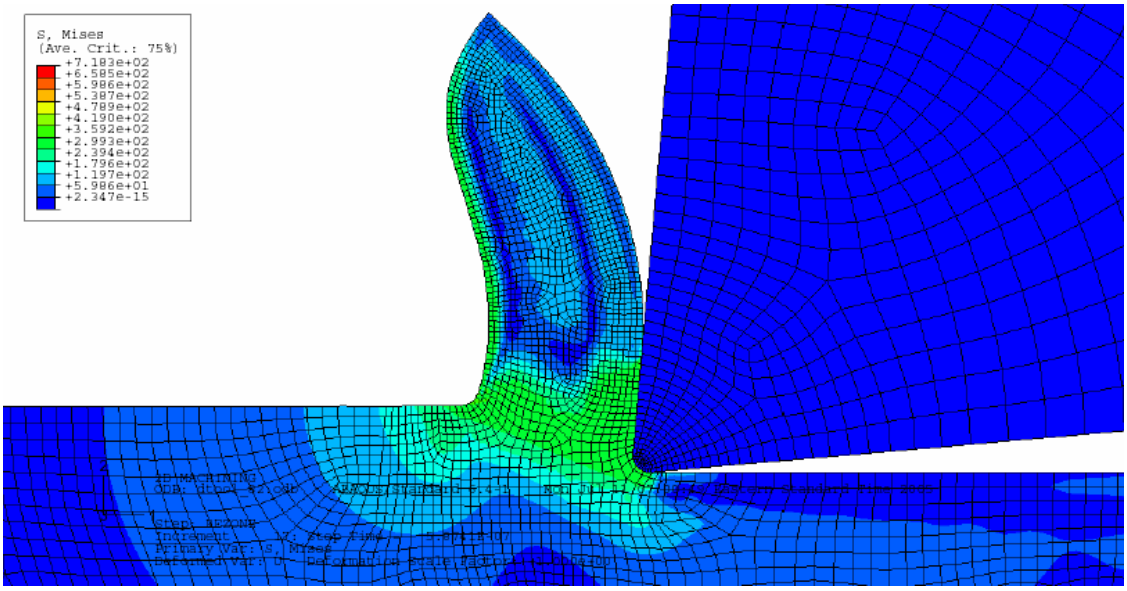

Figure 5.28. Steady state von Mises stress contour for edge radius of 5 µm, uncut chip thickness of 20 µm, cutting speed of 200 m/min, w/o strain gradient effect.

For the simulations without the strain gradient effect, the von Mises stress distribution in the workpiece is shown in Figures 5.24-5.28 for different *t/r* ratios. In call cases it can be seen that the zone of plastic deformation (in green) extends below the cutting edge. It can be seen in Figure 5.30 that the specific cutting energy increases by about 100% when the *t/r* ratio decreases from 4 to 0.6, which indicates that size effect is captured by the simulation using a radiused edge tool even though the strain gradient effect is not included. Examining the maximum temperature drop at tool-chip interface from 75 µm to 7.5 µm uncut chip thickness for tool with 20 µm edge radius and sharp tool, larger temperature drop of 69 ^{o}C was predicted by sharp tool comparing to 41 ^{o}C predicted by edge radiused tool. However, for both cases the temperature drop is not significantly large to account for the size effect observed in simulations. This clearly

suggests that the presence of the tool edge radius is responsible for the observed size effect either directly or indirectly.

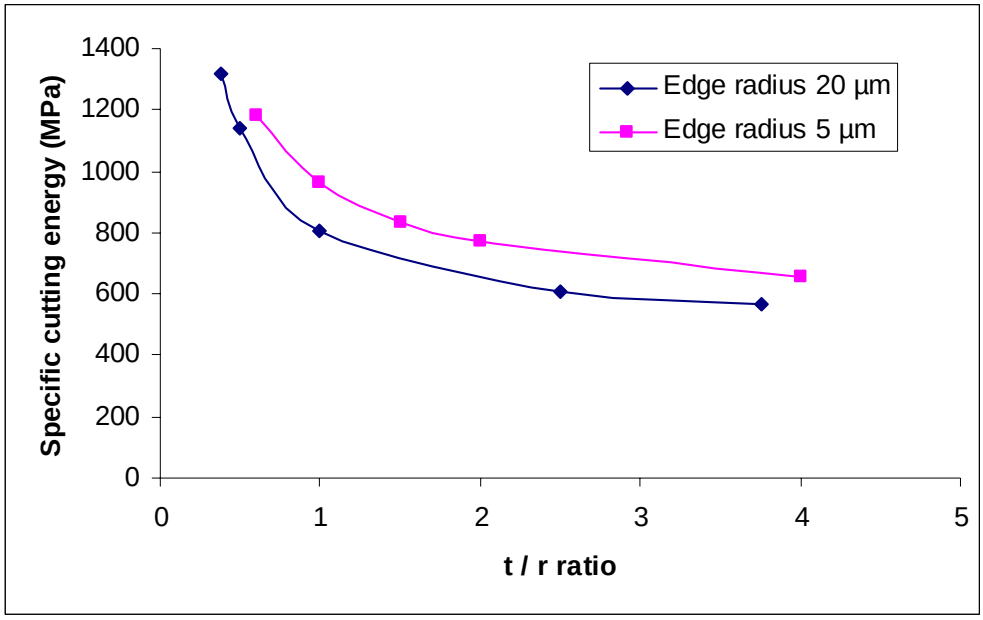

Figure 5.29. Variation of specific cutting energy with *t/r* ratio for two edge radii, without strain gradient effect.

However, comparison of the predicted specific cutting energy for the radiused edge tool with strain gradient effect and the predicted specific cutting energy without strain gradient effect, shown in Figure 5.31, reveals that when accounting only for the tool edge radius only a fraction of the total increase in specific cutting energy with decrease in uncut chip thickness is captured. The model prediction with strain gradient effect and radiused edge tool shows a much higher increase in specific cutting energy.

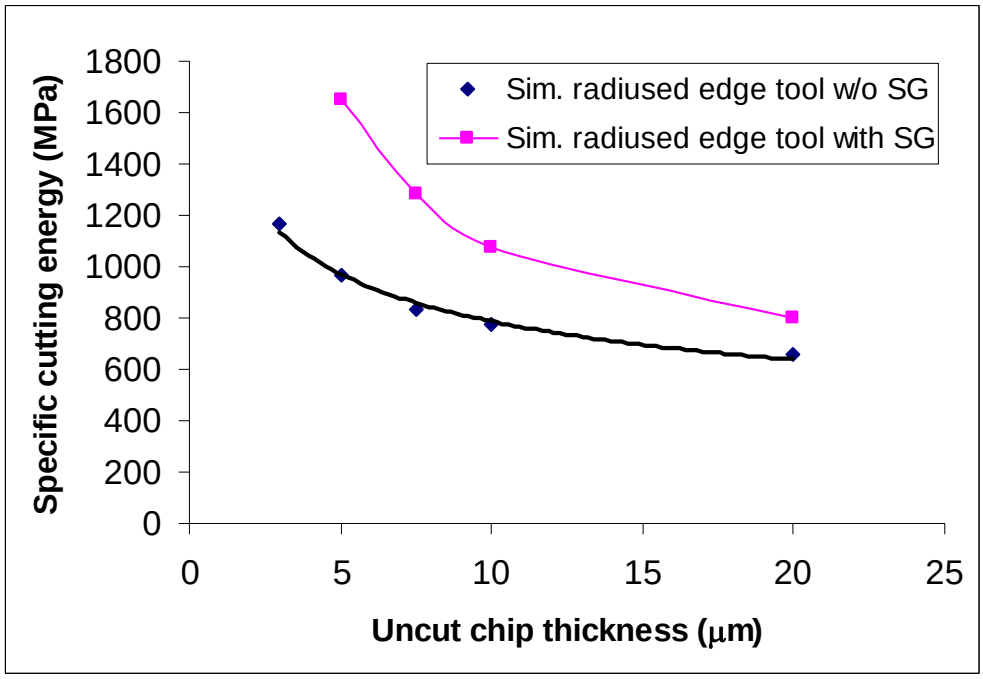

Figure 5.30. Variation of specific cutting energy versus uncut chip thickness for radiused edge tool, with and without strain gradient effect.

To investigate the underlying mechanisms for the size effect captured by the simulation using radiused edge tool even in the absence of the strain gradient effect, simulations were run using a sharp tool and a tool with 20 μm edge radius for the 200 m/min cutting speed. The tool and workpiece material properties, boundary and initial conditions and friction interaction at two uncut chip thickness levels of 7.5 μm and 75 μm are set to the same (see page 58 in Chapter 3, Tables 4.4-4.6, page 88 in Chapter 4)

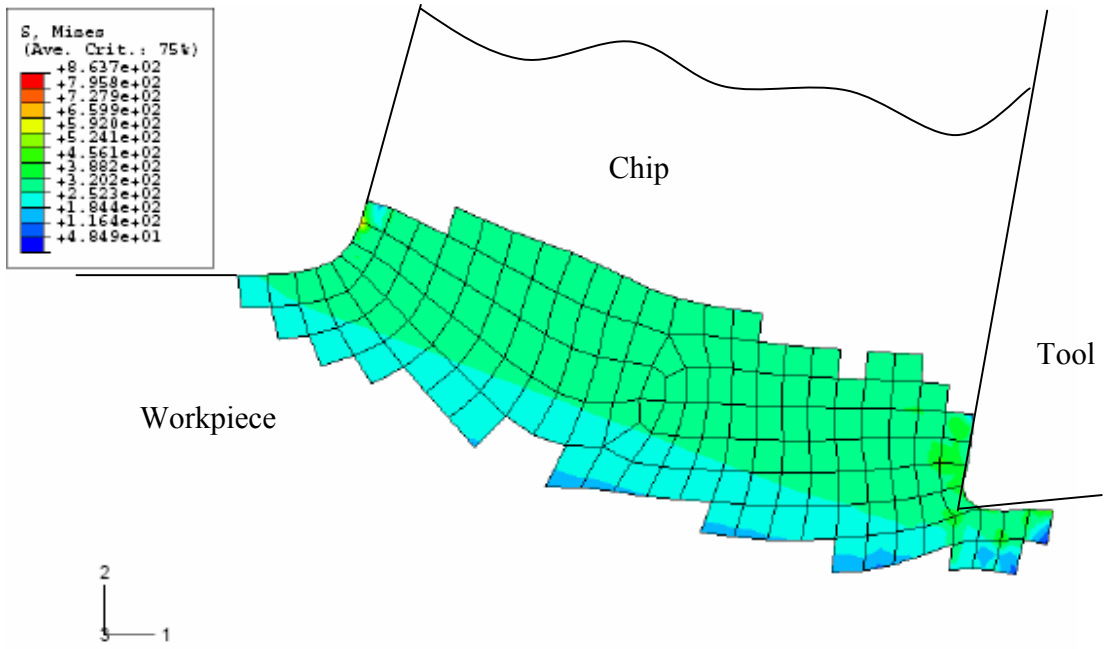

Figure 5.31. Active plastic yielding region for uncut chip thickness of 7.5 µm and sharp tool, 200 m/min cutting speed, w/o strain gradient.

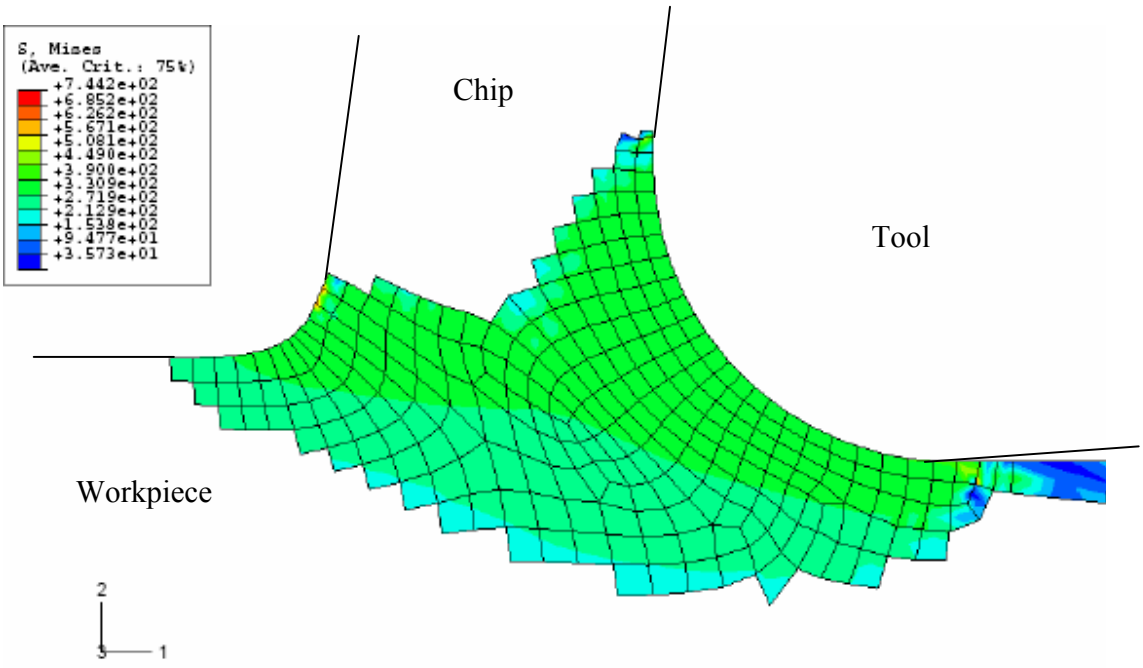

Figure 5.32. Active plastic yielding region for uncut chip thickness of 7.5 µm and radiused edge tool, 200 m/min cutting speed, w/o strain gradient.

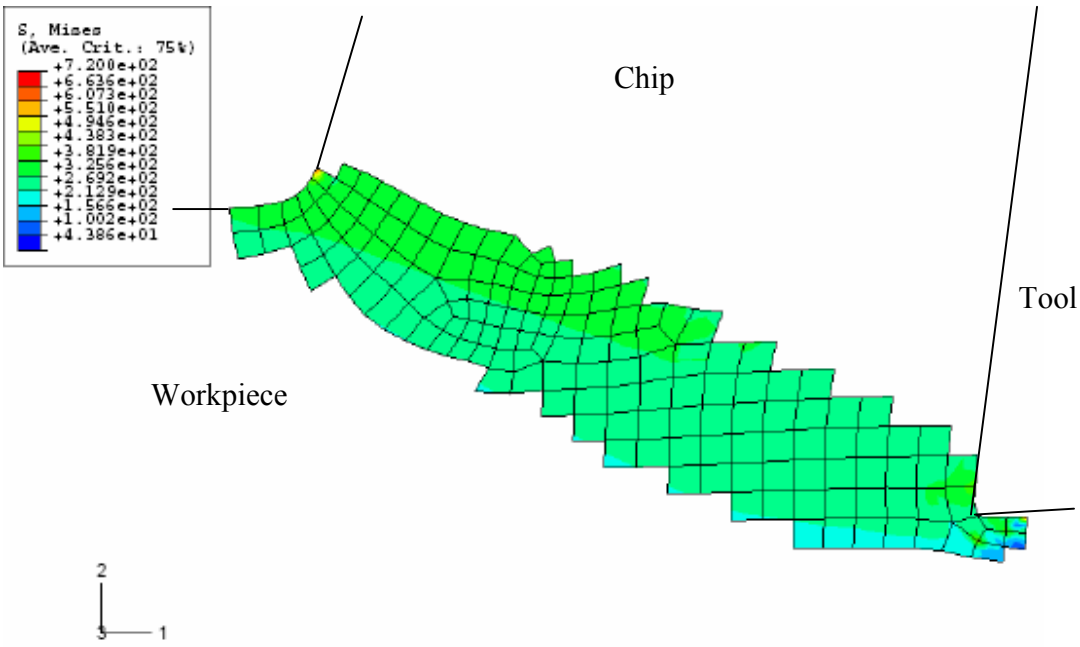

Figure 5.33. Active plastic yielding region for uncut chip thickness of 75 μm and sharp tool, 200 m/min cutting speed, w/o strain gradient.

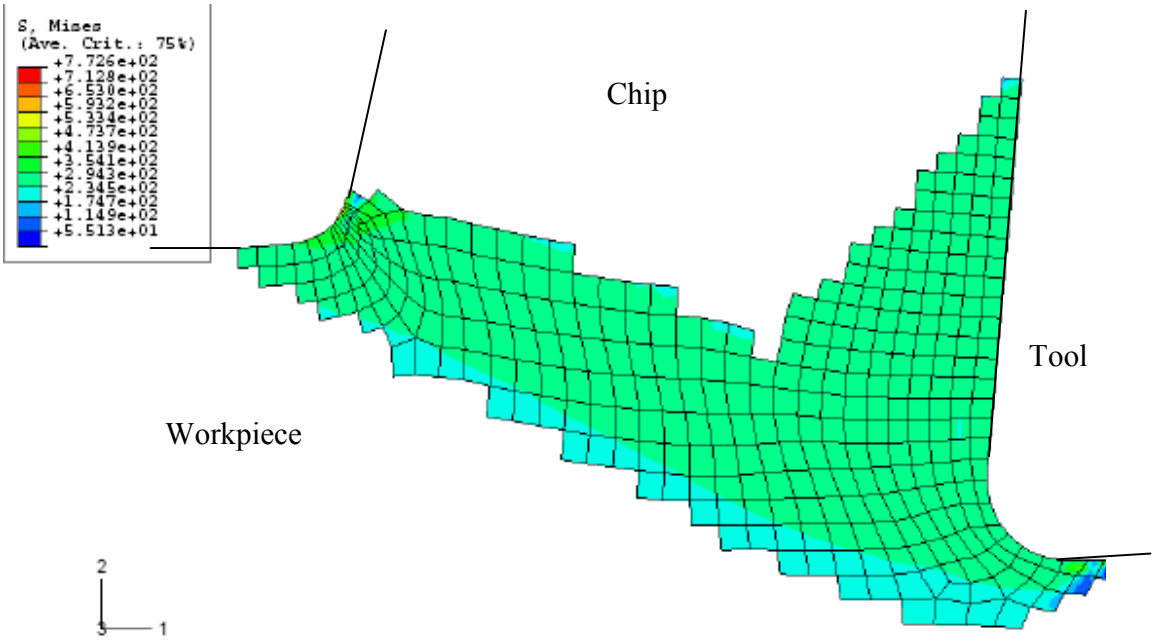

Figure 5.34. Active plastic yielding region for uncut chip thickness of 75 μm and radiused edge tool, 200 m/min cutting speed, w/o strain gradient.

The active plastic yielding zones for the four cases can be identified by defining an element group that only includes the elements undergoing plastic deformation at the current instant. The shapes of the active plastic yielding zones for the sharp tool and the radiused edge tool at the two uncut chip thickness levels are shown in Figures 5.32-5.35. It can be seen that the plastic shear zones for the sharp tool are thinner compared to the plastic shear zones obtained for the radiused edge tool, which are wider and extend toward the rake face of the tool. The difference in plastic shear zone size and shape shows that the edge radius of the tool changes the material flow pattern around the tool tip by expanding and widening the plastic shear zone.

The tool-chip contact lengths for the four cases are also listed in Table 5.2. It is observed that at 75 μm uncut chip thickness, the sharp tool and radiused edge tool yield comparable contact lengths. The contact length for the radiused edge tool is only about 10% higher than for the sharp tool. However, the difference in contact lengths becomes larger at 7.5 μm uncut chip thickness, where the tool-chip contact length of radiused edge tool is 300% higher than for the sharp tool. This suggests that much higher energy associated with frictional interaction at the tool-chip interface is consumed at the small uncut chip thickness of 7.5 μm when using a radiused edge tool. Therefore, an additional reason for the size effect being captured by the radiused edge tool even in the absence of strain gradient effects is the increased frictional interaction at the tool-chip interface at smaller uncut chip thickness values.

Table 5.2. Tool-chip contact length

	Simulated tool-chip contact length (mm)	
	7.5 μm uncut chip thickness	75 μm uncut chip thickness
Sharp tool	0.01	0.11
Tool with 20 μm edge radius	0.03	0.13

5.5 Discussion of Length Scales in Micro-cutting

The length scale commonly associated with the size effect in micro-cutting is the edge radius of the tool. A number of researchers [15, 28-30] have considered the edge radius as the primary reason for the observed nonlinearity in specific cutting energy. The argument made by these researchers is that the nonlinear increase in specific cutting energy occurs at an uncut chip thickness value close to the edge radius of the cutting tool.

In the present work, the strain gradient plasticity is implemented to more accurately represent the material behavior in micro-cutting. As shown in Chapter 3, strain gradient based finite element model developed in this work can capture the size effect satisfactorily, especially at small uncut chip thickness levels. An additional material characteristic length scale, l, is introduced in strain gradient plasticity, as given in Eq. (3.4). The material length scale l in strain gradient plasticity is a function of material properties such as shear modulus, yield stress and the Burgers vector. It was shown earlier that the strain gradient effect is significant only when the product of the material length scale l and effective strain gradient η is comparable to or greater than the $f^2(\varepsilon, \dot{\varepsilon}, T)$ term in Eq. (3.3). In other words, under conditions where the strain gradient effect is dominant, the nonlinearity in specific cutting energy should start to occur at or

near the material length scale l. This was shown to be true for cases where the strain gradient strengthening effect is prominent, as shown in Figure 5.11. The purpose of this section is to examine the applicability of the two length scales – edge radius and the material length scale l - via analysis of data available in the literature.

Since the increasing trend in specific cutting energy appears as a smooth curve, a criterion is needed to define the starting point of the nonlinear increase in specific cutting energy. In this work, the point where the curvature of specific cutting energy curve reaches maximum is considered as the starting point of the nonlinearity. It should be noted that the curvature calculation is affected by the scales of the x and y axes. Consequently, the specific cutting energy is plotted in a normalized coordinate system such that both axes are scaled to a [0, 1] range. This is done by normalizing each axis by the maximum value for that axis.

Table 5.3. Comparison of length scales in micro-cutting.

Material	Measured length scale (μm)	Tool edge radius (μm)	Material length scale l (μm)	Cutting speeds (m/min)	uncut chip thickness range (μm)
Pure Zinc [17]	54.1	5		56.4	17~508
	52.1	25			
	90.1	134			
Al2024 [18]	38.1	upsharp	52.8	56.4	8.8~508
	42.1	25.4			
	42.1	101.6			
Al6061-T6 [15,118]	0.95	0.2	3.7	48	0.01~20
	56.1	396.9		300	11.9~498
	62.1	793.8			
AISI 1045 steel [13]	22	6	27.6	420	5~140
Te-Cu [15]	0.9	0.25		7.6	0.01~20
Oxygen free Cu [16]	2.01			6	0.51~10
Brass [14]	10	3 ~ 4		0.1	2~50
Al5083-H116 [present work]	1.44	0.065 ~ 0.1	5.7	10	0.5~10
	24.1	7		200	20~200

Table 5.3 summarizes the length scale analysis performed using data from literature. The measured length scale in the table represents the uncut chip thickness at which specific cutting energy starts to deviate from linearity. This is established using the maximum curvature criterion defined earlier. Note that the material length scale l is estimated based on material properties using Eq. (3.4). In some cases, sufficient information about the workpiece material is not available in the referenced papers and consequently the material length scale cannot be computed reliably. These cases in the table have no number listed in the cell for material length scale.

It can be seen from Table 5.3 that the starting point of nonlinearity in specific cutting energy determined from the maximum curvature criterion does not always correspond to the size of the tool edge radius. For several cases including Pure Zinc, Al2024, Al6061-T6 at 300 m/min, and Al5083-H116, it is significantly different from the tool edge radius. However, it is observed that the starting point of the nonlinearity is generally closer to the material length scale l especially for data generated at low cutting speed, where, as noted in earlier chapters, the strain gradient effect is dominant. For example, this observation can be made from the machining data for Pure Zinc, Al2024, Al6061-T6 at a cutting speed of 48 m/min, and Al5083-H116 at 10 m/min.

Another interesting observation that can be made from the data in Table 5.3 is the relatively small change in the measured length scale with large changes in the tool edge radius for a given cutting speed. For example, in the case of Al2024, a change in the tool edge radius from upsharp to 101.6 μm produces a minimal change in the measured length scale. Similar observations can be made in the case of Pure Zinc where a five fold change in tool edge radius (from 5 to 25 μm) produces very little change in the measured length scale (from 54.1 to 52.1 μm). However, a significant change in the cutting speed does lead to a noticeable change in the measured length scale. This can be seen for Al6061-T6 and Al5083-H116. This is consistent with the argument made earlier in this chapter that the contribution of the temperature drop in the secondary deformation zone with decrease in uncut chip thickness to size effect is more significant at higher cutting speeds.

It is observed that under cutting conditions where the temperature effect is dominant, e.g. Al6061-T6 at cutting speed of 300 m/min, the starting point of the

nonlinearity is considerably different from the edge radius. This can be attributed to the material's temperature softening sensitivity exponent since a material with higher temperature softening sensitivity exponent will be affected to a greater extent by a given temperature change. For cutting conditions where multiple factors potentially contribute to the size effect in machining, the starting point of the nonlinearity may be affected by multiple factors such as the tool edge radius, the material length scale l and the temperature softening sensitivity exponent. Therefore, the following observations can be made from the above analysis,

- Under cutting conditions where the strain gradient effect is dominant, such as at low cutting speeds, small uncut chip thickness and negligible edge radius of the tool, the nonlinear increase in specific cutting energy starts at or near the material length scale l.
- Under cutting conditions where the temperature effect is dominant, such as at high cutting speeds, large uncut chip thickness and negligible tool edge radius, the starting point of the nonlinearity in the specific cutting energy may be affected largely by material's temperature softening sensitivity exponent.
- For certain cutting conditions, the starting point of nonlinearity may be affected by multiple factors such as size of the edge radius, the material length scale l and the temperature softening sensitivity exponent.

5.6 Summary

With the aim of understanding the contributions of different material strengthening factors to the size effect in micro-cutting, this chapter focused primarily on three factors: (i) strain gradient strengthening, (ii) the decrease in the secondary deformation zone cutting temperature, and (iii) edge radius. These factors were analyzed using a strain gradient plasticity based finite element model of orthogonal micro cutting that was verified experimentally in Chapter 4 for micro cutting of Al5083-H116, a material with a small strain-rate hardening exponent. The model was then used to simulate the size effect in micro cutting under conditions where the temperature and strain gradient effects are dominant. A cutting tool with finite edge radius was also incorporated in the simulation to examine the role of the edge radius on the size effect in specific cutting energy. The following conclusions can be drawn from this work:

- The strain gradient plasticity based model of micro cutting is able to capture the size effect in specific cutting energy for the aluminum alloy Al5083-H116 examined in this work.
- Strain gradient strengthening contributes significantly to the size-effect at low cutting speed (< 10 m/min) and small uncut chip thickness (< 10μm).
- Temperature dependence of flow stress plays a dominant role in causing size effect at relatively high cutting speeds (> 200 m/min) and large uncut chip thickness (> 20 μm). The size effect is caused by material strengthening due to a drop in the secondary shear zone temperature.
- Strain gradient strengthening is more dominant than the temperature effect at high cutting speed (> 200 m/min) and small uncut chip thickness (< 10μm). It

is therefore necessary to consider the strain gradient effect, especially for micron/sub-micron levels of uncut chip thickness.

- The radiused edge tool is able to capture a fraction of the size effect in micro-cutting. The edge radius affects the material deformation process and thus contributes to the size effect in two ways: (i) by changing the material flow pattern around the tool tip by expanding and widening the plastic shear zone, and (ii) causing higher energy dissipation due to increased frictional interaction at the tool-chip interface at smaller uncut chip thickness values.
- Under cutting conditions where the strain gradient effect is dominant, the nonlinear increase in specific cutting energy starts at the material length scale l. Under cutting conditions where the temperature effect is dominant, the starting point of nonlinearity is likely affected largely by material's temperature softening sensitivity exponent. For certain cutting conditions the starting point of the nonlinearity in specific cutting energy may be affected by multiple factors such as the size of tool edge radius, the material length scale l and the temperature softening sensitivity exponent.

CHAPTER 6

SURFACE ROUGHNESS IN MICRO-CUTTING

The previous chapter dealt with quantitative analysis of several material strengthening mechanisms that cause size effect in micro-cutting. In this chapter, a model-based approach is presented for the analysis of surface roughness generation in micro-cutting. Specifically, a model for predicting the surface roughness in micro-turning is presented in this chapter. The approach is based on a surface roughness model that takes into account the effect of plastic side flow, tool geometry, and process parameters. The roughness component associated with plastic side flow is modeled as a function of the material's rheological factor, which is a measure of its ductility. The model is calibrated and evaluated through a series of micro-turning experiments. The results show that the model can predict satisfactorily the surface roughness of a diamond turned surface at small feeds (< 20 μm/rev).

6.1 Surface Finish in Micro-Turning

In a conventional turning operation, the surface finish left on the machined part is produced by the cutting tool with a nose radius. The use of a tool with nose radius introduces several complications:

1. Ridges corresponding to the geometry of the tool nose and having a pitch equal to the axial feed are left behind on the finished surface.
2. The uncut chip thickness gradually goes to zero at the secondary cutting edge and this causes uncertainty in the geometry of the cut at the trailing

edge, since for a given edge sharpness there is minimum uncut chip thickness that will be removed [98].

3. The metal at the trailing edge of the tool is subjected to high normal stress and will flow to the side to relieve this stress [24]. This in turn produces a furrow that contributes to the roughness, particularly in the case of a soft, ductile metal.

In addition to these special roughness components, built up edge (BUE) roughness, roughness of the cutting edge, and roughness due to tool vibration may also be present.

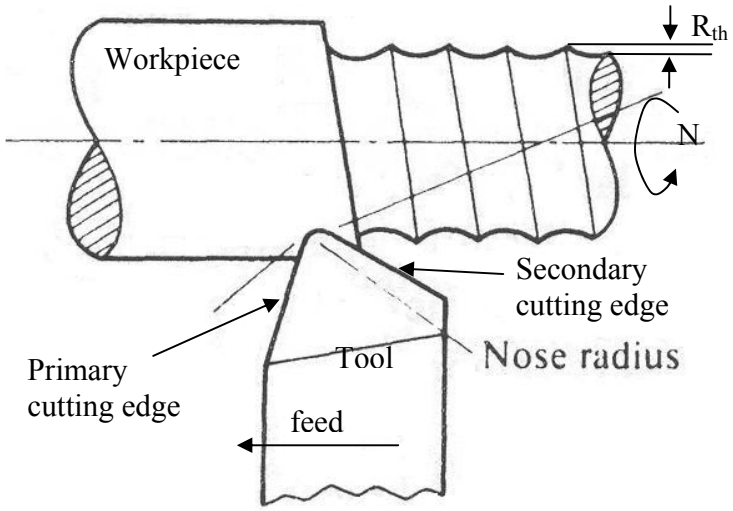

Figure 6.1. Illustration of turning operation showing primary and secondary cutting edges and characteristic wave-form left on the finished surface [24].

The first component of surface roughness is simply the geometric contribution of the tool nose geometry and the tool feed, as seen in Figure 6.1. This geometric component of surface roughness, also called kinematic or theoretical surface roughness, can be approximated by the following equation,

$$R_{th} \cong \frac{f^2}{8r_n} \tag{6.1}$$

where f is the feed and r_n is the tool nose radius.

The kinematic surface roughness is considered to be the main factor responsible for the tool marks left on the machined surface and is commonly used to estimate the theoretical surface roughness in conventional cutting at large feeds.

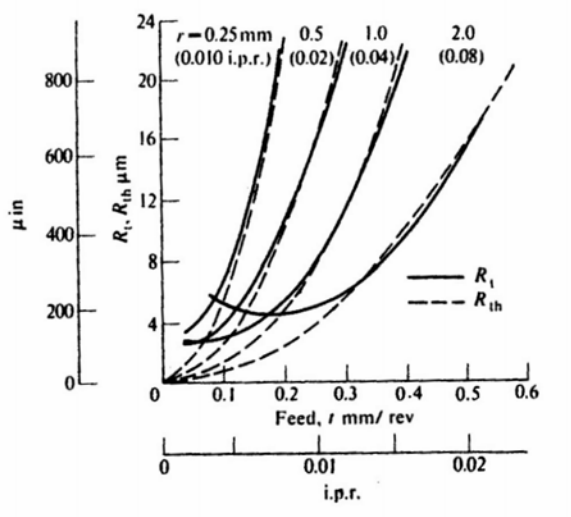

Figure 6.2. Comparison of measured and theoretical values of peak-to-valley roughness for tools of different nose radius at different feeds [24].

Figure 6.2 shows a plot of the measured and theoretical peak-to-valley roughness when using sharp tools of different nose radii to machine a steel at different feeds. The theoretical surface roughness is shown to yield satisfactory predictions of the surface roughness at large feeds. However, mismatch between the measured and theoretical surface roughness is observed in turning at small feeds.

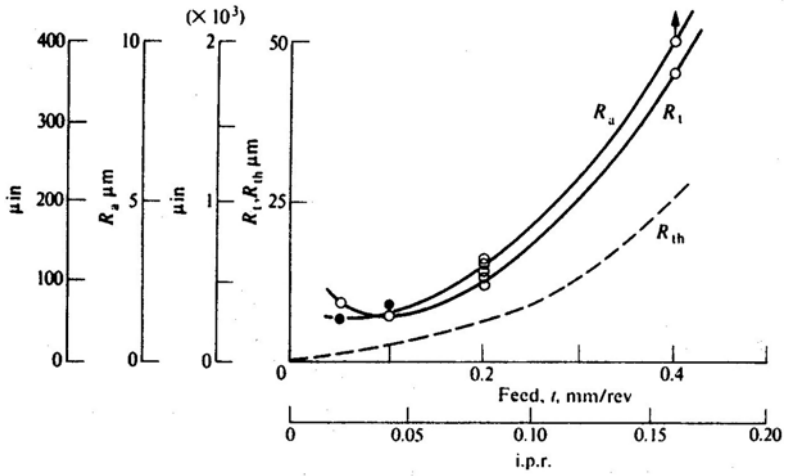

Figure 6.3. Comparison of measured and theoretical values of surface roughness (workpiece AISI 1045 steel, tool tungsten carbide) [24].

It can be seen from Figure 6.3 that the kinematic surface roughness under-predicts the measured surface roughness in micro-turning, especially at small feeds. It has also been observed that surface roughness in micro-turning decreases with feed, reaches a minimum, and then increases with further reduction in feed. This trend can be clearly seen in Figure 6.3 and in micro-turning of Al5083-H116 alloy used in the current study (see Figure 6.4).

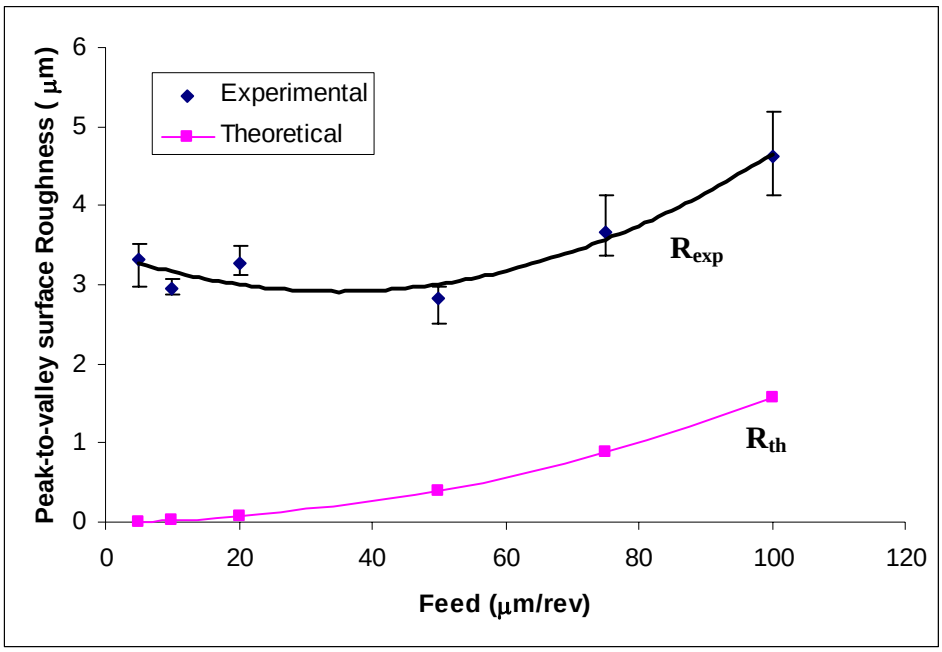

Figure 6.4. Comparison of measured and theoretical values of surface roughness for PCD diamond tool cutting of Al5083-H116 at 200 m/min.

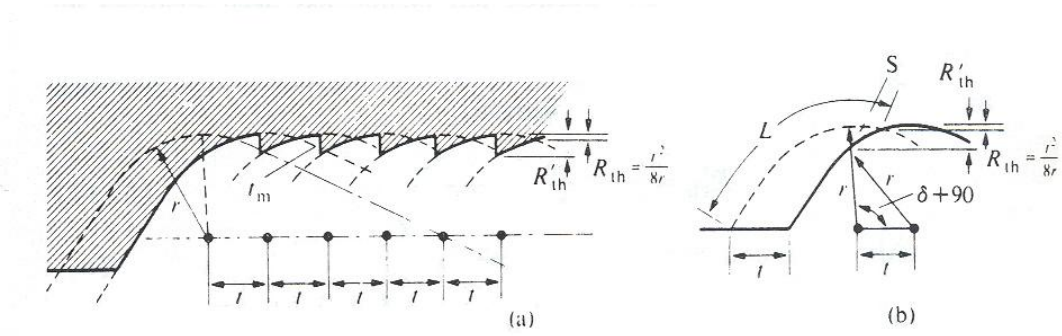

Figure 6.5. Illustration of surface roughness contribution of Spanzipfel [98].

Sokolowski [119] suggested that there is a minimum uncut chip thickness below which a chip will not form. When this occurs, rubbing takes place instead. Applying this idea to the secondary cutting edge of a turning tool, it is suggested that a small triangular portion of the material that should be removed is left behind. The portion left behind has

been analyzed by Brammertz [98] who called it a Spanzipfel. An additional purely geometric term (see Eq. 6.2) was proposed by Brammertz to supplement the kinematic surface roughness to account for the contribution of the Spanzipfel to the surface roughness in turning.

$$R_{th}' = \frac{f^2}{8r} + \frac{f_m}{2}\left(1 + \frac{rf_m}{2}\right) \tag{6.2}$$

Grzesik [99] proposed a revised model based on Brammertz's work to account for the increasing trend in surface roughness below a certain feed by introducing the minimum uncut chip thickness as a function of the tool feed.

However, as pointed out by Shaw [24, pp. 519], the Spanzipfel will be plastically deformed and made smaller as it comes into contact with the clearance surface of the tool. Consequently, it is not likely to completely account for the observed trend at small feeds.

Sata [120] has studied the influence of material side flow on surface finish and has found that this component of roughness is zero for a brittle material such as brass, but may contribute up to 6 μm to the roughness when an alloy steel is machined.

Shaw [24] also indicated that plastic side flow is most significant at very small feeds and could be partly responsible for the rise in surface roughness after reaching a minimum for feeds less than a certain value. According to Shaw, this is due in part to the fact that the specific cutting energy, and hence the mean stress on the tool face, increases rapidly as the feed decreases. This in turn will cause more plastic side flow along the secondary cutting edge. The furrow or ridge that is thus formed because of material side flow will add to the discrepancy between the measured and theoretical values of surface roughness. Although Shaw [24, pp. 516] forwarded this as a likely explanation, he did not

demonstrate its validity through modeling and analysis. The present paper attempts to do this explicitly.

Therefore, in this study three roughness components, the kinematic or theoretical surface roughness, roughness of the cutting edge and the roughness associated with plastic side flow are considered to be the main factors that contribute to the surface finish at very small feeds. In particular, the surface roughening associated with plastic side flow is analyzed and modeled quantitatively.

6.2 Plastic Side Flow Induced Surface Roughness

The material around the cutting edge is subjected to sufficiently high pressure to cause the material to flow to the side (see Figure 6.6). As shown schematically in Figure 6.7, the solid curve shows the profile left behind in the absence of side flow while the dotted curve shows the profile with side flow. It is evident from Figure 6.7 that the peak-to-valley roughness is larger when side flow is present.

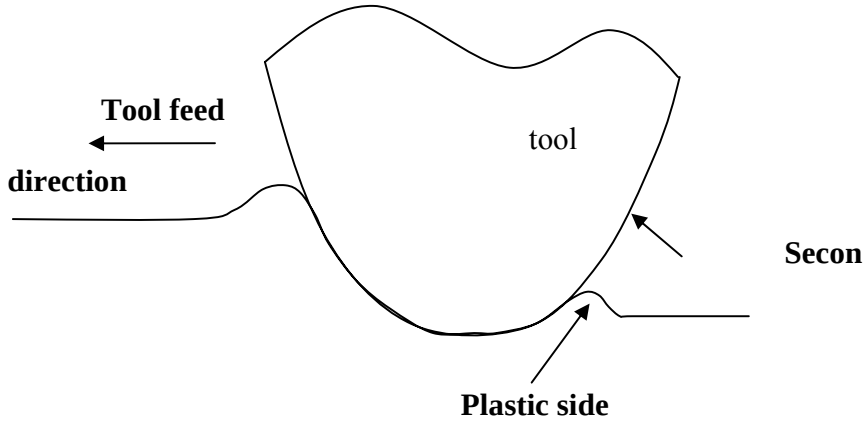

Figure 6.6. Illustration of plastic side flow generated by secondary cutting edge.

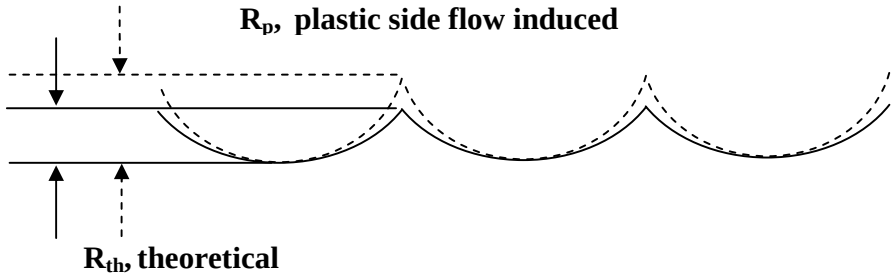

Figure 6.7. Surface profile generated by tool with nose radius, with and without plastic side flow.

Since the material pile up height at the trailing edge of the tool due to plastic side flow is dependent on the strength and ductility of the material, it is very likely that the increasing trend in surface roughness at low feeds, after reaching a minimum, is linked to the size effect in micro-turning. It is well-known that metals strengthen remarkably at the micron scale of deformation [19-23]. Size effect in micro-cutting shows that the specific cutting energy increases nonlinearly as the uncut chip thickness is decreased. This increase in specific cutting energy can arise from increase in material strength due to large strain gradient, temperature and strain rate effects. If the material directly in front of the tool face is strengthened much more than the material on the side, more plastic side flow will occur and the roughness due to plastic side flow will be greater. Therefore, the strain gradient based finite element model of micro-cutting developed and validated in chapter 3, 4 will be used to provide an estimate of the average flow stress in the shear zone for use in the proposed model of surface roughness due to plastic side flow.

6.3 Proposed Surface Roughness Model

The proposed surface roughness model is based on mechanical analysis of a scratch test performed on metals. The scratch test is used mainly to study the mechanical properties of materials near their surface. The scratch hardness and surface deformation depend in particular on the rheology of the material, the friction at the interface and the indenter geometry.

The behavior in a scratch test depends on the rheological factor, x [121,122]:

$$x = \frac{E \cot \theta}{\sigma_y} \tag{6.3}$$

where θ is the semi-apical angle of the indenter, E is the Young's modulus and σ_y is the yield stress of the material.

The rheological factor represents the ratio of the plastic strain caused by the indenter ($\varepsilon_p \sim cot\ \theta$) and the portion of the elastic strain ($\varepsilon_e \sim \sigma_o/E$).

Jardret et al. [121] have studied scratch resistance of elastoplastic materials such as metals and polymers. They have performed experiments with a Berkovich indenter and have measured the scratch morphology. They defined a depth h_a, which is measured from the bottom of the scratch groove to the top of the lateral pile-up (see Figure 6.8), and is given by the following relation:

$$\frac{h_a}{h} = 0.3084 \ln x + 0.3233 \tag{6.4}$$

where h is the contact depth.

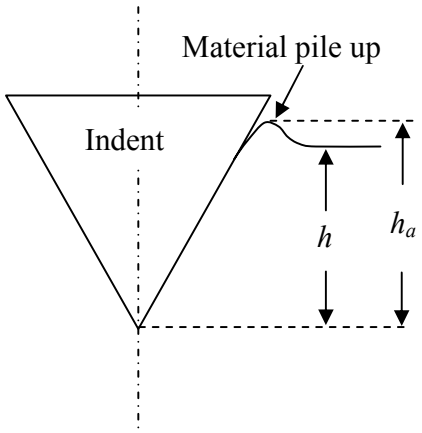

Figure 6.8. Illustration of contact depth h and actual contact depth h_a in a scratch test.

Bucaille et al. [122] performed a three dimensional finite element analysis of scratching on elastic and perfectly plastic materials and obtained a similar form of equation with different coefficients.

Since there exist similarities between a cutting test and the scratch test, the general form of Eq. (6.4) can be used to represent the roughness due to plastic side flow as a function of the rheological factor x. However, the tool used in turning has a different geometry from the indenter used in a scratch test. Also, in a turning test, the tool is fed in a direction different from the cutting direction. Therefore, coefficients k_1 and k_2 in Eq. (6.5) need to be calibrated via actual turning tests for a range of conditions.

$$R_p = k_1 \ln x + k_2 \tag{6.5}$$

$$x = \frac{E \cot \theta}{\overline{\sigma}_y e} \tag{6.6}$$

In the definition of the rheological factor x in Eq. (6.6), an average flow stress $\overline{\sigma}_y$ which accounts for the hardening effect replaces the constant flow stress σ_y used for a perfect plastic material in Eq. (6.3). An additional variable e is introduced to account for

the difference in material strength between the material in the front and material at either side of the tool. The variable e is defined as the ratio of the average flow stress with strain gradient strengthening to the average flow stress without strain gradient strengthening.

The revised model for surface roughness prediction in micro-turning consists of three components, kinematic surface roughness R_{th}, roughness associated with plastic side flow R_p and roughness of the cutting edge R_{edge}:

$$R_{total} = R_{th} + R_p + \lfloor R_{edge} \rfloor \tag{6.7}$$

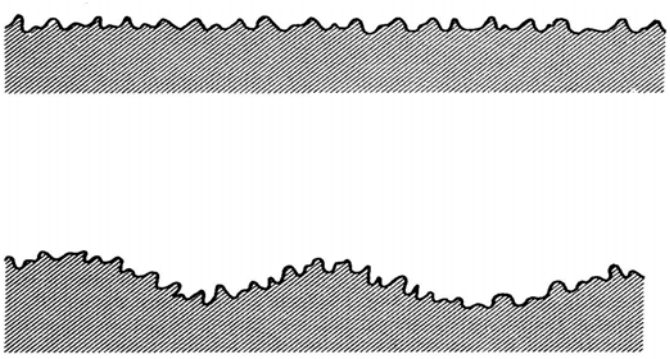

Figure 6.9. Surface roughness due to a non-smooth cutting edge.

Figure 6.9 shows the surface roughness component due to the roughness of the cutting edge R_{edge} and how it contributes to the overall peak-to-valley roughness height. It is seen that the surface profile within each trough is caused directly by the non-smooth cutting edge. However, it is obvious that this component has little effect on the overall peak-to-valley surface roughness at conventional feeds. Its contribution to the overall peak-to-valley surface roughness becomes important only when the feed is decreased to a value so low that the roughness of the cutting edge is comparable to overall peak-to-

valley surface roughness. Thus, in Eq. (6.7) the term R_{edge} is inside a square bracket, which means that its inclusion in the total surface roughness is subject to certain conditions.

6.4 Model Calibration

6.4.1 Experimental Goal

The objective of the calibration experiments is to establish a quantitative relationship between the peak-to-valley surface roughness induced by plastic side flow and the rheological factor x for aluminum alloy Al5083 H-116, the strain-rate insensitive material used in this study. This implies determination of the constants k_1 and k_2 in Eq. (6.5).

6.4.2 Experimental Design and Procedure

Turning tests were conducted on a Hardinge Conquest T42SP lathe. Polycrystalline diamond (PCD) tools (TP432, grade KD100) with 800 μm nose radius and toolholder CTGPR-164D were used for turning Al5083-H116. The toolholder together with the insert gave a side rake angle of 5 degrees, back rake angle of 0 degree, side cutting edge angle of 0 degree and a clearance angle of 11 degrees.

A grooving test was initially conducted at a large feed of 2 mm/rev and the material pile up height at the two edges of the groove was measured using a white light interferometer (Zygo®). It was found that the height of material pile up at the two edges are comparable and therefore the material pile up height at smaller feeds was measured at the front edge instead of the trailing edge due to ease of measurement. Figure 6.10 shows

the surface profile of the material pile up near the edge of the groove at feed of 150 µm/rev.

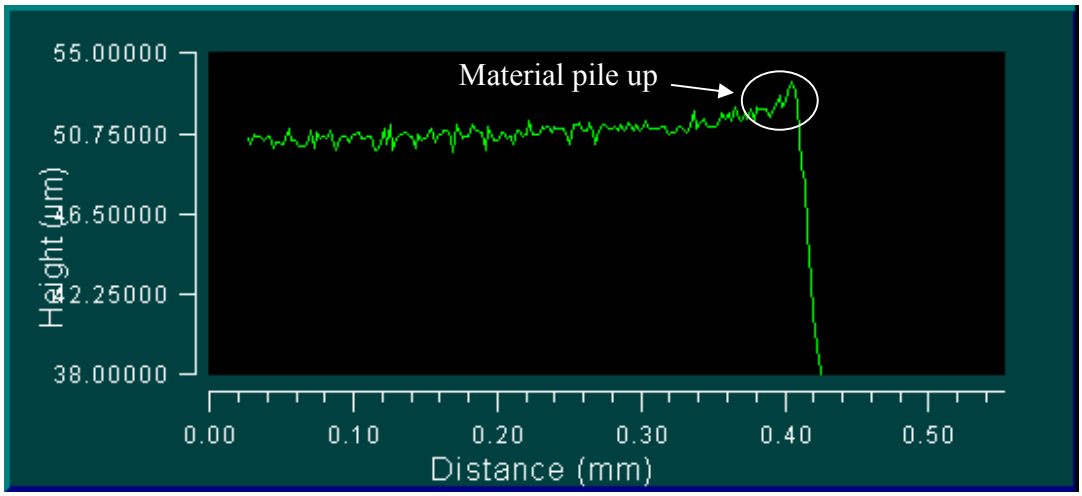

Figure 6.10. Zygo measurement of material pile up height at the edge of groove for feed of 150 µm/rev.

Longitudinal turning tests were performed on a solid round bar at a cutting speed of 200 m/min for four levels of feed, as listed in Table 6.1. The cutting speed of 200 m/min was chosen to ensure that the surface finish is not affected by possible built up edge formation during cutting. Three replications of each test condition were performed. The responses measured in the experiments consisted of the material pile-up height at the leading edge of the groove, cut forces and the chip width and thickness. The thickness and width of the deformed chips were measured using a microscope and a micrometer, respectively.

Table 6.1. Factor and factor levels for R_p model calibration tests.

Feed (μm/rev)	30	60	100	150
Depth of cut (μm)	100			
Speed (m/min)	200			

The effect of depth of cut on material pile up height was examined by conducting turning tests at two different depths of cut, 50 μm and 150 μm. It was observed that the material pile up height is only slightly affected by the depth of cut within the range examined in this work. Thus, all calibration tests were conducted at 100 μm depth of cut. Note that the material pile up height is affected indirectly by the feed and depth of cut via the average flow stress $\overline{\sigma}_y$. It is found that the material pile up height is significantly affected by the feed, but only slightly affected by the depth of cut within the range examined.

6.4.3 R_p Model Fitting

Table 6.2 shows the cutting forces and chip geometry obtained from model calibration tests. These data were used to estimate the rheological factor x using an equivalent orthogonal cutting model. For this purpose, the three dimensional cutting conditions in turning were converted to their equivalent orthogonal cutting conditions. This was done via the use of an equivalent orthogonal uncut chip thickness. The determination of the equivalent uncut chip thickness should nominally consider the actual shape of undeformed chip cross-section in turning. It should be noted that the cross section of the undeformed chip in turning is not rectangular as in orthogonal cutting. Since the plastic deformation near the region of the undeformed chip cross section where

plastic side flow occurs is of primary interest, the equivalent uncut chip thickness in orthogonal cutting was assumed to be equal to the feed used in the turning tests.

Table 6.2. Measured cutting forces and chip geometry in calibration tests.

Feed (μm/rev)	Cutting force, F_c (N)	Thrust force, F_t (N)	Chip thickness (μm)	Chip width (μm)
30	8.18	9.04	51	270
60	10.67	8.63	69	345
100	13.18	10.66	91	405
150	15.69	12.69	94	645

In order to evaluate the material rheological factor *x*, the average flow stress within the shear zone needs to be determined. The procedure to calculate the average flow stress within the shear zone is described by Eqs. (6.8)-(6.14). Since the inclination angle is calculated to be approximately 0 degree and the third direction (axial direction) force component signal was observed to be negligible, reasonable approximation of the average shear stress in three dimensional turning can be obtained by using orthogonal cutting equations with nominal angles.

The inclination angle i and normal rake angle α_n can be found from the known angles given earlier using Eqs. (6.8)-(6.9),

$$i = \tan^{-1}\left(\tan\alpha_b \cos C_s - \tan\alpha_s \sin C_s\right) \tag{6.8}$$

$$\alpha_n = \tan^{-1}\left[\cos i(\tan\alpha_s \cos C_s + \tan\alpha_b \sin C_s)\right] \tag{6.9}$$

where α_b is the back rake angle, α_s is the side rake angle, C_s is the side cutting edge angle. The inclination angle and normal rake angle are calculated to be approximately 0 degree and 5 degrees, respectively.

To estimate the average shear stress in the primary shear zone, the normal shear angle was calculated from the following equation,

$$\varphi_n = \tan^{-1}\left(\frac{r\cos\alpha_n}{1 - r\sin\alpha_n}\right) \tag{6.10}$$

where r is the cutting ratio and is defined as,

$$r = \frac{t}{t_c} \tag{6.11}$$

and t is the uncut chip thickness and t_c the deformed chip thickness.

The normal friction angle β_n can be obtained from

$$\beta_n = \tan^{-1}\left(\frac{F_t + F_c\tan\alpha_n}{F_c - F_t\tan\alpha_n}\right) \tag{6.12}$$

The mean shear stress was estimated using the following equation:

$$\bar{\tau} = \frac{F_c\cos(\beta_n + \varphi_n - \alpha_n)\sin\varphi_n}{\cos(\beta_n - \alpha_n)tw} \tag{6.13}$$

where w is the width of the chip.

Finally, the average flow stress was computed from

$$\bar{\sigma}_y = \bar{\tau} * \sqrt{3} \tag{6.14}$$

The plastic side flow induced surface roughness R_p at feeds of 30, 60, 100 and 150 μm/rev were measured and are listed in Table 6.3. The rheological factor x can now be calculated using Eq. (6.14) and Eq. (6.6) and its values are given in Table 6.3.

Table 6.3. Rheological factor x and plastic side flow induced surface roughness R_p used for calibration.

Rheological factor, x	R_p (μm)
4.15E+02	2.2
4.25E+02	2.5
5.17E+02	3.5
7.14E+02	4.63

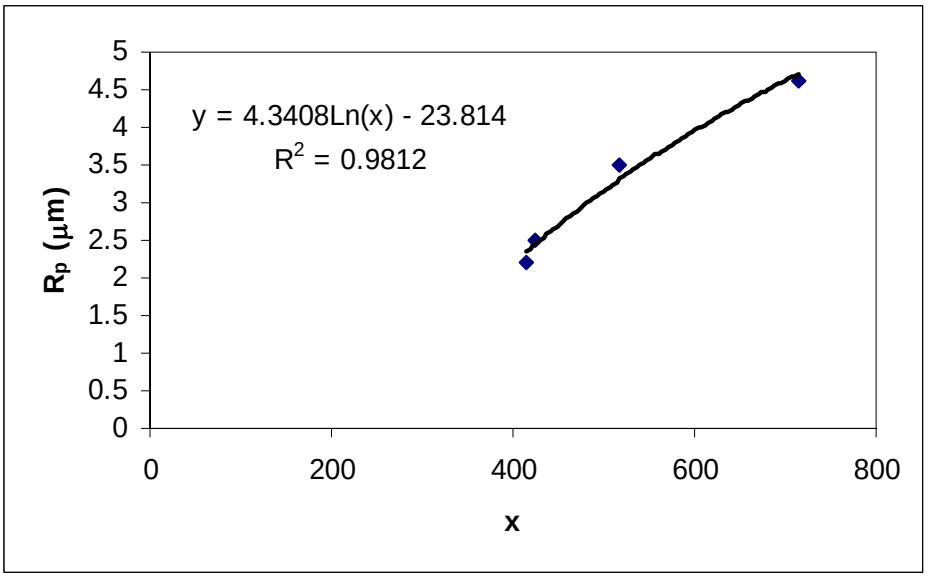

Figure 6.11. Determination of coefficients k_1 and k_2.

The data in Table 6.3 was fitted using Eq. (6.5) and the coefficients k_1 and k_2 were found to be 4.3408 and -23.814, respectively. The roughness R_p due to plastic side flow can now be established as a function of the material rheological factor x by the following equation,

$$R_p = 4.3408\ln(x) - 23.814 \quad (\mu m) \tag{6.15}$$

6.5 Effect of Cutting Edge Roughness, R_{edge}

A turning test was conducted at zero feed and a speed of 200 m/min using a fresh PCD tool to examine the roughness produced by a non-smooth cutting edge. This roughness component was measured by scanning the surface profile within each groove using the Zygo white light interferometer and the results show that the average roughness due to a non-smooth cutting edge is less than 2 μm. Therefore, this roughness component does not contribute significantly to the overall peak-to-valley roughness in the current study and will not be included in the total surface roughness calculation.

6.6 Surface Roughness Prediction

Micro-turning tests for surface roughness model validation were conducted on Al5083-H116 over a range of feed from 5 to 100 μm/rev. Cutting conditions used are given in Table 6.4 and the experimental measurements of the peak-to-valley surface roughness are plotted against theoretical surface roughness in Figure 6.12. Note that the feeds used in the validation tests are different from the R_p model calibration tests.

Table 6.4. Factor and factor levels for Al5083-H116.

Feed (μm/rev)	5	10	20	50	75	100
Depth of cut (μm)	100					
Speed (m/min)	200					

The surface roughness model prediction (Eq. (6.7)) was compared against the experimental measurement of surface roughness in micro-turning. First, the average flow stress with and without strain gradient strengthening for each feed was obtained from

orthogonal cutting simulations using the finite element model of orthogonal micro-cutting presented in chapter 3 and using the equivalent uncut chip thickness i.e. the feed. The average flow stresses σ' (with strain gradient strengthening) and σ'' (without strain gradient strengthening) and their ratio e are computed and listed in Table 6.5.

Table 6.5. Average flow stress and surface roughness prediction for Al5083 H-116.

Feed (μm)	σ' (MPa)	σ'' (MPa)	e	R_{total}' (μm)	R_{total}'' (μm)
5	375	295.5	0.79	2.30	3.34
10	358.8	292.7	0.82	2.35	3.23
20	339.5	290	0.85	2.39	3.07
50	310.5	285	0.92	2.46	2.83
75	297.45	280	0.94	2.54	2.80
100	265	260	0.98	2.86	2.94

The total surface roughness R_{total}' in Table 6.5 was calculated from the average flow stress without strain gradient strengthening (e is assumed to be 1 in this case). The total surface roughness R_{total}'' was calculated from the average flow stress with strain gradient strengthening and the e values listed in Table 6.5.

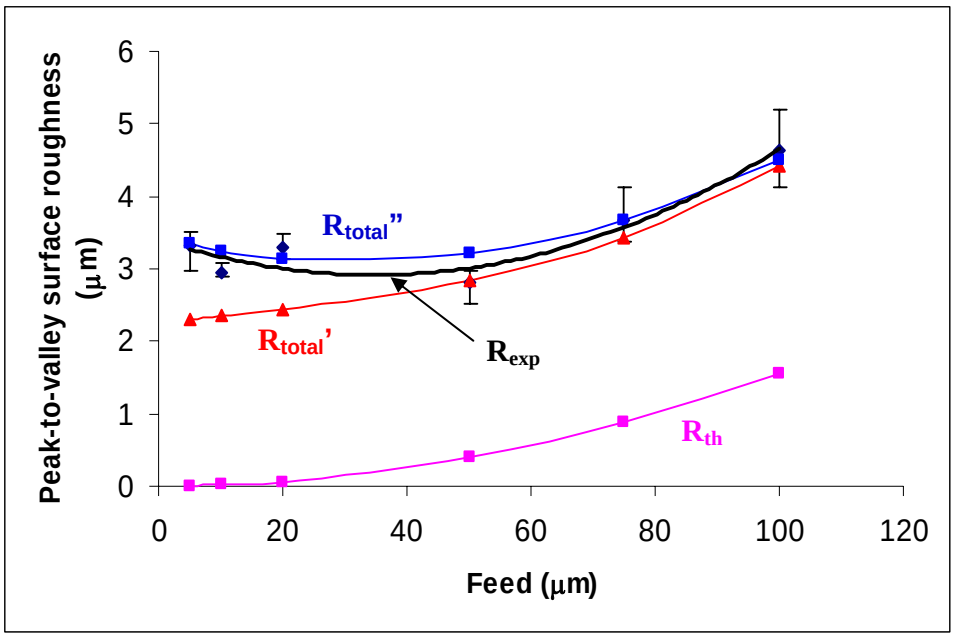

Figure 6.12. Surface roughness prediction using the developed model.

The surface roughness predictions R_{total}' and R_{total}'' are plotted in Figure 6.12 and compared with the measured surface roughness R_{exp} and the theoretical peak-to-valley surface roughness R_{th}. It can be seen that for feeds greater than 50 μm/rev, both R_{total}' and R_{total}'' yield much better predictions than the theoretical surface roughness prediction since the additional roughness associated with plastic side flow is considered. However, for feeds less than 50 μm/rev, R_{total}' fails to predict the increasing trend when the feed is decreased further. The prediction of R_{total}", which considers strain gradient strengthening of material in front of the tool face, is seen to capture this trend well. Therefore, it can be concluded that the increasing trend in surface roughness at low feeds is related to the size effect in micro-cutting arising from material strengthening due to strain gradient effects (for Al5083-H116). This confirms Shaw's earlier hypothesis [24, pp. 516]. To obtain

accurate predictions of the surface roughness in micro-cutting, strain gradient strengthening is important and should be considered in the model.

Table 6.6. Comparison of predicted versus measured surface roughness in micro-turning.

Feed (μm)	R_{exp} (μm)	R_{th} (μm)	R_{th} error	R_{total}" (μm)	R_{total}" error
5	3.32	0.004	0.73%	3.34	-99.88%
10	2.95	0.02	10.15%	3.24	-99.47%
20	3.28	0.06	-4.57%	3.13	-98.10%
50	2.82	0.39	14.14%	3.22	-86.17%
75	3.67	0.88	0.12%	3.68	-76.08%
100	4.63	1.56	-2.68%	4.50	-66.24%

Table 6.6 shows the surface roughness predicted by the theoretical surface roughness equation and the developed model. It can be seen that the theoretical surface roughness is very poor and the percentage error is more than 66% for all feeds. In contrast, significant improvement in roughness prediction is achieved using the surface roughness model developed in this paper. It can be seen that the percentage error of the prediction by the developed model is less than 15% for all feeds.

6.7 Summary

This chapter presented a model based approach for predicting the surface roughness in single point micro-turning of Al5083-H116. The approach is based on a surface roughness model that takes into account the effect of plastic side flow, tool geometry, and process parameters. The model combined more accurate information of average flow stress of Al5083-H116 at the micron length scale from the previous strain gradient based finite element model and was evaluated through a series of turning experiments. The results show that the model can predict well the surface roughness of a diamond turned surface at small feeds. Therefore, the following conclusions can be drawn:

- It is shown that most of the discrepancy between the theoretical surface roughness and measured surface roughness in micro-turning is due to the additional surface roughening caused by plastic side flow.
- The increase in roughness after reaching a minimum can be attributed to increased side flow caused by the strain-gradient induced strengthening of the material directly ahead of the tool.
- Significant improvement in roughness prediction is achieved using the developed surface roughness model. The percentage error of the prediction using the developed model is less than 15% for all feeds investigated.

CHAPTER 7

CONCLUSIONS AND RECOMMENDATIONS

7.1 Conclusions

A finite element model that incorporates strain gradient plasticity in process modeling of micro scale orthogonal cutting is developed in this thesis. The role of strain gradient strengthening on size effect and its relative contribution to size effect compared to other factors, such as temperature and edge radius, are analyzed. In addition, a model-based approach is developed for prediction of the surface roughness in the micro-turning process. Better physical understanding of material and cutting parameter interactions in micro-cutting is achieved through this modeling effort. The following paragraphs summarize the key findings of this work.

7.1.1 Size Effect Analysis in Micro-Cutting

- Size effect cannot be explained satisfactorily by a single mechanism. Multiple mechanisms can be responsible for size effect in micro-cutting.
- A constitutive model based on Tayor-based nonlocal theory of plasticity was developed to accurately represent the material strengthening behavior of Al5083-H116 at micron/submicron level. A fully coupled thermo-mechanical Finite Element model created in the ABAQUS®/Standard software was used to simulate orthogonal micro-cutting of Al5083-H116 using the developed material model.
- The simulation procedure and the developed material model were validated successfully by comparing predicted machining forces with those determined

experimentally. An absolute average percentage error of 4.25% for cutting force and an average percentage error of 23.21% for thrust force are obtained at a cutting speed of 200 m/min. An absolute average percentage error of 9.6% for cutting force and an absolute average percentage error of 22.2% for thrust force are obtained for orthogonal cutting tests at a cutting speed of 10 m/min.

- The strain gradient plasticity based model of orthogonal micro-cutting is able to capture the size effect in specific cutting energy for the aluminum alloy Al5083-H116 examined in this work.
- Strain gradient strengthening contributes significantly to the size-effect at low cutting speed (< 10 m/min) and small uncut chip thickness (< 10μm).
- Temperature dependence of flow stress plays a dominant role in causing size effect at relatively high cutting speeds (> 200 m/min) and large uncut chip thickness (> 20 μm). The size effect is caused by material strengthening due to a drop in the secondary shear zone temperature.
- Strain gradient strengthening is more dominant than the temperature effect at high cutting speed (> 200 m/min) and small uncut chip thickness (< 10μm). It is therefore necessary to consider the strain gradient effect, especially for micron/sub-micron levels of uncut chip thickness.
- The radiused edge tool is able to capture a fraction of the size effect in micro-cutting. The edge radius affects the material deformation process and thus contributes to the size effect in two ways: (i) by changing the material flow pattern around the tool tip by expanding and widening the plastic shear zone,

and (ii) causing higher energy dissipation due to increased frictional interaction at the tool-chip interface at smaller uncut chip thickness values.

- Under cutting conditions where the strain gradient effect is dominant, the nonlinear increase in specific cutting energy starts at the material length scale l. Under cutting conditions where the temperature effect is dominant, the starting point of nonlinearity is likely affected largely by material's temperature softening sensitivity exponent. For certain cutting conditions the starting point of the nonlinearity in specific cutting energy may be affected by multiple factors such as the size of tool edge radius, the material length scale l and the temperature softening sensitivity exponent.

7.1.2 Surface Roughness Prediction in Micro-Turning of Al5083-H116

- It is shown that most of the discrepancy between the theoretical surface roughness and measured surface roughness in micro-turning is due to the additional surface roughening caused by plastic side flow.
- The increase in roughness after reaching a minimum can be attributed to increased side flow caused by the strain-gradient induced strengthening of the material directly ahead of the tool.
- Significant improvement in roughness prediction is achieved using the developed surface roughness model. The percentage error of the prediction using the developed model is less than 15% for all feeds investigated.

7.2 Recommendations for Future Work

7.2.1 Modeling Size Effect in Micro-Cutting

- In order to examine the strain rate hardening and its effect on size effect in micro-cutting, a finite element model with constitutive model including strain rate hardening component needs to be developed. This will provide a complete model that can be used for a thorough analysis on all material strengthening mechanisms and their contribution to size effect.
- Frictional interaction at the tool-chip interface is modeled with Coulomb friction using a constant friction coefficient, which leads to larger prediction errors in the thrust force at small uncut chip thickness. It is observed that the friction coefficient has an increasing trend with the decrease in uncut chip thickness. Thus, the friction characteristic in microscale metal cutting needs to be investigated.
- The use of work material flow stress data for Al5083-H116 obtained from hot torsion test in micro-cutting leads a certain degree of inaccuracy in the solution. Independent material tests should be performed to obtain flow stress of Al5083-H116 in the range of high temperature and high strain rate.
- The validation procedure used machining forces as the only measure of accuracy of the developed finite element model. This should be expanded to include other metrics such as chip thickness, cutting temperatures and strains generated in the machined surface.

- The uncut chip thickness in micro-cutting approaches the grain size of the material and therefore the effect of grain size and micro-structural influence on the flow stress needs to be investigated.

7.2.2 Prediction of Surface Roughness in Micro-Turning

- In the present work, the average flow stress information is obtained from the equivalent orthogonal cutting condition. The strain gradient based finite element model should be extended to three-dimensions to provide a more accurate prediction of the material strength in oblique cutting.

APPENDIX A

Table A.1. Cutting forces and specific cutting energy for radiused edge tool with 20 μm edge radius.

Uncut chip thickness t (μm)	Cutting force, F_c (N)	Thrust force, F_t (N)	Specific cutting energy, SF_c (MPa)	Specific thrust energy, SF_t (MPa)	t/r
7.5	9.9	10.24	1320.00	1365.33	0.375
10	11.4	10.8	1140.00	1080.00	0.5
20	16.1	10.5	805.00	525.00	1
50	30.3	11	606.00	220.00	2.5
75	42.5	11.2	566.67	149.33	3.75

Table A.2. Cutting forces and specific cutting energy for radiused edge tool with 5 μm edge radius.

Uncut chip thickness, t (μm)	Cutting force, F_c (N)	Thrust force, F_t (N)	Specific cutting energy, SF_c (MPa)	Specific thrust energy, SF_t (MPa)	t/r
3	3.55	2.75	1183.33	916.67	0.6
5	4.83	2.86	966.00	572.00	1
7.5	6.25	2.9	833.33	386.67	1.5
10	7.75	3	775.00	300.00	2
20	13.1	2.9	655.00	145.00	4

APPENDIX B

Table B.1. Cutting forces from orthogonal cutting tests at cutting speed of 200 m/min.

Uncut chip thickness (μm)	Cutting Force replication I (N)	Cutting Force replication II (N)	Cutting Force replication III (N)	Mean Cutting force (N)	Standard deviation (N)
20	20.0	21.0	23.1	21.4	1.6
50	39.6	39.4	39.4	39.5	0.1
75	53.5	52.0	53.8	53.1	0.9
100	67.2	69.0	65.5	67.2	1.7
150	101.9	105.8	104.3	104.0	1.9
200	137.9	133.3	129.1	133.4	4.4

Table B.2. Thrust forces from orthogonal cutting tests at speed of 200 m/min.

Uncut chip thickness (μm)	Thrust Force replication I (N)	Thrust Force replication II (N)	Thrust Force replication III (N)	Mean Thrust force (N)	Standard deviation (N)
20	10.9	10.7	12.5	11.4	1.0
50	15.0	15.5	16.0	15.5	0.5
75	19.0	19.4	20.9	19.8	1.0
100	25.9	26.2	24.9	25.7	0.7
150	42.4	47.1	48.5	46.0	3.2
200	55.4	54.0	53.0	54.1	1.2

Table B.3. Force data from orthogonal cutting tests at 10 m/min.

Uncut chip thickness (μm)	Cutting Force F_c (N)	Thrust Force F_t (N)
0.5	0.8195	0.2785
0.5	0.9366	0.3621
0.5	0.9666	0.4092
0.5	1.0698	0.4203
0.5	1.0614	0.4011
1	1.2495	0.4415
1	1.2846	0.3864
1	1.6426	0.3821
1	1.464	0.4307
1	1.6164	0.3733
2	2.939	0.5547
2	2.3457	0.3597
2	2.3031	0.3986
2	2.3898	0.4398
2	2.3573	0.4852
5	5.2325	0.9926
5	5.1497	0.9667
5	5.2845	0.9937
5	5.4666	1.1752
5	5.4246	1.0989
7.5	7.7623	1.5619
7.5	7.6515	1.552
7.5	7.6347	1.5232
7.5	7.6305	1.4933
7.5	7.8616	1.6678
10	9.7068	1.8961
10	9.7143	1.901
10	9.6915	1.8443
10	9.6997	1.8553
10	10.0352	2.0073

Table B.4. Surface roughness measurement at feed of 100 μm/rev, Depth of cut of 100 μm and cutting speed of 200 m/min (all units in μm).

feed 100 μm/rev						
Point 1	Pv	6.725	Rms	0.869	Ra	0.692
L1	4.471		0.859		0.692	
L2	4.069		0.82		0.663	
L3	4.334		0.908		0.724	
L4	5.055		0.895		0.723	
L5	4.148		0.805		0.658	
average	**4.4154**		**0.8574**		**0.692**	
Point 2	Pv	6.343	Rms	0.795	Ra	0.653
L1	4.014		0.798		0.653	
L2	4.278		0.79		0.662	
L3	4.143		0.762		0.623	
L4	3.738		0.732		0.602	
L5	4.431		0.783		0.642	
average	**4.1208**		**0.773**		**0.6364**	
Point 3	Pv	7.262	Rms	0.871	Ra	0.698
L1	4.598		0.851		0.702	
L2	4.489		0.787		0.64	
L3	4.7		0.842		0.69	
L4	5.03		0.906		0.721	
L5	5.157		0.862		0.675	
average	**4.7948**		**0.8496**		**0.6856**	
Point 4	Pv	7.569	Rms	0.949	Ra	0.752
L1	5.149		0.928		0.737	
L2	5.009		0.928		0.739	
L3	5.897		0.977		0.79	
L4	4.798		0.896		0.71	
L5	5.069		0.953		0.758	
average	**5.1844**		**0.9364**		**0.7468**	
Average	**4.62885**		**0.8541**		**0.6902**	

Table B.5. Surface roughness measurement at feed of 75 μm/rev, Depth of cut of 100 μm and cutting speed of 200 m/min (all units in μm).

feed 75 μm/rev						
Point 1	Pv	6.106	Rms	0.644	Ra	0.498
L1	3.485		0.613		0.471	
L2	3.373		0.565		0.441	
L3	3.797		0.628		0.484	
L4	3.739		0.684		0.542	
L5	3.822		0.648		0.499	
average	**3.6432**		**0.6276**		**0.4874**	
Point 2	Pv	6.24	Rms	0.587	Ra	0.457
L1	3.604		0.571		0.439	
L2	3.475		0.568		0.454	
L3	3.069		0.547		0.44	
L4	3.153		0.521		0.422	
L5	3.531		0.619		0.477	
average	**3.3664**		**0.5652**		**0.4464**	
Point 3	Pv	6.185	Rms	0.59	Ra	0.459
L1	3.968		0.618		0.469	
L2	3.302		0.577		0.453	
L3	4.279		0.629		0.479	
L4	3.205		0.586		0.467	
L5	3.015		0.543		0.433	
average	**3.5538**		**0.5906**		**0.4602**	
Point 4	Pv	5.906	Rms	0.649	Ra	0.497
L1	4.206		0.651		0.491	
L2	3.986		0.628		0.49	
L3	4.41		0.613		0.467	
L4	3.974		0.606		0.483	
L5	4.102		0.627		0.503	
average	**4.1356**		**0.625**		**0.4868**	
Average	**3.67475**		**0.6021**		**0.4702**	

Table B.6. Surface roughness measurement at feed of 50 μm/rev, Depth of cut of 100 μm and cutting speed of 200 m/min (all units in μm).

feed 50 μm/rev						
Point 1	Pv	5.325	Rms	0.417	Ra	0.321
L1	2.581		0.39		0.297	
L2	2.868		0.402		0.318	
L3	2.867		0.419		0.333	
L4	3.067		0.406		0.312	
L5	2.922		0.366		0.282	
average	**2.861**		**0.3966**		**0.3084**	
Point 2	Pv	4.687	Rms	0.399	Ra	0.305
L1	2.373		0.385		0.299	
L2	2.563		0.398		0.318	
L3	2.53		0.388		0.304	
L4	2.355		0.337		0.259	
L5	2.728		0.385		0.292	
average	**2.5098**		**0.3786**		**0.2944**	
Point 3	Pv	6.309	Rms	0.48	Ra	0.361
L1	3.746		0.528		0.378	
L2	3.117		0.439		0.341	
L3	2.543		0.388		0.305	
L4	2.927		0.473		0.373	
L5	2.424		0.441		0.343	
average	**2.9514**		**0.4538**		**0.348**	
Point 4	Pv	0.605	Rms	0.433	Ra	0.331
L1	3.14		0.444		0.324	
L2	3.312		0.413		0.32	
L3	2.642		0.385		0.296	
L4	2.88		0.427		0.321	
L5	2.905		0.433		0.332	
average	**2.9758**		**0.4204**		**0.3186**	
Average	**2.8245**		**0.41235**		**0.31735**	

Table B.7. Surface roughness measurement at feed of 20 μm/rev, Depth of cut of 100 μm and cutting speed of 200 m/min (all units in μm).

feed 20 μm/rev						
Point 1	Pv	5.447	Rms	0.492	Ra	0.359
L1	3.626		0.443		0.333	
L2	3.073		0.451		0.34	
L3	3.616		0.504		0.357	
L4	2.836		0.466		0.344	
L5	3.557		0.45		0.32	
average	**3.3416**		**0.4628**		**0.3388**	
Point 2	Pv	7.228	Rms	0.571	Ra	0.433
L1	3.231		0.574		0.436	
L2	3.641		0.578		0.427	
L3	3.539		0.548		0.407	
L4	3.894		0.586		0.462	
L5	3.135		0.552		0.443	
average	**3.488**		**0.5676**		**0.435**	
Point 3	Pv	7.421	Rms	0.507	Ra	0.373
L1	4.382		0.553		0.439	
L2	3.18		0.554		0.417	
L3	2.88		0.473		0.346	
L4	2.585		0.412		0.314	
L5	2.819		0.506		0.372	
average	**3.1692**		**0.4996**		**0.3776**	
Point 4	Pv	5.278	Rms	0.496	Ra	0.346
L1	3.193		0.427		0.3	
L2	2.952		0.448		0.328	
L3	3.261		0.475		0.336	
L4	3.279		0.483		0.343	
L5	2.966		0.474		0.316	
average	**3.1302**		**0.4614**		**0.3246**	
Average	**3.28225**		**0.49785**		**0.369**	

Table B.8. Surface roughness measurement at feed of 10 μm/rev, Depth of cut of 100 μm and cutting speed of 200 m/min (all units in μm).

feed 10 μm/rev						
Point 1	Pv	5.18	Rms	0.453	Ra	0.33
L1	3.132		0.418		0.316	
L2	3.478		0.504		0.376	
L3	2.689		0.444		0.333	
L4	2.604		0.486		0.38	
L5	2.53		0.404		0.283	
average	**2.8866**		**0.4512**		**0.3376**	
Point 2	Pv	6.289	Rms	0.432	Ra	0.302
L1	2.869		0.384		0.272	
L2	2.448		0.411		0.29	
L3	3.173		0.443		0.311	
L4	3.048		0.453		0.339	
L5	2.926		0.374		0.256	
average	**2.8928**		**0.413**		**0.2936**	
Point 3	Pv	6.02	Rms	0.547	Ra	0.425
L1	3.401		0.58		0.45	
L2	0.972		0.501		0.394	
L3	3.476		0.559		0.432	
L4	2.676		0.465		0.364	
L5	4.073		0.599		0.459	
average	**2.9196**		**0.5408**		**0.4198**	
Point 4	Pv	6.507	Rms	0.439	Ra	0.309
L1	3.67		0.494		0.358	
L2	3.259		0.413		0.3	
L3	2.766		0.388		0.279	
L4	2.532		0.444		0.334	
L5	3.196		0.449		0.321	
average	**3.0846**		**0.4376**		**0.3184**	
Average	**2.9459**		**0.46065**		**0.34235**	

Table B.9. Surface roughness measurement at feed of 5 μm/rev, Depth of cut of 100 μm and cutting speed of 200 m/min (all units in μm).

feed 5 μm/rev						
Point 1	Pv	5.507	Rms	0.595	Ra	0.459
L1	3.712		0.595		0.468	
L2	2.869		0.56		0.457	
L3	3.959		0.647		0.502	
L4	3.318		0.512		0.391	
L5	3.383		0.56		0.433	
average	**3.4482**		**0.5748**		**0.4502**	
Point 2	Pv	6.125	Rms	0.593	Ra	0.455
L1	3.722		0.612		0.47	
L2	3.902		0.597		0.46	
L3	3.115		0.555		0.435	
L4	3.206		0.557		0.428	
L5	3.642		0.614		0.461	
average	**3.5174**		**0.587**		**0.4508**	
Point 3	Pv	5.623	Rms	0.539	Ra	0.415
L1	2.503		0.498		0.397	
L2	2.817		0.51		0.407	
L3	3.205		0.594		0.47	
L4	3.333		0.532		0.41	
L5	3.058		0.505		0.382	
average	**2.9832**		**0.5278**		**0.4132**	
Point 4	Pv	6.096	Rms	0.508	Ra	0.374
L1	3.863		0.556		0.386	
L2	3.011		0.444		0.332	
L3	3.723		0.43		0.298	
L4	2.895		0.488		0.361	
L5	3.121		0.561		0.419	
average	**3.3226**		**0.4958**		**0.3592**	
Average	**3.31785**		**0.54635**		**0.41835**	

REFERENCES

[1] C. R. Friedrich and S.D. Kang, 1994, "Micro heat exchangers fabricated by diamond machining", *Precision Eng.*, **16**, pp. 56-59.

[2] D. P. Adams, M. J. Vasile and A. S. M. Krishnan, "Microgrooving and microthreading tools for fabricating curvilinear features", *Precision Eng.*, **24**, pp. 347-356.

[3] D. P. Adams, M. J. Vasile, G. Benavides and A. N. Campbell, 2001, "Micromilling of metal alloys with focused ion beam-fabricated tools", *Precision Eng.*, **25**, pp. 107-113.

[4] K. Egashira, K. Mizutani and T. Nagao, 2002, "Ultrasonic vibration drilling of microholes in glass", *CIRP Ann.*, **51**, pp. 339-342.

[5] K. Egashira and K. Mizutani, 2002, "Micro-drilling of monocrystalline silicon using a cutting tool", *Precision Eng.,* **26**, pp. 263-268.

[6] T. Schaller, L. Bohn, J. Mayer and K. Schubert, 1999, "Microstructure grooves with a width of less than 50 μm cut with ground hard metal micro end mills", *Precision Eng.,* **23**, pp. 229-235.

[7] Y. Takeuchi, K. Sawada and T. Sata, 1996, "Ultraprecision 3d micromachining of glass", *CIRP Ann.*, **45**, pp. 401-404.

[8] C. R. Friedrich and M. J. Vasile, "Development of the micromilling process for high-aspect-ration microstructures", *J. Microelectromech. Syst.*, 5, pp. 33-38.

[9] S. Shoji and M. Esashi, 1994, "Microflow devices and systems", *J. Micromech. Microeng.*, **4**, pp. 157-171.

[10] H. Suzuki, N. Ohya, N. Kawahara, M. Yokoi, S. Ohyanagi, T. Kurahashi and T. Hattori, 1995, "Shell-body fabrication for micromachines", *J. Micromech. Microeng.*, **5**, pp. 36-40.

[11] H. Tritschler, J. Schmidt, D. Spath, J. Elsner and V. Huntrup, 2002, "Requirements of an industrially applicable microcutting process for steel microstructures", *Microsys. Technol*., **8**, pp. 402-408.

[12] W. R. Backer, E. R. Marshall, and M. C. Shaw, 1952, "The size effect in metal cutting", *Trans. of ASME,* pp. 74-61.

[13] E. M. Kopalinsky and P.L.B. Oxley, 1984, "Size effects in metal removal processes", *Institute of Physics Conference Series,* n70, 1984, pp. 389-396.

[14] K. Nakayama and K. Tamura, 1968, "Size effect in metal-cutting force", *American Society of Mechanical Engineers*, 67-Prod-9, 1967, 8p

[15] D. A. Lucca, R.L. Rhorer, and R. Komanduri, 1993, "Effect of tool edge geometry on energy dissipation in ultraprecision machining", *Annals of the CIRP*, **42**(1), pp. 83-86.

[16] Y. Furukawa and N. Moronuki, 1988, "Effect of material properties on ultra precision cutting process", *Annals of the CIRP*, 37(1), pp. 113-116.

[17] R. J. Schimmel and W. J. Endres, 2002, "Application of an internally consistent material model to determine the effect of tool edge geometry in orthogonal cutting", *Transactions of the ASME*, 124, pp. 536-543.

[18] R. K. Kountanya, 2002, "Process mechanics of metal cutting with edge radiused and worn tools", Ph.D. Dissertation, Univ. of Michigan.

[19] W.D. Nix, 1989, "Mechanical properties of thin films", *Metallurgical Transactions*, **20A**, pp. 2217-2245.

[20] Q. Ma and D.R. Clarke, 1995, "Size dependent hardness of silver single crystals", *J. Mater. Res.,* **10**, pp. 853-863.

[21] N.A. Stelmashenko, M.G. Walls, L.M. Brown, Y.V. Milman, 1993, "Microindentation on W and Mo oriented single crystals: an STM study", *Acta Metallurgica et Materialia*, **41**, pp. 2855-2865.

[22] N.A. Fleck, G.M. Muller, M. F. Ashby and J.W. Hutchinson, 1994, "Strain gradient plasticity: theory and experiments", *Acta Metallurgica et Materialia,* **42**(2), pp. 475-487.

[23] J.S. Stolken, A.G. Evans, 1998, "A microbend test method for measuring the plasticity length scale", *Metallurgica et Materialia*, **46**, No. 14, pp. 5109–5115.

[24] M. C. Shaw, 1984, "Metal cutting principles", Oxford University Press Inc., New York.

[25] J.Larsen-Basse and P.L.B. Oxley, 1973, "Effect of strain rate sensitivity on scale phenomena in chip formation", *Proceedings of the 13th International Machine Tool Design & Research Conference*, University of Birmingham, pp. 209-216

[26] T.D. Marusich, 2001, “Effects of friction and cutting speed on cutting force”, *Proc. IMECE (ASME), Nov. 11-16, New York.,* Paper#: MED-23313

[27] N. Fang, 2003, “Slip-line modeling of machining with a rounded-edge tool—part II: analysis of the size effect and shear strain-rate”, *J. Mech. Phys. Solids,* 51, 743-762.

[28] K.W. Kim, W.Y. Lee and H.C. Sin, 1999, “A finite element analysis of machining with the tool edge considered”, *J. of Mat. Proc. Tech.*, **86**, pp. 45-55.

[29] E.J.A. Armarego and R.H. Brown, 1962, “On the size effect in metal cutting”, *International Journal of Production Research.,* **1**, n3, pp. 75-99.

[30] M. Masuko, 1956, “Fundamental research on the metal cutting , second report”, *Bulletin of Japan Society of Mechanical Engineers*, Vol. **22**, No. 118, pp.371

[31] R. Komanduri, N. Chandrasekaran and L. M. Raff ,1998, “Effect of tool geometry in nanometric cutting: a molecular dynamics simulation approach”, *Wear,* **219**, pp. 84-97.

[32] A.G. Atkins, 2003, “Modeling metal cutting using modern ductile fracture mechanics: quantitative explanations for some longstanding problems”, *Int. J. of Mech. Sci.,* **45**, pp. 373-396.

[33] D. Dinesh, S. Swaminathan, S. Chandrasekar, and T.N. Farris, 2001, “An intrinsic size-effect in machining due to the strain gradient”, *Proc. 2001 ASME IMECE, Nov. 11-16, NY,* pp. 197-204.

[34] S. S. Joshi and S. N. Melkote, 2004, “An Explanation for the size-effect in machining based on strain gradient plasticity”, *Journal of Manufacturing Science and Engineering, Transactions of the ASME,* **126**, n 4, pp. 679-684.

[35] Merchant, M., E., 1944, "Basic Mechanics of the Cutting Process", *ASME Journal of Applied Mechanics*, Vol. **11**, pp.168-175.

[36] E. Usui and T. Shirakashi, 1982, “Mechanics of machining from descriptive to predictive theory, on the art of cutting metals-75 years later”, *ASME-PED*, **7**, pp.13-15.

[37] K. Iwata, A. Osakada and Y. Terasaka, 1984, “Process modeling of orthogonal cutting by rigid-plastic finite element method”, *Journal of Engineering Materials and Technology*, **106**, pp. 132-138.

[38] J.T. Carroll and J.S. Strenkowski, 1988, “Finite element models of orthogonal cutting with application to single point diamond turning”, *Int. J. of Mech. Sci.* Vol. **30**, pp. 899-920.

[39] K. Komvopoulous and S. A. Erpenbeck, 1991, "Finite element modeling of orthogonal metal cutting", *Trans. of ASME*, *J. Eng. Ind.*, Vol. **113**, pp. 253-267.

[40] T. Obikawa, H. Sasahara, T. Shirakashi and E. Usui, 1997, "Application of computational machining method to discontinuous chip formation", *J. Mfg. Sci. & Eng.,* Vol. **119**, pp. 667-674.

[41] T. Sata, M. Li, S. Takata, H. Hiraoka, C.Q. Li, X.Z. Xing and X.G. Xiao, 1985, "Analysis of surface roughness generation in turning operation and its applications", *STC PE*, **34/1**, pp. 473.

[42] A. J. Shih and H. T. Y. Yang, 1993, "Experimental and finite element predictions of residual stresses due to orthogonal metal cutting", *Int. J. Num. Methods in Engg.*, Vol. **36**, pp. 1487-1507.

[43] S. M. Athavale and J. S. Strenkowski, 1995, "Material based model for predicting chip breakability", *ASME Trans.: Manufacturing Science and Engineering*, MED-Vol 2-1/M-H Vol 3-1, pp. 303-316.

[44] S. M. Athavale and J. S. Strenkowski, 1998, "Finite element modeling of machining: from proof to concept to engineering applications", *CIRP Intl. Workshop on Modeling of Mach. Oprns.*, pp. 2B/3-1 – 2B/3-14

[45] T. MacGinley and J. Monaghan, 2001, "Modeling the orthogonal machining process using coated cemented carbide cutting tools", *Journal of Materials Processing Technology*, **118**, pp. 293-300.

[46] A. G. Mamalis, M. Horvath, A.S. Branis and D. E. Manolakos, "Finite element simulation of chip formation in orthogonal metal cutting", *Journal of Materials Processing Technology*, **110**, pp. 19-27.

[47] J. Q. Xie, A. E. Bayoumi and H. M. Zbib, 1994, "Characterization of chip formation and shear banding in orthogonal machining using finite element analysis", *American Society of Mechanical Engineers, Applied Mechanics Division, AMD*, v **183**, *Material Instabilities Theory and Application*, 1994, pp. 285-301.

[48] G. S. Sekon and J. L. Chenot, 1993, "Numerical simulation of continuous chip Formation during non steady orthogonal cutting", *Engineering Computations*, Vol. **10**, pp. 31-48.

[49] T. D. Marusich and M. Ortiz, 1995, "Modeling and simulation of high speed machining", *Int. J. Num. Methods in Engg.,* Vol. **21**, pp. 3675-3694.

[50] T. Ozel and T. Altan, 2000, "Determination of workpiece flow stress and friction at the chip-tool contact for high speed cutting", *International Journal of Machine Tools & Manufacture*, **40**, pp. 133-152

[51] E. Ceretti, 1998, "FEM simulations of segmented chip formation in orthogonal cutting: further improvements", *CIRP Intl. Workshop on Modeling of Mach. Oprns.*, pp. 2B/8-1 – 2B/8-7

[52] K. Liu and S.N. Melkote, 2004, "A strain gradient based finite element model for micro/meso-scale orthogonal cutting process", *Proceedings of 2004 Japan-USA Symposium on Flexible Automation*, Denver, Colorado, July, 2004.

[53] G. R. Johnson and W.H. Cook, 1983, "A constitutive model and data for metals subjected to large strain, high strain rates and high temperatures", *Proc. 7th Int. Symp. on Ballistics*, pp. 541-547.

[54] K.W. Kim, W. Y. Lee and H. Sin, 1999, "A finite element analysis for the characteristics of temperature and stress in micro-machining considering the size effect", *International Journal of Machine Tools & Manufacture*, **39**, pp. 1507-1524.

[55] Y. B. Guo, 2004, "A FEM study on mechanisms of discontinuous chip formation in hard turning", *Journal of Materials Processing Technology*, v **155-156**, pp. 1350-1356.

[56] S. Jing and C.R. Liu, "The influence of material models on finite element simulation of machining", *Transactions of the ASME. Journal of Manufacturing Science and Engineering*, v **126**, n 4, pp. 849-857.

[57] A. Ramesh, 2002, "Prediction of process-induced microstructural changes and residual stresses in orthogonal hard machining", Ph.D. Thesis, Mechanical Engineering, Georgia Institute of Technology.

[58] N.A. Fleck and J.W. Hutchinson, 1993, "A phenomenological theory for strain gradient effects in plasticity", *J. Mech. Phys. Solids,* **41**, pp. 1825–1857.

[59] H. Gao, Y. Huang, W.D. Nix, and J.W. Hutchinson, 1999, "Mechanism-based strain gradient plasticity - I. Theory", *J. Mech. Phys. Solids,* **47**. pp. 1239-1263.

[60] A. Acharya and J.L. Bassani, 2000, "Lattice incompatibility and a gradient theory of crystal plasticity", *J. Mech. Phys. Solids,* **48**, pp. 1565-1595.

[61] M. Zhou and B.K. A Ngoi, 2001,"Effect of tool and workpiece anisotropy on microcutting processes", *Proc. Instn. Mech. Engrs*. Vol 215 part B 13-19.

[62] Y. Liang, N. Moronuki and Y. Furukawa, 1994,"Calculations of the effect of material anisotropy on microcutting processes", *Precision Engineering*, vol 16, No 2. 132-138.

[63] L. Chuzhoy, R. E. DeVor, S. G. Kapoor and D. J. Bammann, 2001, "Microstructure-level modeling of ductile iron machining", *Proc. ASME*

Manufacturing Engineering Division (MED-Vol. **12**), 2001 ASME International Mechanical Engineering Congress and Exposition , NY, pp. 125-134.

[64] Y.C. Yen, A. Jain and T. Altan, "A finite element analysis of orthogonal machining using different tool edge geometries", *Journal of Materials Processing Technology*, v **146**, n 1, pp. 72-81.

[65] J. C. Jaeger, 1942, "Moving sources of heat and temperature at sliding contact", *Proc. Royal Soceity of New South Wales*, 76, pp203-224.

[66] H. Chandrashekharan and A. Thuvander, 1998, "Tool stresses and temperature in machining", *CIRP Intl. Workshop on Modeling of Mach. Oprns.*, pp. 2B/7-1 – 2B/7-10.

[67] Ng, E-G., D. K. Aspinwall, D. Brazil and J. Monaghan, 1999, "Modeling of temperature and forces when orthogonally machining hardened steel", *Intl. J. Machine Tools and Manufacture*, Vol. 39, pp. 885-903.

[68] I. W. Park, 1996, "Modeling of burr formation processes in metal cutting", *Ph. D. Dissertation,* Dept. of Mechanical Engineering, University of California at Berkeley.

[69] M. Hashimura, Y. P. Chang and D. Dornfeld, 1999, "Analysis of burr formation in orthogonal cutting", *Journal of Manufacturing Science and Engineering*, vol. 121, pp. 1-7.

[70] Y. B. Guo and D. A. Dornfeld, 2000, "Finite element modeling of burr formation process in drilling 304 Stainless Steel", *J. Mfg. Science and Engg*., Vol. 122, pp 612 – 619.

[71] A. C. Erigen, 1987, "Theory of nonlocal elasticity and some applications", *Res Mechanica: International Journal of Structural Mechanics and Materials Science*, v **21**, n 4, pp. 313-342.

[72] R. A. Toupin, 1962, "Elastic materials with couple stresses", *Arch. Ration. Mech. Anal.* **11**, 385-414.

[73] A. Needleman, 1988, "Material rate dependence and mesh sensitivity in localization problems", *Computer Methods in Applied Mechanics and Engineering*, v **67**, n 1, pp. 69-85.

[74] D. L. McDowell, 2000, "Modeling and experiments in plasticity", *International Journal of Solids and Structures,* **37**, pp. 293-309.

[75] W. T. Koiter, 1964, "Couple stresses in the theory of elasticity, I and II", *Proc. K. Ned. Akad. Wet.*, (B), **67**, pp. 17-44

[76] R. D. Mindlin, 1964, "Micro-structure in linear elasticity", *Arch. Ration. Mech. Anal.* **16**, 51-78.

[77] R. D. Mindlin, 1965, "Secondary gradient of strain and surface tension in linear elasticity", *Int. J. Solids Struct*., **1**, 417-438.

[78] N. A. Fleck and J. W. Hutchinson, 2001, "A reformulation of strain gradient plasticity", *Journal of the Mechanics and Physics of Solids*, v **49**, n 10, pp. 2245-2271.

[79] E. C. Aifantis, 1984, "On the microstructural origin of certain inelastic models", *ASME Journal of Engineering Materials and Technology*, Vol. **106**, pp. 326-330.

[80] E. C. Aifantis, 1987, "The physics of plastic deformation", *Int. J. Plasticity*, Vol. **3**, pp. 211-247.

[81] H. Zbib and E. C. Aifantis, 1989, "On the localization and postlocalization behavior of plastic deformation. Part I. On the initiation of shear bands; Part II: On the evolution and thickness of shear bands; Part III: On the structure and velocity of Portevin-Le Chatelier bands", *Res. Mech.* pp. 261-277, 279-292 and 293-305.

[82] W. D. Nix and H. Gao, 1998, "Indentation size effects in crystalline materials: a low for strain gradient plasticity", *J. Mech. Phys. Solids*, **46**, 411-425.

[83] K. W. McElhaney, J. J. Vlassak and W. D. Nix, 1998, "Determination of indenter tip geometry and indentation contact area for depth-sensing indentation experiments", *J. Mater. Res.*, **13**, pp. 1300.

[84] H. Gao and Y. Huang, 2001, "Taylor-based nonlocal theory of plasticity", *International Journal of Solids and Structures,* **38**, pp. 2615-2637.

[85] T. Ozel, 2005, "Predictive modeling of surface roughness and tool wear in hard turning using regression and neural networks", *International Journal of Machine Tools and Manufacture*, v**45**, n4-5, pp. 467-479.

[86] Y. Sahin and A. R. Motorcu, 2005, "Surface roughness model for machining mild steel with carbide tool", *Materials and Design*, v**26**, n4, pp.321-326.

[87] A. Kohli and U. S. Dixit, 2005, "A neural-network based methodology for the prediction of surface roughness in a turning process", *International Journal of Advanced Manufacturing Technology*, v**25**, n1-2, pp. 118-129.

[88] Y. Jiao, S. T. Lei and Z. J. Pei, 2004, "Fuzzy adaptive networks in machining process modeling: Surface roughness prediction for turning operations", *International Journal of Machine Tools and Manufacture*, v**44**, n15, pp. 1643-1651.

[89] C. X. Feng and X. Wang, 2002, "Development of empirical models for surface roughness prediction in finish turning", *International Journal of Advanced Manufacturing Technology*, v**20**, n5, pp. 348-356.

[90] Y. Z. Dai and F. P. Chiang, 1992, "On the mechanism of plastic deformation induced surface roughness", *Transactions of the ASME,* vol.114, 432-438.

[91] P. F. Thomson and P. U. Nayak, 1979, "The effect of plastic deformation on the roughening of free surfaces of sheet metal", *Int. J. Mach. Tool Des.Res.* vol. 20 pp73-86.

[92] P. F. Thomson and B. V. Shafer, 1982, "The roughening of free surfaces during plastic working", *Int. J. Mach. Tool Des.Res.* vol. 22 pp261-264.

[93] S. To, C. F. Cheung and W. B. Lee, 2001, "Influence of material swelling on surface roughness in diamond turning of single crystals", *Materials Science and Technology*, vol. 17, 102-108.

[94] S. Takasu, M. Masuda, T. Nishiguchi and A. Kobayashi, 1985, "Influence of study vibration with small amplitude upon surface roughness in diamond machining", *Annals of the CIRP,* 34/1, pp 463-467.

[95] O. B. Abouelatta and J. Madl, 2001, "Surface roughness prediction based on cutting parameters and tool vibrations in turning operations", Journal of Materials Processing Technology, v**118**, n1-3, pp.269-277.

[96] C. F. Cheung and W. B. Lee, 2000, "Theoretical and experimental investigation of surface roughness formation in ultra-precision diamond turning", International Journal of Machine Tools and Manufacture, v**40**, n7, pp.979-1002.

[97] Z. J. Yuan, W. B. Lee, Y. X. Yao and M. Zhou, 1994, "Effect of crystallographic orientation on cutting forces and surface quality in diamond cutting of single crystal", *Annals of the CIRP*, 43/1, pp. 39.

[98] P. H. Brammertz, 1961, "Ursachen fur formund massfehler an feinbearbeiten werkstuchken", Dissertation, T.H., Aachen.

[99] W. Grzesik, 1996, "A revised model for predicting surface roughness in turning", *Wear*, **194**, pp. 143-148.

[100] E. Amanatidou and N. Aravas, 2002, "Mixed finite element formulation of strain gradient elasticity problems", *Computer Methods in Applied Mechanics and Engineering*, v **191**, n 15-16, pp. 1723-1751.

[101] J. Y. Shu, W. E. King and N. A. Fleck, 1999, "Finite elements for materials with strain gradient effects", *International Journal for Numerical Methods in Engineering*, v **44**, n 3, pp. 373-91.

[102] N. N. Zorev, 1963, "Inter-relationship between shear processes occurring along tool face and shear plane in metal cutting", *International Research in Production Engineering*, pp. 42-49.

[103] T. Shirakashi, and E. Usui, 1974, "Simulation Analysis of Orthogonal Metal Cutting Mechanism", *Proceedings of the International Conference of Production Engineering*, Tokyo, Part I, pp. 535-540.

[104] J. T. Burwell and C. D. Strang, 1952, *Journal of Applied Physics*, vol. **23**, pp.18.

[105] A. A. Radwan, 1985, "Investigation of secondary deformation zone and mean coefficient of friction during the machining of 5083-H34 aluminum alloy", *Wear*, **101**, pp. 191-204.

[106] G. S. Sekon and J. L. Chenot, 1993, "Numerical Simulation of Continuous Chip Formation during Non Steady Orthogonal Cutting", *Engineering Computations*, Vol. **10**, pp. 31-48.

[107] Y. B. Guo, "3-D Modeling of Superfinish Hard Turning", *Ph.D. Dissertation,* Dept. of Industrial Engineering, Purdue University.

[108] V. Hamel, J.M. Roelandt, J. N. Gacel and F. Schmit, 2000, "Finite element modeling of clinch forming with automatic remeshing", *Computers and Structures*, **77**, pp. 185-200.

[109] N. Fang, 2003, "Sensitivity analysis of the material flow stress in machining", *American Society of Mechanical Engineers, Manufacturing Engineering Division, MED*, **14**, 2003, p 23-32.

[110] S. Kalpakjian, 1984, "Manufacturing processes for engineering materials", third edition, Addison Wesley.

[111] A. H. Clausen, T. Borvik, O.S. Hopperstad and A. Benallal, 2004, "Flow and fracture characteristic of aluminum alloy AA5083-H116 as function of strain rate, temperature and triaxiality", *Materials Science and Engineering*, **A364**, pp. 260-272.

[112] T. Altan and F.W. Bougler, 1973, "Flow stress of metals and its application in metal forming analyses", *American Society of Mechanical Engineers*, n **73**-Prod-4, 1973, 11p.

[113] MatWeb material database http://www.matweb.com.

[114] N. Ikawa, S. Shimada and H. Tanaka, 1992, “Minimum Thickness of Cut in Micromachining”, Nanotechnology, Vol. **3**, 6-9.

[115] C. K. Ng, 2005, “Experimental study of micro-/nano-scale cutting of aluminum 7075 and P20 mold steel”, Master Thesis, Dept. of Mechanical Engineering, Georgia Institute of Technology.

[116] P.L.B. Oxley, 1989, “Mechanics of machining, An analytical approach to assessing machinability”, Ellis Horwood Ltd, Chichester.

[117] M. Zhou and M.P. Clode, 1998, “Constitutive equations for modeling flow softening due to dynamic recovery and heat generation during plastic deformation”, *Mechanics of Materials*, **27**, pp. 63-76.

[118] D. J. Waldorf, R. E. DeVor and S.G. Kapoor, 1999, “An evaluation of ploughing models for orthogonal machining”, Transactions of the ASME, Journal of Manufacturing Science and Engineering, Vol. 121, pp. 550-557.

[119] A. P. Sokolowski, 1955, “Prazision in der Metallbearbeitung”, VEB Verlag Technik, Berlin.

[120] T. Sata and M. C. Shaw, 1964, “Behavior of cellular materials undergoing plastic flow”, *CIRP Ann.*, 12, 190.

[121] V. Jardret, H. Zahouani, J. L. Loubet and T. G. Mathia, 1998, “Understanding and quantification of elastic and plastic deformation during a scratch test”, *Wear*, **218**, pp. 8-14.

[122] J. L. Bucaille, E. Felder and G. Hochstetter, 2001, “Mechanical analysis of the scratch test on elastic and perfectly plastic materials with the three-dimensional finite element modeling”, *Wear*, **249,** pp. 422-432.

[123] B. Taljat, G. M. Pharr, 2004, “Development of plie-up during spherical indentation of elastic-plastic solids”, *International Journal of Solids and Structures*, **41**, pp. 3891-3904.

[124] R. J. Schimmel, J. Manjunathaiah and W. J. Endres, 2000, “Edge radius variability and force measurement considerations”, *Transactions of the ASME, J. of Manufacturing Science and Enginering*, Vol. **122**, pp. 590-593.

[125] R. J. Schimmel, 1999, “Analyzing and modeling the effects of tool edge geometry in machining”, Ph.D Dissertation, Univ. of Michigan.

[126] E. Usui and T. Shirakashi, 1982, “Mechanics of machining – from descriptive to predictive theory. In on the art of cutting metals-75 years later”, *ASME Publication PED **7***, pp. 13-35.

[127] A. J. Shih, S. Chandrasekar and H.T. Yang, 1990, "Finite element simulation of metal cutting process with strain-rate and temperatures effects", *Fundamental Issues in Machining*, *ASME, PED* **43**, pp. 11-24.

[128] S. Bhattacharya and M.R. Lovell, 2000, "Characterization of friction in machining: evaluation of asperity deformation and seizure-based models", *Transactions of NAMRI/SME, XXVII*, pp. 107-112.

[129] M.R. Lovell, S. Bhattacharya and R. Zeng, 1998, "Modeling orthogonal machining for variable tool-chip interfacial friction using explicit dynamic finite element methods", *Proceedings of the CIRP international workshop on modeling of machining operations*, pp. 265-276.

[130] Z. Tao and M.R. Lovell, 2002, "Towards an improved friction model in material removal processes: Investigating the role of temperature", *Technical paper – SME, MR02-188*, pp.1-8.

[131] V. Madhavan, S. Chandrasekar and T.N. Farris, 2000, "Machining as a wedge indentation", *Journal of Applied Mechanics, Transactions of the ASME,* **67**, pp. 128-139.

[132] E. Ceretti, P. Fallbohmer, W.T. Wu and T. Altan, 1996, "Application of 2D FEM to chip formation in orthogonal cutting", *Journal of Materials Processing Technology*, **59**, pp. 169-180.

[133] P.L.B. Oxley, 1989, "Mechanics of machining, An analytical approach to assessing machinability", Ellis Horwood Ltd, Chichester.

[134] G. Shi, X. Deng and C. Shet, 2002, "A finite element study of the effect of friction in orthogonal metal cutting", *Finite Element in Analysis and Design*, 38, pp.863-883.

VITA

KAI LIU

LIU was born in Huangshi, Hubei, China. He attended public schools in Guixi, JiangXi, received a B.S. in Mechanical Engineering from Tsinghua University, Beijing, China in 1999 and a M.S. in Mechanical Engineering from Polytechnic University, Brooklyn, New York in 2001 before coming to Georgia Tech to pursue a doctorate in Mechanical Engineering.